University of California
Los Angeles

Plasma Sputtering Behavior of Structured Materials

A dissertation submitted in partial satisfaction
of the requirements for the degree
Doctor of Philosophy in Aerospace Engineering

by

Gary Zhi Li

2020

ABSTRACT OF THE DISSERTATION

Plasma Sputtering Behavior of Structured Materials

by

Gary Zhi Li
Doctor of Philosophy in Aerospace Engineering
University of California, Los Angeles, 2020
Professor Richard E. Wirz, Chair

The energetic ion bombardment, or sputtering, of plasma devices is a universal phenomenon and challenge. In applications that require long lifetimes and high performance, such as electric propulsion or nuclear fusion, the plasma facing components must be designed to minimize sputtering. Next generation devices will require advanced materials that can reduce sputtering beyond what is currently possible with standard solid materials. To address this need, the objective of this dissertation is to investigate the plasma sputtering behavior of structured materials for long-term resilience and reduced contamination.

The Plasma interactions facility at UCLA is configured to perform sputtering measurements of materials with evolving surface morphologies. A focused argon plasma is directed to an electrically biased target for energetic ion bombardment, and a scanning quartz crystal microbalance is used to obtain time-resolved sputtering measurements. The first experiment in this dissertation exposes a novel micro-architectured molybdenum sample to 300 eV argon ions for 17 h. The total sputtering yield is initially significantly reduced compared to that of a flat sample, but is shown to approach the flat yield after 10 h as the surface features are eroded away. The discovery that featured surfaces can only provide a sputtering reduction for a limited time motivates the investigation of open-cell foams as a volumetrically structured material.

Two aluminum foams with 40 Pores Per Inch (PPI) and 10 PPI pore density are tested in the Pi facility and sputtering yield measurements are obtained. For the first time, the aluminum foams demonstrate a sustained reduction in sputtering yield, ranging from 40% to 60% compared to a flat surface over a 30 h exposure to 300 eV argon ions. Furthermore, the reduction in yield is found to be as large as 80% at lower ion energies. The measured yields prove that foams can maintain a reduced sputtering yield and that the plasma environment plays a major role in determining the foam sputtering behavior. A plasma-foam sputtering theory and analytical model are introduced to understand the experimental findings and study the key physical processes.

A metallic open-cell foam uniquely interacts with plasma depending on the ratio of the foam pore size to the plasma sheath thickness. A plasma-infused foam is defined as having pore sizes much larger than the sheath thickness, which will allow plasma to infuse the foam interior. In the opposite limit, a plasma-facing foam will have an external sheath that accelerates ions normal to the macroscopic surface. The angular sputtering profiles at low ion energies and reduced ion fluxes from plasma density gradients are shown to play a major role in reducing the sputtering yield. Additionally, the effective sputtering area is significantly increased for a plasma-infused foam, resulting in a larger yield relative to a foam with less plasma infusion. The key processes involved in reducing, or in some cases enhancing, the effective sputtering yield are found to be the plasma-foam sputtering behavior and the geometric recapture of sputtered particles.

The dynamic interplay between plasma and material processes is shown to govern plasma-foam sputtering behavior. In addition to excellent sputtering resistance, metallic foams offer attractive thermomechanical properties and the potential for interlayer transport of fluids for various plasma applications. The potential impact of plasma-foam sputtering for both theoretical investigation and practical application is discussed and multiple avenues of future work are recommended.

The dissertation of Gary Zhi Li is approved.

Taylor S. Matlock

George J. Morales

Xiaolin Zhong

Nasr M. Ghoniem

Richard E. Wirz, Committee Chair

University of California, Los Angeles
2020

Dedicated to friends and family.

Table of Contents

List of Figures

LIST OF TABLES

ACKNOWLEDGMENTS

First and foremost, I would like to thank my advisor Prof. Richard Wirz. From the moment you accepted me into your lab as a clueless physics student, you've taught me the ins and outs of experiments, the nuances of computational modeling, and molded me into the engineer I am today. No day in grad school was the same. One day, we'd discover groundbreaking results. The next day, the hollow cathode would break again. Through all the ups and downs, you were always there to encourage me. When I was lost on what to do, you guided me to the right path and showed me that sometimes you just need to look at things from a different perspective. I will never forget time and creative space. Thank you for believing in me and supporting me through all these years.

I am grateful to Prof. Xiaolin Zhong, Prof. Nasr Ghoniem, Prof. George Morales, and Dr. Taylor Matlock for taking the time to serve on my thesis committee. Your advice as experts in the field was invaluable. I also want to thank my mentors from my internships: Dr. Ira Katz from NASA JPL for guiding me on electrospray modeling, Dr. Carrie Hill from Edwards AFRL for teaching me about field reversed configuration thrusters, and Dr. Bill Tighe from The Aerospace Corporation for always having a story about hollow cathodes. I also want to thank Steve Isakowitz and the Matthew Isakowitz Fellowship for showing me how exciting the New Space industry is and for reviving my passion for commercial spaceflight. Finally, I want to acknowledge my funding sources, the National Defense Science and Engineering Graduate Fellowship and the Mechanical & Aerospace Engineering Department.

Grad school wouldn't have been possible without my amazing labmates: Jun, Ben, Marlene, Cesar, Chris, Louis, Phil, Stephen, Ani, Nolan, Peter, Henry, Kenna, Angelica, Mary, Adam, Zhitong, Kaiyuan, Yide, Parker, Mitchell, and Sid. Our lab shenanigans are what kept me sane through these long stressful years. I'm still disappointed we never got to film a day in the life of the Chunky Lab. I'm going to miss our long days running experiments together, hiking adventures, seasonal parties, quarterly dining hall splurges, and daily lunch

conversations. As the old members graduated and fresh faces joined the lab, I was surprised to see that the lab culture was always preserved. The future of the lab is in great hands and I'm excited to see what great things everyone will accomplish.

Finally, I want to thank my friends and family. Jason Chang, my roommate of 5 years, was always there to lend an ear. I'll forever remember our random conversations and epic adventures. None of this would have been possible without my parents. I still don't know how you guys moved to America with nothing, and raised Alan and me while working tirelessly everyday. Dad will always be my role model; the first in my family to get a PhD and the one who led by example. Mom supported me the entire way, no matter how many mistakes I made. To Mom and Dad, thank you for giving me the opportunity to follow my dreams.

Vita

2011-2014	Teaching Assistant, *General Astronomy*, Astronomy Department, University of California, Berkeley
2014	B.A. (Astrophysics) and B.A. (Physics), University of California, Berkeley.
2014–2020	Graduate Student Researcher, Plasma & Space Propulsion Laboratory, University of California, Los Angeles.
2014	Mechanical & Aerospace Engineering Graduate Fellowship, University of California, Los Angeles.
2015	National Defense Science and Engineering Graduate Fellowship
2016	M.S. (Aerospace Engineering), University of California, Los Angeles.
2019	Boeing Graduate Fellowship
2019	Matthew Isakowitz Fellowship
2018–2020	Teaching Assistant, *Plasma & Ionized Gases, Astronautics, Spacecraft Technology, Spacecraft Design*, Mechanical & Aerospace Engineering Department, University of California, Los Angeles.

PUBLICATIONS

Li G and Wirz R, "Persistent Sputtering Yield Reduction in Plasma-Infused Foams", *Physical Review Letters*, submitted, 2020.

Li G, Matlock T, Goebel D, Dodson C, Matthes C, Ghoniem N, and Wirz R, "In situ plasma sputtering and angular distribution measurements for structured molybdenum surfaces", *Plasma Sources Science and Technology*, **26** (6), 2017.

Matthes C, Ghoniem N, Li G, Matlock T, Goebel D, Dodson C, and Wirz R, "Fluence-dependent Sputtering Yield of Micro-architectured Materials", *Applied Surface Science* **407**, 223-235, 2017.

Ottaviano A, Li G, Huerta C, Thuppul A, Chen Z, Dodson C, and Wirz R, "Plasma-Material Interactions for Electric Propulsion: Challenges, Approaches, Future", *36th International Electric Propulsion Conference*, 2019.

Li G, Huerta C, and Wirz R, "Computational Modeling of an Axial Ring Cusp Discharge for the MiXI Thruster", *54th Joint Propulsion Conference*, 2018.

Samples S, Li G, and Wirz R, "Performance Testing and Development of the MiXI Thruster with the ARCH Discharge", *54th Joint Propulsion Conference*, 2018.

Li G, Dodson C, Wirz R, Matlock T, and Goebel D, "Implementation of in situ diagnostics for sputter yield measurements in a focused plasma", *52nd Joint Propulsion Conference*, 2016.

CHAPTER 1

Introduction

Sputtering is the process by which particles are ejected when a material is impacted by an energetic ion. As a fundamental plasma-material interaction, sputtering is an omnipresent phenomenon in both nature and artificial plasma devices. In nature, high energy ions are present in the solar wind, the interiors of stars, the radiation belts, and generally anywhere there exists an acceleration process and a vacuum for the ion to maintain its energy. On Earth, the atmosphere is dense enough such that ions lose their energy to collisions unless the ion is accelerated in an enclosed vacuum vessel. Therefore, sputtering can occur for plasma devices such as electric propulsion thrusters, nuclear fusion reactors, plasma processing machines, and particle accelerators. In plasma processing machines, sputtering may have a positive effect for applications such as sputter deposition of thin films. However, for other applications such as electric propulsion and nuclear fusion, ions can cause systemic erosion to the plasma-facing walls and result in limited performance and lifetime. My dissertation will focus on the latter application and investigate methods of reducing the effective sputtering yield of plasma-facing materials.

1.1 Applications Influenced by Plasma Sputtering

1.1.1 Electric Propulsion

Electric propulsion (EP) thrusters are used as fuel efficient alternatives to traditional chemical rockets for in-space applications. EP devices have enabled deep space exploration missions such as Dawn and SMART-1 and have allowed for significant fuel savings for commercial applications such as telecommunications and satellite imagery. The guiding principle behind EP thrusters is the acceleration of charged particles via electromagnetic fields. As an example, the acceleration of a singly charged ion of mass m and charge q through an electrostatic grid of potential difference ϕ will yield an ion velocity of $\sqrt{2q\phi/m}$. Compared to chemical thrusters that are limited to low exhaust velocities due to temperature limits, electric thrusters can theoretically accelerate particles to near light speed given enough electrical power. The rocket equation describes the effect of high exhaust velocities on a spacecraft's propellant mass:

$$m_{\text{prop}} = m_{\text{PL}} \left[\exp\left(\frac{\Delta V}{u_{\text{ex}}} \right) - 1 \right] \tag{1.1}$$

where m_{prop} and m_{PL} are the propellant and payload masses respectively, ΔV is the change in velocity required for a given thruster maneuver, and u_{ex} is the thruster exhaust velocity. A large exhaust velocity results in a smaller propellant mass which allow mission designers to add useful payloads or save costs.

EP thrusters can extract ions from plasmas or ionic liquids. This dissertation focuses on the sputtering behavior of plasma-exposed materials that are present in devices such as ion thrusters, Hall thrusters, and magnetoplasmadynamic (MPD) thrusters. An overview of the sputtering mechanisms in these thrusters are discussed in the following sections.

1.1.1.1 Ion Thrusters

Gridded ion thrusters are high specific impulse, low thrust propulsion devices that have been used for a variety of missions. Early development started in the 1960s, and they have been gaining traction in space agency missions and the satellite industry in the recent decades. The NASA Dawn mission[1] utilized the NSTAR 30 cm ion thrusters to travel and orbit around two different asteroids. A similar ion thruster called the Xenon Ion Propulsion System (XIPS)

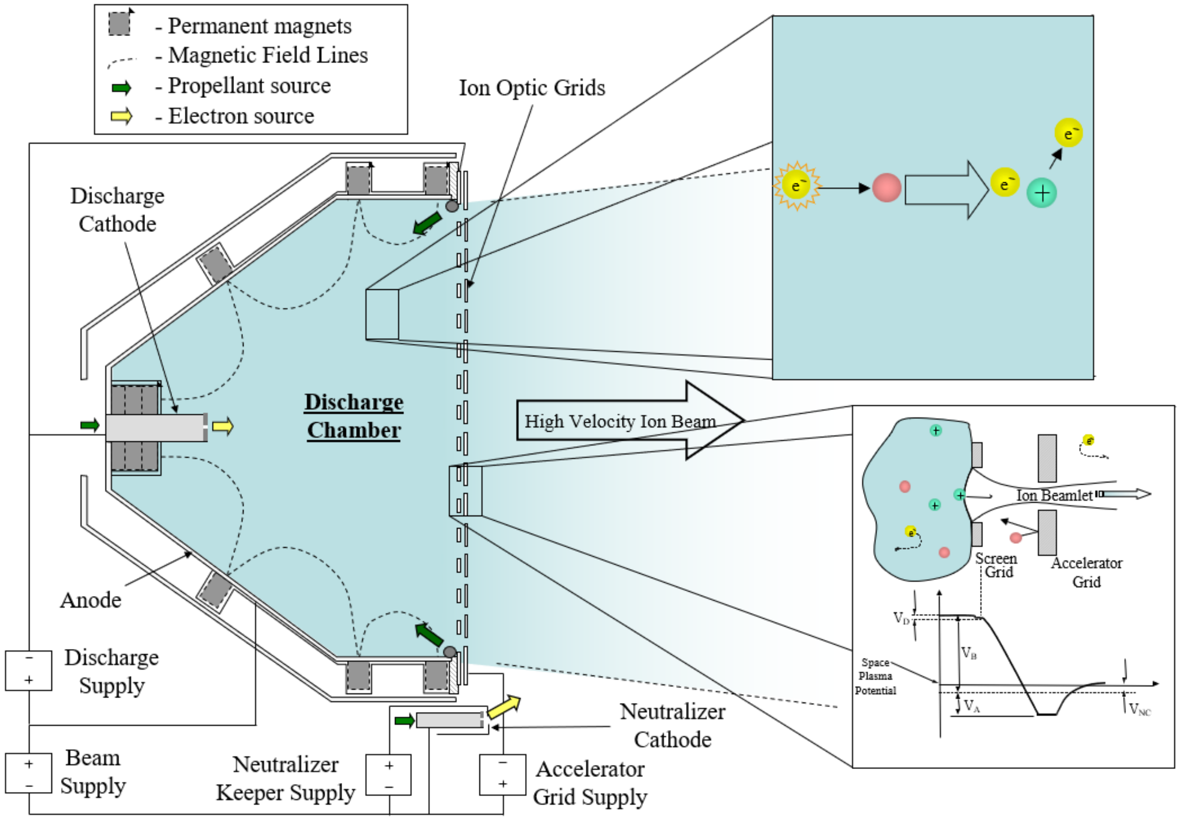

Figure 1.1: Electrical diagram of a gridded ion thruster. Source: R. Wirz (2005).

thruster was developed by L3 communications and is now flown on several satellites[2]. Furthermore, gridded ion thrusters are being used for future designs including that of a 50,000 s lithium-fueled ion thruster[3] and miniature xenon ion (MiXI) thrusters[4, 5]. While extensive research has been performed on these thrusters to ensure long lifetime and high performance, there are some issues that remain unresolved.

Ion thrusters operate with modular stages consisting of plasma generation, ion acceleration, and beam neutralization. Figure 1.1 shows a schematic of a gridded ion thruster with the main processes highlighted. A gaseous propellant, typically xenon, is injected into the enclosed discharge chamber. Electrons emitted from the hollow cathode, labeled “discharge cathode”, are accelerated by potential fields generated by the direct current (dc) discharge and subsequently impact neutral propellant atoms, creating a partially ionized plasma[6].

Following the plasma generation stage, ions are extracted through the ion optics to form an ion beam. As shown in the subimage in Figure 1.1, the screen and accelerator grids form a negative-going potential structure to accelerate ions with a negative potential trough to repel backstreaming electrons. Finally, electrons are emitted from the neutralizer cathode outside the thruster to neutralize the beam and avoid charge accumulation on the spacecraft.

One of the largest remaining issues is that of accelerator grid erosion[7, 8, 9]. The accelerator grid is the second grid in the ion optics system and is biased negatively relative to space potential, which is often ground potential in laboratory systems. Ions do not pick up the full energy from the voltage difference between the screen and accelerator grids due to the potential hill from the accelerator grid to the ambient background. However, the relative negative potential of the accelerator grid allows backstreaming electrons from outside the thruster to be deflected, preventing shorting issues inside the discharge chamber. The problem is associated with the neutral propellant atoms that stream through the ion optics system. Accelerated ions can interact with the slow neutral atoms via the resonant charge-exchange (CEX) process to produce a fast neutron and slow ion. The fast neutron will follow the same trajectory and escape the thruster while the slow ion may be born at a downward sloping potential location and accelerate towards the accelerator grid until impacting and sputtering. There are two characteristic erosion patterns from these CEX

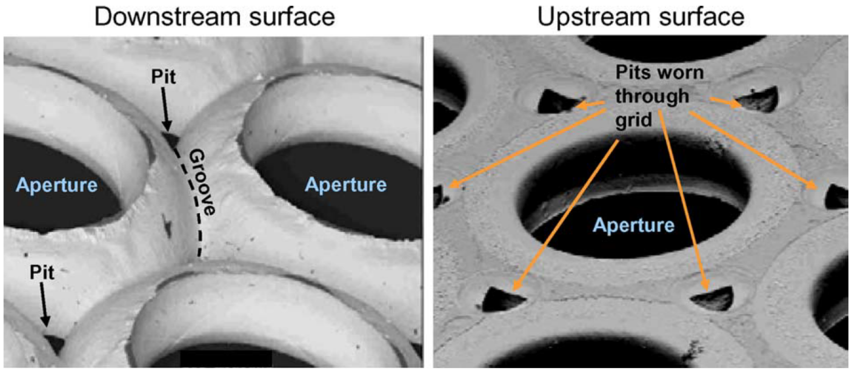

Figure 1.2: SEM images of pits and grooves erosion of the NSTAR ion optics system. Source: R. Wirz (2011).

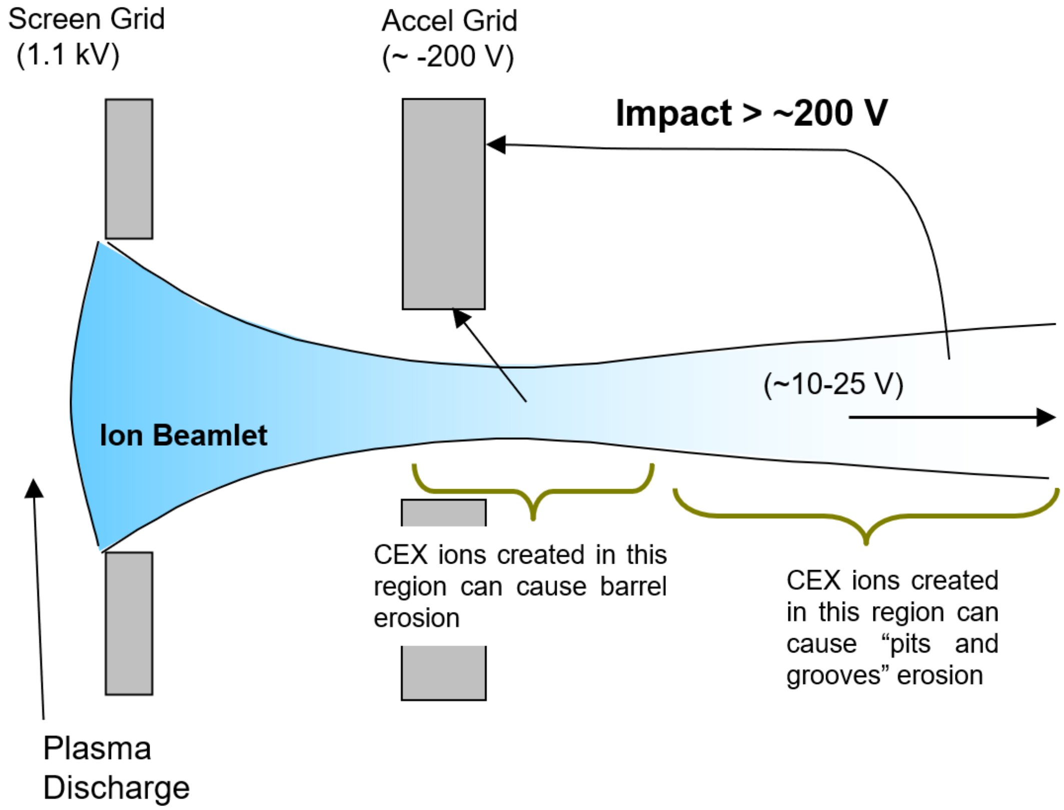

Figure 1.3: Illustration of accelerator grid erosion with and without a decelerator grid. Modified from R. Wirz (2011).

ions as shown in Figure 1.2: (1) pits and grooves erosion and (2) barrel erosion. Pits and grooves erosion results from ions born from downstream of the accelerator grid and therefore impact the grid from the outside and in between the orifices. Barrel erosion is due to ions born inside the orifice or between the grids and results in widening of the grid holes.

Figure 1.3 shows the detailed processes for CEX erosion as well as screen grid erosion from ions inside discharge chamber. It is seen that CEX ions born in the plume can impact the accelerator grid with energies from 200 - 300 eV, for both barrel and pits and grooves erosion. Meanwhile, ions in the discharge plasma are accelerated towards the screen grid through the plasma sheath, acquiring energies on order of the discharge voltage. Therefore, ion optics erosion is primarily a particle-based erosion effect while the screen grid erosion depends heavily on the plasma-material interactions at the grid.

1.1.1.2 Hall Thrusters

Similar to ion thrusters, Hall effect thrusters (HET) are electrostatic thrusters that accelerate ionized propellant using an electric field. The 13 kW Hall Effect Rocket with Magnetic Shielding (HERMeS) is shown in Figure 1.4a with externally mounted hollow cathodes and operating on xenon plasma. The electrons generated by the hollow cathodes are confined in the annular channels via applied magnetic fields and result in an $E \times B$ current. The azimuthal electron current ionizes the propellant injected into the channel and a downstream electric field accelerates ions to high velocities. High power variants of single-channel HET are nested-channel HET that can have two or more concentric annular channels as shown in Figure 1.4b. The extra channels allow for a larger discharge current to be generated for higher thrust operation.

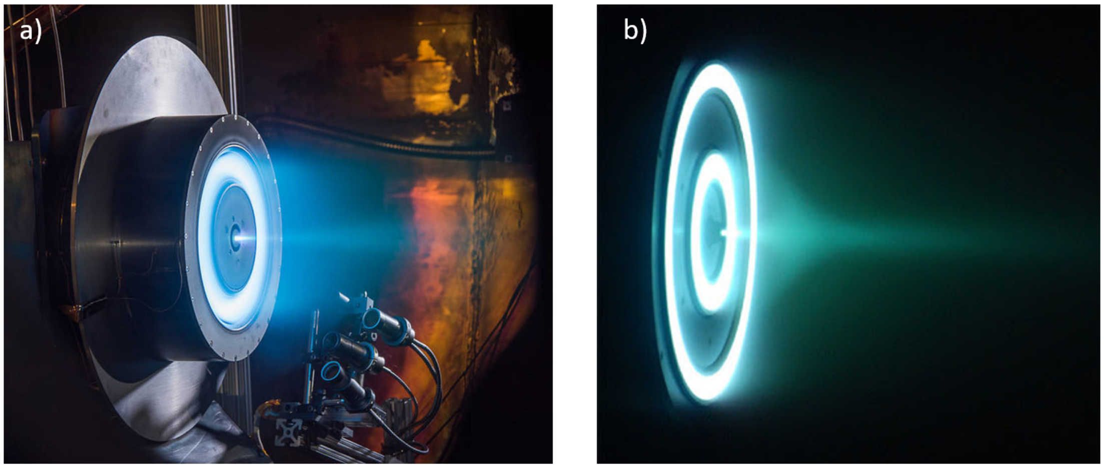

Figure 1.4: The thrusters shown are a) the 13 kW Hall Effect Rocket with Magnetic Shielding (HERMeS) (Source: NASA Glenn) and b) the nested channel Hall thruster (Source: UofM PEPL).

Traditional HET experience erosion through sputtering of the ceramic walls of in the annular channels[10]. A common observation is the erosion ridges shown in Figure 1.5 which form after 100 h of operation. The primary HET failure mode results from the excessive erosion of the channels which expose the underlying magnetic circuitry. The magnetically shielded variants of the HET as shown in Figure 1.4 has a similar annular plasma structure, but has a different magnetic field geometry that reduces the ion energy hitting the annular channels. Magnetically shielded HET will experience erosion of the pole pieces, which can be remedied using sputter-resistant pole piece covers[11]. HET erosion is heavily dependent on the plasma properties near the boundaries and therefore plasma-material interactions play a major role in selecting long life materials.

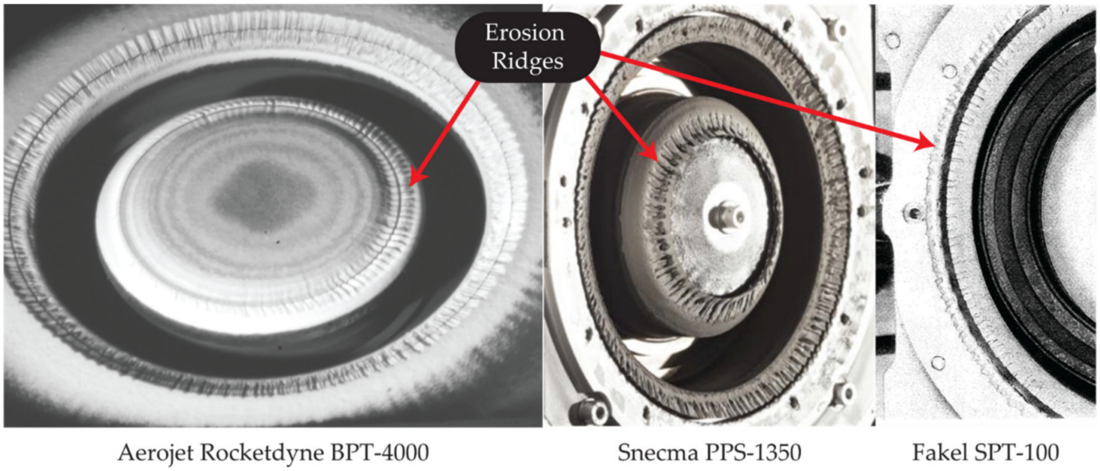

Figure 1.5: The images show the erosion ridges on the inner insulator rings of several Hall effect thrusters (Source: Brown and Walker (2020)).

1.1.1.3 Magnetoplasmadynamic Thrusters

Magnetoplasmadynamic (MPD) thrusters use a combination of electromagnetic acceleration ($J \times B$) and electrothermal heating to generate thrust. MPD thrusters are relatively simple devices consisting of a cathode and an anode as shown in Figure 1.6a and can have steady or unsteady operation. The large contact areas allow for large discharge currents to be driven between the electrodes resulting in high thrust (50 - 100 N) while maintaining high specific impulse (2000 - 7000 s) in the MW regime[12]. While highly attractive for heavy cargo missions requiring MW-class electric propulsion, current MPD thrusters are unable to meet the requirements of 50%+ efficiencies with sufficient lifetimes for such missions. The investigation of cathode erosion mechanisms and methods of erosion reduction are still an ongoing focus of research.

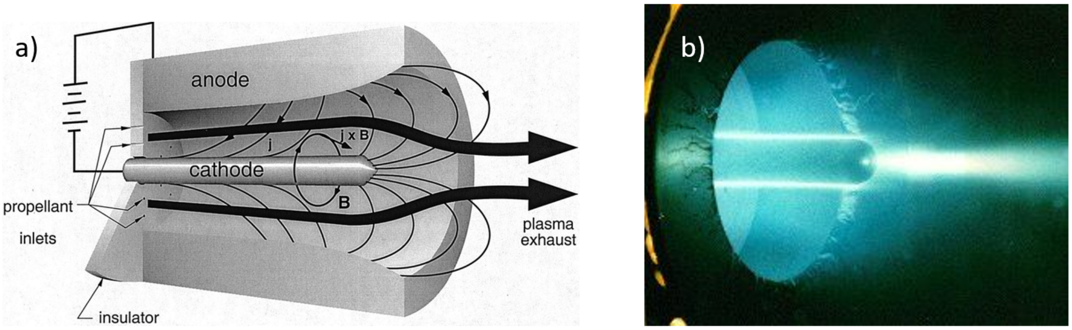

Figure 1.6: a) The configuration for a magnetoplasmadynamic thruster (Source: Jahn and Chouieri (2002)) and b) a steady magnetoplasmadynamic thruster operating on argon (Source: Princeton EPPDyL).

Figure 1.6b shows the operation of a steady-state MPD thruster operating with an argon propellant. The bright layer of plasma near the cathode indicates a large current density at the electrode. Schrade et al.[13] investigates the erosion behavior in a MPD thruster running in steady and quasi-steady modes. Their experimental findings revealed that the erosion process is differentiated between a spotty highly erosive mode and a diffusive low erosive mode. The spot mode process begins with a localized electric field concentration at a microprotrusion on the cathode surface. As the microprotrusion heats up, electrons are emitted from the low work function surface and a local plasma is generated with the full discharge current drawn through this spot. As additional spots are formed on the cathode, the full discharge current divides among the different spot emission sites. The majority of the spot erosion occurs in the early periods with few spot sites and large current densities.

The thermionic cathode attachment in the diffusive regime starts when the cathode is heated up and the tip begins to glow very brightly. The sublimation rate is shown to correlate with the cathode temperature and emission area. Schrade et al. measure the erosion rate and show there is a factor of 3 discrepancy between the rate predicted from sublimation and the measured rate. The difference is postulated to be due to the existence of instability and hot spot generation. The spot current densities are predicted to be on the order of $10^{12} - 10^{14}$ A/m^2. The diffusive mode is shown to be determined primarily by the localized erosion of small spots as well. Polk et al.[14] investigated the cathode erosion mechanisms experimentally using a thoriated thungsten cathode. They found that the temperature of the cathode are typically below the melting point of thoriated tungsten, and sputtering and evaporation dominated the erosion rate. Future efforts to maintain long life electrodes are needed to minimize the evaporative and sputter erosion before MPDs can be a viable technology for deep space exploration.

1.1.2 Nuclear Fusion Reactors

Nuclear fusion is a revolutionary technology that promises to produce unlimited clean energy for the world. By fusing atomic nuclei together, an enormous amount of energy is released which can be extracted to produce useful electricity. The nuclear fusion reactor concept is naturally motivated by the Sun which is powered by nuclear fusion processes in the core. In a massive body like the Sun, gravitational forces compress the center of the star to astronomical pressures ($\sim 10^{17}$ Pa) and temperatures ($\sim 10^{7}$ K). The high temperatures in particular facilitate nuclear reactions such as the following examples for typical deuterium-tritium plasma reactors:

$$\begin{aligned}
\mathrm{D + D} &\rightarrow \mathrm{T\ (1.01\ MeV) + p\ (3.03\ MeV)} && (1.2)\\
\mathrm{D + D} &\rightarrow \mathrm{He^{3}\ (0.82\ MeV) + n\ (2.45\ MeV)} && (1.3)\\
\mathrm{T{+}D} &\rightarrow \mathrm{He^{4}\ (3.52MeV) + n\ (14.06\ MeV)} && (1.4)\\
\mathrm{D + He^{3}} &\rightarrow \mathrm{He^{4}\ (3.67\ MeV) + p\ (14.67\ MeV)} && (1.5)\\
\mathrm{Li^{6} + n} &\rightarrow \mathrm{T + He^{4} + 4.8\ MeV} && (1.6)\\
\mathrm{Li^{7} + n\ (2.5\ MeV)} &\rightarrow \mathrm{T + He^{4} + n.} && (1.7)
\end{aligned}$$

The challenge in nuclear fusion is to generate more energy than is used to heat the plasma

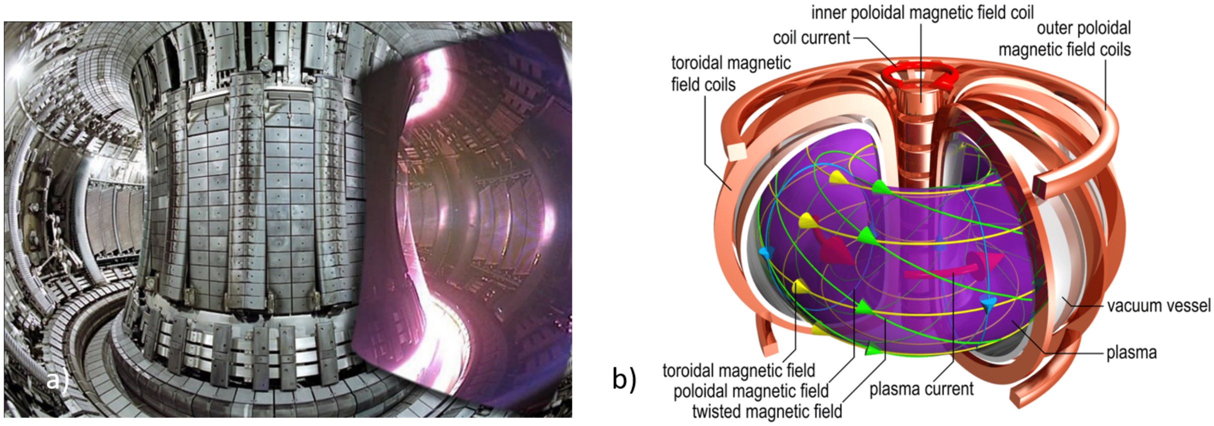

Figure 1.7: a) Internal view of the Joint European Torus (JET) reactor with an overlaid image of the plasma on. b) Tokamak schematic. Sources: JET and C. Brandt.

to fusion conditions. Since it is not feasible to create fusion plasma heated by gravitational energy like the Sun, many terrestrial fusion reactor concepts have emerged to create a net-energy positive power plant. Relevant devices with active areas of sputtering research include tokamaks, spheromaks, field-reversed configurations, and Z-pinch reactors, among others. In these devices, the lifetime of plasma-facing components and loss of energy through impurity radiation add additional challenges[15]. Due to high particle fluxes at the walls, a significant mass of plasma facing material is sputtered. Some fraction of this material is recycled in a erosion-redeposition process, but a large number of wall material is still transported to the core where energy is lost through Bremsstrahlung radiation. The reduction of wall erosion in reactors is one of the critical issues facing modern fusion reactors and advanced materials are currently being researched.

1.1.2.1 Tokamaks

Tokamaks are nuclear fusion reactors that utilize magnetic confinement to contain a thermonuclear plasma. As one of the most studied reactor designs, tokamaks have been shown to reach the densities, temperatures, and confinement times necessary for break-even energy production[16]. These efforts have led to the design of the International Thermonuclear

Experimental Reactor (ITER), a collaborative effort between many countries to produce a sustainable fusion energy source. Figure 1.7a shows an example of the interior of a tokamak.

The plasma in a tokamak are confined by a toroidal magnetic field superimposed with a poloidal magnetic field to give the characteristic "donut" shape as seen in Figure 1.7b. The toroidal field is produced by external magnets while the poloidal field is created by the large azimuthal current induced in the toroidal direction. The plasma is initially resistively heated using this azimuthal current, but this method loses its effectiveness at higher temperatures. Additional heating mechanisms such as neutral beam injection and microwave heating are used to bring the plasma to fusion temperatures.

A significant problem in tokamak reactors is the sputtering of the plasma-facing components (PFCs). When energetic ions are formed from either charge exchange or sheath acceleration processes, contaminants can be ejected from the wall due to sputtering. The introduction of impurity particles into the core plasma results in cooling and dilution. Since the particle fluxes to the walls are so large, the amount of impurities ejected into the core plasma can make it significantly more difficult to reach thermonuclear conditions. Additionally, the impurities can be transported in the plasma and subsequently ionized and redeposited elsewhere on the vacuum vessel. An altered surface composition will potentially result in tritium retention and negatively affect overall plasma properties.

The concentrated regions of sputtering in a tokamak are at the first wall and divertors as shown in Figure 1.8. The first wall is oriented parallel to the magnetic field lines where the adjacent region has a significantly lower density and temperature than the core plasma, known as the Scrape-Off Layer (SOL). In old designs, limiters were used in place of divertors and placed perpendicular to the magnetic field lines in order to intercept impurity fluxes, thereby leading to higher ion fluxes and more sputtering. Divertors are similarly used as impurity dumps, but these interfaces typically lie at the ends of magnetic field lines outside the primary torus. Therefore, divertors can have larger surface areas and the option for more control of the sputtered particles.

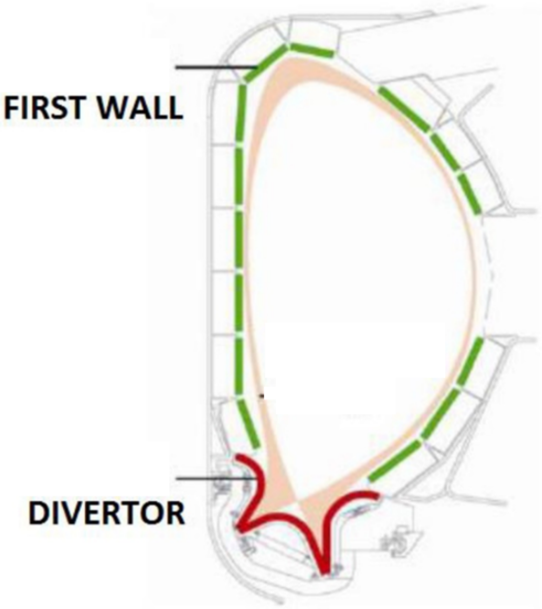

Figure 1.8: Schematic of a tokamak reactor. Source: Rieth et al. (2013).

The first walls are typically bombarded by energetic neutral atoms created by charge exchange processes. Since neutral atoms will retain their energy across magnetic field lines, the neutral energy distribution will have a large range from low energy to a high energy tail from ions in the core plasma. In contrast, the limiters and divertors intercept the magnetic field lines and therefore receives ion fluxes from the SOL plasma. Since the SOL plasma is cooled to 50-100 eV due to plasma-surface interactions, the ions accelerated through the sheath obtain energies of 100 to 300 eV[16].

The erosion rate of ITER is predicted to be on the order of cm/year or equivalently 1 ton/year of wall material[17]. Current methods of implementing flat sputter-resistant wall materials are insufficient, so there is a need to investigate advanced wall materials that can further reduce the sputtering yields.

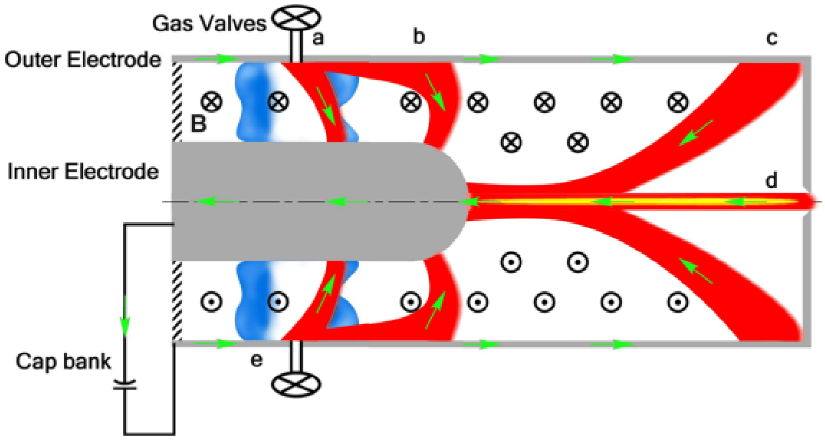

Figure 1.9: Schematic of a simplified Shear-Flow Stabilized (SFS) Z-pinch. Source: Zhang, Y. et al (2019).

1.1.2.2 Z-pinch Fusion Reactors

The Z pinch concept was originally developed as a simple means to create a high temperature plasma column. Figure 1.9 shows a simplified schematic of a shear-flow stabilized (SFS) Z-pinch. Gas is puffed into an annular vacuum chamber with a center cathode electrode. A capacitor drives a large current through the gas from the center cathode to outer anode electrode and the resulting $J \times B$ force accelerates the plasma axially. The axial plasma can be heated to thermonuclear fusion conditions. The SFS Z-pinch demonstrated by Zhang et al.[18] measured plasma densities of 10^{25} m^{-3} and ion temperatures of 1-2 keV with $\sim 10^5$ neutrons/pulse generated via fusion reactions in 5 μs. One of the main challenges facing Z-pinch reactors is the stabilization of non-linear hydrodynamic behavior associated with the fast implosion process. The shear-flow stabilization method which drives a sheared axial flow, dV_z/dr, enabled the first long-lived Z-pinch to be tested at fusion conditions[18].

The similarity of the Z-pinch geometry to MPD thrusters results in many of the same erosion phenomena. The center cathode electrode is subject to large electron currents, $\sim$ 100 kA - 1 MA, that can heat the cathode to non-negligible temperatures. Assuming the cathode operates below the melting point, the electrode will experience large sputtering and evaporation rates from the energetic ion fluxes in the attached plasma. In addition, the anode is subjected to similar erosion processes although it is spread out over a larger area. In general, the Z-pinch reactor is one of many fusion and propulsion applications [19] where a sputter-resistant material is necessary to achieve long-life and high performance operation.

1.2 Choosing the Right Materials

The plasma applications described previously have a variety of material requirements including structural, thermal, chemical, electrical, and financial considerations. For example, a plasma-facing material in a fusion reactor requires low sputtering yield, low atomic number, compatibility with plasma elements, low tritium retention, high melting point, high thermal conductivity, high strength, low activation by neutrons, and low cost[15]. The challenge of a material designer is to select materials that satisfy all of these requirements. On the other hand, the purpose of this thesis is to investigate optimal materials with one specific attribute: low sputtering yields in the energy range of interest.

1.2.1 Sputtering Yield Resources

The simple solution is to pick elemental materials with the lowest reported sputtering yields. The sputtering yield is the accepted metric for assessing the sputtering resistance of materials, presented in units of ejected atoms per incident ion or mm^3/C. Yamamura and Tawara (1996) compiled a comprehensive database of sputtering yields for many ion-atom combinations from low to high energies[20]. Data from the literature are fit with a semi-empirical equation that has been refined over the years. Details on the equations are presented in Chapter 2. Many more references have been added to the historical data over the years. Figure 1.10 shows examples of the sputtering plots presented in Yamamura and Tawara's manuscript. The argon ion on aluminum and molybdenum results are referenced throughout this dissertation. Note that the data must be interpreted with caution as the sputtering

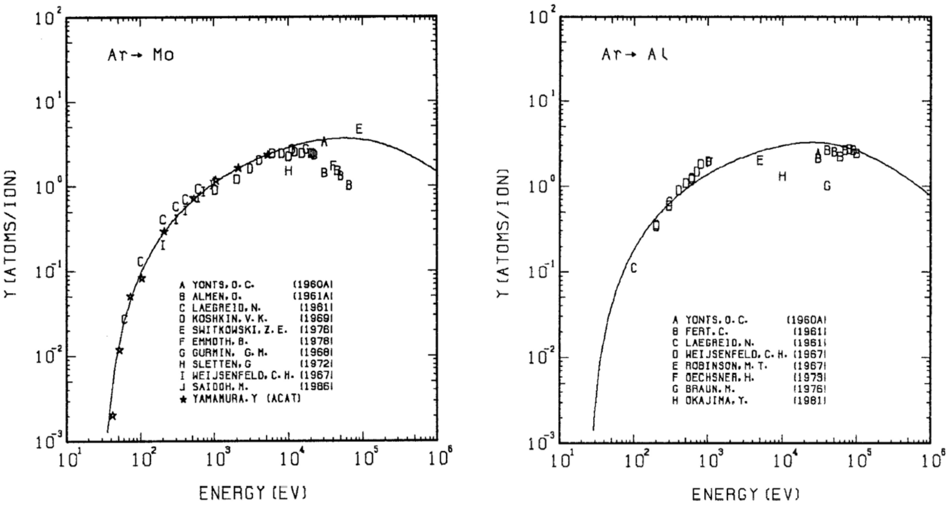

a) Argon on Molybdenum

b) Argon on Aluminum

Figure 1.10: Two examples of sputtering yield plots from Yamamura and Tawara (1996) are shown for a) argon ions on molybdenum and b) argon ions on aluminum.

yield values have a large spread due to variations in the experimental setup and sample preparation. These considerations are discussed in Chapter 3.

Another resource for finding low sputtering materials is the computational code Stopping and Range of Ions in Matter (SRIM), which includes the original code Transport of Ions in Matter (TRIM)[21, 22]. SRIM incorporates advancements in both theory and experiment to provide sputtering yield values for various ion-atom combinations. The results will presented in a similar fashion in the form of plots of yield versus energy as well. While the simulations will produce sputtering yield curves without experimental error bars, the results must also be interpreted carefully as discrepancies have been reported by several authors[23].

1.2.2 Structured Materials

In extreme cases with high ion fluxes or material limitations, it is insufficient to simply select a material with a low reported sputtering yield. One method of decreasing the sputtering yield even further is by adding roughness, i.e. microscopic surface features. The addition of grooves and protrusions allow ejected particles to be recaptured by the surface structures, resulting in a lower effective sputtering yield. The sputter-deposition process where sputtered particles travel in straight-line trajectories to intersect with local material features is known as ballistic deposition.

Rosenberg and Wehner[24] showed that the sputtering yield of a threaded nickel rod was substantially reduced compared to that of a smooth rod at the same ion energies. Ballistic deposition is found to be more pronounced at lower ion energies because the material is preferentially ejected at oblique angles, becoming trapped in the troughs of the threading. Huerta et al.[25] recently confirmed Rosenberg and Wehner's results computationally using a view factor model. It has also been shown that in certain cases, faceted structures can increase the overall sputtering yield[26, 27]. Therefore, the properties of the surface features determine whether the sputter yield is reduced or increased and to what degree.

Wehner and Hajicek[28] showed that microscopic cones were formed after bombardment of copper by molybdenum ions. The cones were closely packed and had a velvet-like configuration resulting in a lower overall sputtering yield compared to the previously flat copper. Building on these ideas, Cramer and Oblow[29] and Tetsuya et al.[30] proposed honeycomb vacuum walls for fusion reactors, showing a major reduction in yield. Clearly, features that result in obliquely emitted sputterants that are likely to intersect with adjacent structures are preferable for minimizing sputtering yield. The following subsection describes materials that aim to optimize the surface featuring for minimizing the yield.

Recently, the development of microfabrication processes has allowed materials engineers to intelligently design and control micro-featured surfaces. These micro-architectured materials can be created using the chemical vapor deposition (CVD) process using a variety of refractory metals, conventional metals, and insulators. By understanding sputtering theory, surfaces can be specifically engineered to minimize the overall sputtering yield. Ziegler et al.[31] tested a surface coated with dense tungsten whiskers and showed that the sputtering from a low energy helium plasma was reduced by a factor of 3 to 100. More recently,

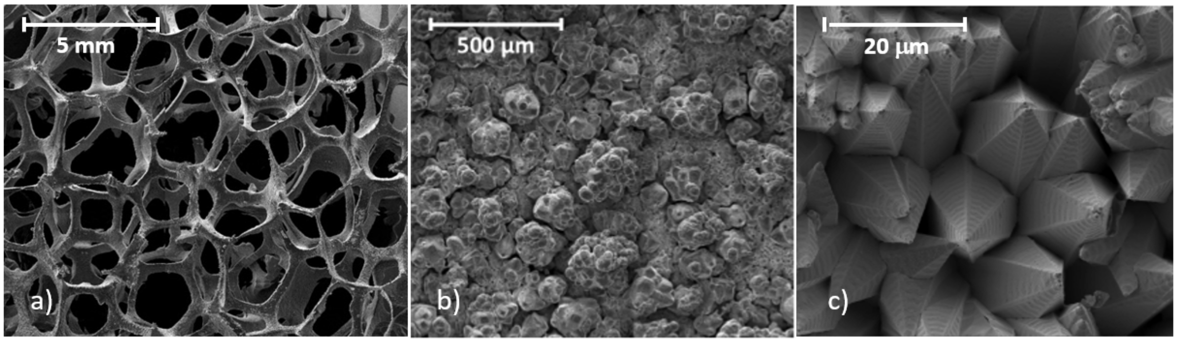

Figure 1.11: The three images above show a) reticulated foam b) fractal molybdenum nodules and c) dendritic spears. Figures b) and c) are from C. Matthes (2016)

Ghoniem et al.[32] has tested both tungsten and molybdenum surfaces with nano-rods and nano-nodules. The authors elaborate on the nano-architectured design and demonstrate a decrease in sputtering yield for all tested samples at both normal and oblique angles of incidence.

The three major categories of textured material surfaces as presented by Ghoniem et al.[32] and Matthes[33] are:

1. *Reticulated structures*

   Reticulated materials generally consist of mesh-like foams with open-cell cores that are connected by a network of ligaments. These foams are organized and uniform and can be either manufactured as pure metallic structures or deposited onto a skeletal framework. Therefore, the elemental composition can be chosen to either minimize sputtering yield, provide insulation, or maximize heat and electrical conductivity among other options. The main geometric properties of the foam are the porosity, which has units of Pores Per Inch (PPI), and relative density, which effectively determines the volume of ligaments. An SEM image of a reticulated foam sample is shown in Figure 1.11a.

2. *Fractal structures*

   Fractal structures are self-similar geometric features created from the surface texturing process. Figure 1.11b shows a molybdenum sample with self-similar nodules at the hundreds of micrometer scale. These structures protrude from the surface and cause sputtered material to intersect with adjacent structures. Ultramet Inc. produced the structured molybdenum sample tested in the present work.

3. *Dendritic structures*

   Dendrites are widely used fibrous micro-features that protrude from the surface. The specific geometry of the feature can range from needle-like nanorods to wide pillars, resembling velvets, spears, and nodules. The unique range of features result in many designs, such as the micro-spears shown in Figure 1.11c, that can allow for geometric trapping of sputterants. Many dendritic samples are manufactured by Ultramet Inc. which includes refractory metals deposited on rhenium substrates.

1.3 Thesis Objective

Many modern plasma devices are in need of advanced wall materials that can reduce the sputtering yield beyond what is currently possible with standard flat materials. Early work has demonstrated that surface roughness is effective at reducing the sputtering yield through geometric recapture of ejected particles. Armed with the knowledge of sputtering theory and modern manufacturing techniques, it is possible to intelligently design structured materials that can optimize the sputtering reduction. Therefore, it is the objective of this dissertation to investigate the behavior of plasma-sputtered structured materials for reducing the overall erosion rate for long-term plasma resilience.

1.4 Dissertation Overview

This dissertation is outlined as follows:

Ch 1 An introduction to plasma applications that require the development of advanced sputter-resistant wall materials, followed by the objective of my dissertation.

Ch 2 A discussion of the fundamental theories that will allow for a better understanding of the plasma sputtering experiments.

Ch 3 A summary of the design principles for a properly conducted sputtering experiment as well as a survey of sputtering yield diagnostics.

Ch 4 A description of the Plasma interactions test facility at UCLA along with details on the sputtering yield diagnostics and material samples.

Ch 5 The results of both a benchmark experiment on a characterized flat sample and a novel micro-architectured molybdenum sample.

Ch 6 An introduction to plasma-foam sputtering theory and the results from an aluminum foam sputtering experiment.

Ch 7 An analytical model is introduced to discuss the key physical mechanisms in the plasma sputtering of foams and the experimental results from the previous chapter are analyzed within this framework.

Ch 8 A conclusion of the dissertation along with a discussion of future work.

CHAPTER 2

Plasma Sputtering Theory

In this chapter, general concepts relevant to the topic of plasma sputtering are introduced to motivate and better understand the experimental investigations. Many complex phenomena exist in the plasma-material boundary, so sputtering is first discussed in the context of plasma-material interactions. Plasma sheath and sputtering theory are then presented. The discussion focuses on the physics relevant for physical sputtering in the low energy (≤ 1 keV) heavy ion regime with a particular emphasis on the angular sputtering distributions. The chapter concludes with a discussion of the erosion reduction mechanisms present for the plasma sputtering of structured materials.

2.1 Plasma-Material Interactions

Sputtering is a subset of plasma-material interactions (PMI), a phenomena-rich field involving plasma particles, radiation, and their boundaries. Figure 2.1 shows examples of several interactions that can occur between the plasma species, including ions, electrons, neutral particles, and radiation, with the material surface. Naujoks provides a comprehensive reference of PMI for nuclear fusion[15].

Bombarding particles can be backscattered into the plasma, or implanted into the wall and cause the release of surface particles. For ions and neutral particles, backscattering occurs if the sticking coefficient is less than unity, implantation is common if the ions and neutrals are much heavier than the wall particles, and sputtering is possible when the incident energy is higher than the surface binding energy. Ejected atoms or sputterants can be

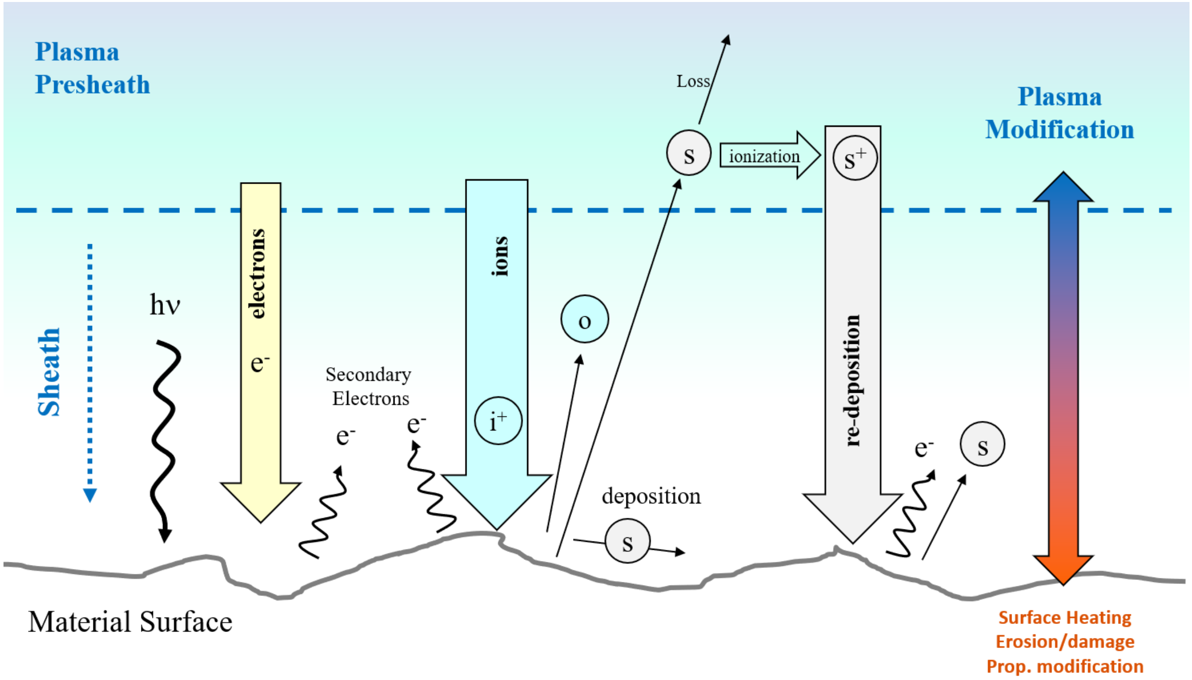

Figure 2.1: Examples of plasma-material interactions. The o particles are neutrals, s particles are sputterants, $h\nu$ is radiation, and e^- and i^+ are electrons and ions respectively.

recycled via transport in the plasma and subsequent ionization and deposition back on the surface in a process known as plasma redeposition[34]. Ions can also cause the release of electrons in ion-induced electron emission[35]. Electrons can also backscatter, implant in the surface, or cause the release of secondary electrons[36].

In addition to particle coupling, power can also be transferred between the plasma and the material. Ion, electron, and radiation heating of the surface can lead to melting and sublimation[15]. For low work function materials, a sufficiently high temperature can also lead to thermal emission of electrons[37]. At the plasma-material boundary, the sheath acts as a transport layer between the plasma and wall for power and particle fluxes. As both an accelerating and boundary layer medium, the plasma sheath plays a large role in the plasma sputtering of materials and PMI as a whole.

2.2 Sheath Theory

At any plasma-material interface, there exists a boundary layer known as the plasma sheath where an electric field exists due to an imbalance of the ion and electron fluxes to the wall. The understanding of sheaths has led to advances in semiconductor devices, erosion and performance issues in electric propulsion and nuclear fusion, Langmuir probes, spacecraft charging, among many other applications. Needless to say, sheaths are important for understanding plasma-material interactions[38].

2.2.1 Debye Sheaths

The Debye length, λ_D, is the most fundamental scale length in a plasma. It describes the characteristic radial distance required to shield, or screen out, a test charge placed in a quasineutral plasma. Figure 2.2 shows a positive test charge with a "Debye sphere" of zero net charge in a bulk plasma. Inside the sphere, there is a potential well, i.e. electric field, from the test charge, but the potential perturbation in the plasma is shielded beyond a distance of λ_D.

The traditional derivation of the Debye length is available in many plasma physics textbooks[39]. The electric field in the Debye sphere is found from Poisson's equation:

$$\nabla^2\phi = -\frac{\rho}{\epsilon_0} = -\frac{e}{\epsilon_0}(Zn_i - n_e), \tag{2.1}$$

where ϕ is the electric potential, ρ is the charge density, Z is the ion test charge, and $n_{e,i}$ are the ion and electron densities. Assume singly charged ions and small potential perturbations ($e\phi \ll kT_e$) with Boltzmann electrons and quasineutrality ($n_i \approx n_0$). The Boltzmann density for thermal electrons is

$$n_e = n_0 \exp\left(\frac{e\phi}{kT_e}\right) \approx n_0\left(1 + \frac{e\phi}{kT_e}\right), \tag{2.2}$$

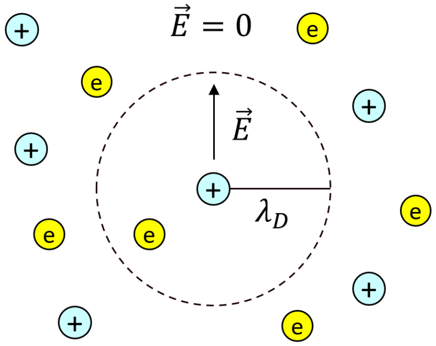

Figure 2.2: Debye shielding.

where the expression is expanded in a Taylor series neglecting terms of $\mathcal{O}((e\phi/kT_e)^2)$. Plugging into Poisson's equation in spherical coordinates, the resulting differential equation for the potential is

$$\frac{1}{r^2}\frac{\partial}{\partial r}\left(r^2\frac{\partial \phi}{\partial r}\right) = \frac{n_0 e^2}{\epsilon_0 k T_e}\phi = \frac{1}{\lambda_D^2}\phi. \tag{2.3}$$

Knowing that the potential for a point charge is

$$\phi(r) = \frac{1}{4\pi\epsilon_0 r} \tag{2.4}$$

the differential equation can be solved to find

$$\phi(r) = \frac{1}{4\pi\epsilon_0 r}\exp\left(-\frac{r}{\lambda_D}\right). \tag{2.5}$$

The potential is seen to have the same $1/r$ decay as a standard point charge with an additional exponential decay factor due to the plasma shielding effect. The Debye length is the characteristic decay length. Although this derivation was based on a point charge in spherical coordinates, the Debye length will be found to be the key scale length in sheaths.

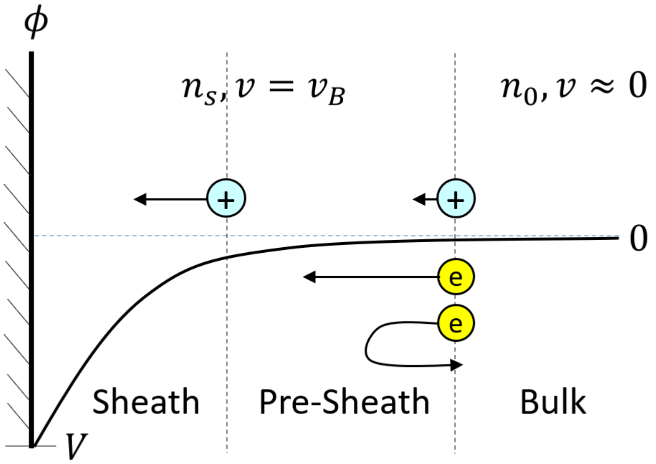

Figure 2.3: 1D sheath structure.

2.2.2 Child-Langmuir Sheath

While Debye sheaths are calculated for minor potential perturbations in the plasma ($e\phi \ll kT_e$), Child-Langmuir sheaths form when the potential difference is much larger than the electron temperature ($e\phi \gg kT_e$). Child-Langmuir sheaths, i.e. ion sheaths, are space-charge limited regions where all ions fall into the potential well and gain energy equal to the potential difference while electrons are largely repelled. Although sheaths can also be positive-going, i.e. electron sheaths, the Child-Langmuir sheath is the regime encountered in plasma sputtering. A wall that is negatively biased or even floating will often accelerate ions above the sputtering threshold energy and cause sputtering to become significant.

Figure 2.3 shows the general structure of an ion sheath. The bulk plasma region is quasineutral with and ions are assumed to be cold ($v_i \approx 0$). The plasma is assumed to be weakly collisional and magnetic fields are neglected. Ions with near-zero thermal velocity are directed into the pre-sheath region and accelerated to the Bohm velocity, $v_B = \sqrt{kT_e/M}$, at the sheath boundary, where M is the ion mass. The Bohm velocity is derived from the Bohm criterion which states that ions must fall through a potential difference of $kT_e/2e$ before entering the sheath in order to ensure a monotonically decreasing sheath potential[38].

Therefore, the ion velocity at the sheath entrance is typically assumed to be equal to the Bohm velocity.

Since the ion flux is conserved throughout the sheath, the current density, $J_i = n_s e v_B$, can be calculated at the sheath boundary. The pre-sheath is also quasineutral so the ion density can be found from the Boltzmann electron density and the potential drop in the pre-sheath of $kT_e/2e$

$$n_s = n_0 \exp\left(\frac{e\Delta\phi}{kT_e}\right) \approx 0.606 n_0. \tag{2.6}$$

The corresponding ion current density is

$$J_i = 0.6 n_0 e v_B \approx \frac{1}{2} n_0 e \sqrt{\frac{kT_e}{M}} \tag{2.7}$$

which can be used to find the ion density in the sheath as a function of position, ϕ,

$$n_i(x) = \frac{J_i}{ev(x)} = \frac{J_i}{e\sqrt{2e\phi/M}}. \tag{2.8}$$

Similar to the Debye sheath derivation, Poisson's distribution can be applied. Assuming no electrons, Poisson's equation gives

$$\frac{d^2\phi}{dx^2} = -\frac{n_i(x)e}{\epsilon_0} = -\frac{J_i}{\epsilon_0\sqrt{2e\phi/M}}. \tag{2.9}$$

Multiplying by $d\phi/dx$ and integrating twice gives

$$J_i = \frac{4\epsilon_0}{9}\sqrt{\frac{2e}{M}}\frac{V^{3/2}}{L_s^2}, \tag{2.10}$$

which is also known as Child-Langmuir's law[40, 41]. The equation can be arranged to solve for the sheath thickness, L_s, in terms of the Debye length to be

$$\frac{L_s}{\lambda_D} = \frac{\sqrt{2}}{3}\left(\frac{2eV}{kT_e}\right)^{3/4}. \tag{2.11}$$

The Child-Langmuir sheath thickness is a function of the characteristic Debye shielding length and scales with $V^{3/4}$. Typically, $L_s \sim 5 - 20\lambda_D$ for low temperature plasmas. Larger wall voltage drops will result in a thicker sheath. In this dissertation, the sheath thickness will play a major role in determining the plasma sputtering behavior as discussed in Chapter 6.

2.3 Sputtering Theory

Sputtering is the process by which particles from a solid material target are ejected due to bombardment by energetic particles including atoms, ions, and molecules. Due to the convenient mechanism of electrostatic acceleration, ions are typically the energetic particles used for sputtering experiments, although it's been shown that atom and ion sputtering yield nearly identical effects. If the ion is non-reacting, e.g. a noble gas, and singly-charged then the ion-solid interaction, termed physical sputtering, is purely via momentum exchange and only involves collisions as opposed to chemical or quantum effects. When the energy of the impacting ion exceeds the sputtering threshold energy, there exists a finite probability that an atom or molecule will be ejected from the target. The erosion rate is characterized by a statistical quantity known as the sputtering yield, which is defined as the average number of atoms ejected per incident ion as below:

$$Y = \frac{\Gamma_a}{\Gamma_i} = \frac{\text{atoms ejected}}{\text{ions incident}} \tag{2.12}$$

where $\Gamma_{a,i}$ are the fluxes of ejected atoms and incident ions respectively.

Physical sputtering consists of three different regimes shown in Figure 2.4 that depend on the energy of the incident ion[42]. For low energy sputtering near threshold (E $\lesssim$ 100

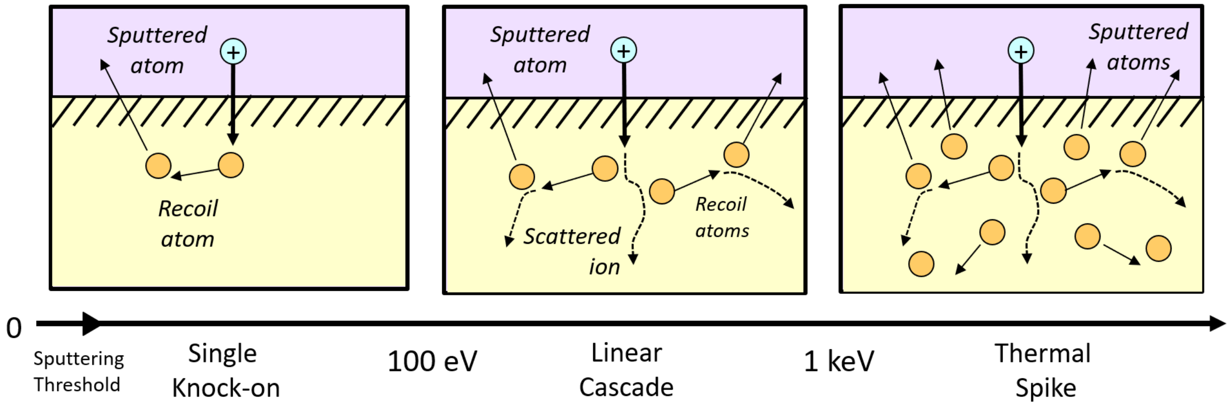

Figure 2.4: Sputtering regimes.

eV), the sputtering is in the single knock-on regime where the ion collides with a surface atom which is then set into motion. The recoiling atom, called the primary knock-on atom, can collide with additional surface atoms and possibly transfer sufficient energy to overcome the surface binding energy, U_b, and result in sputtering. If the energy of the ion is slightly higher (100 eV $\lesssim$ E $\lesssim$ 1 keV), the ion may have enough kinetic energy to start a collision cascade. In this scenario, several surface atoms can be set into motion simultaneously and generate higher order recoil atoms which may then obtain energy to overcome the surface binding energy. The energy is ultimately dissipated by heat when the energy transfer reaches the lattice binding energy. For the highest energy ions (E $\gtrsim$ 1 keV), the sputtering is in the thermal spike regime where a majority of the nearby surface atoms are already in motion. In other words, there is localized melting of the material and larger amounts of atoms, potentially even clusters, can be ejected. For the experiments performed in this work, the sputtering processes will be in the primary knock-on and linear cascade regimes.

In addition to the characteristic energies, E and U_b, there are two characteristic depths for sputtering[43]. Since the ion penetrates the surface, the collision cascade events that lead to sputtering typically occur at some distance into the material. This first characteristic length is equal to some fraction of the ion range and increases with ion beam energy, E. Secondly, there is the depth at which sputtered atoms are emitted. For single knock-on and linear collision cascade events, this occurs very close to the surface and is only weakly dependent on external conditions[43]. For thermal spike events, the behavior is non-linear and sputtered particles can originate from near the surface to deeper into the material.

In the most fundamental description, physical sputtering is modeled by hard-sphere collision with completely elastic scattering. However, in the limit of low energy sputtering, the collisions involve screened Coulomb and electronic interactions which are inelastic effects that introduce additional energy losses. Therefore, the nuclear stopping power, which determines the energy loss of the incident ion through the material, is highly dependent on the atomic model used for the energy transfer calculation[44]. In the following section, several analytical approaches to calculating the sputtering yield are discussed.

2.3.1 Sputtering Yield Equations

In 1969, Sigmund published a comprehensive solution for physical sputtering based on transport theory[42]. Assuming the interaction took place in the linear cascade regime for random slowing of an ion in an infinite monatomic medium, the linearized Boltzmann equation can be solved for the sputtering yield as a function of ion energy and varying ion-target combinations. A rigorous derivation can be found in Ref. [42]. The solution for normal incidence is shown to be:

$$Y(E) = \frac{0.042}{U_s} \alpha \left(\frac{M_2}{M_1} \right) S_n(E), \tag{2.13}$$

where U_s is the sublimation energy, α is a fit parameter based on the ion-target mass ratio, and $S_n(E)$ is the nuclear stopping cross section. The Sigmund formula above is valid for collisions in the linear cascade regime, but may not apply for the single knock-on regime closer to the sputtering threshold. However, the general derivation performed by Sigmund is flexible and several semi-empirical adaptations have been implemented for better agreement with experimental data as described in detail in Appendix A. The sputtering yield is found to depend on the ion-atom combination and more specifically the ratio of the masses, M_2/M_1. The analogy can be traced back to the canonical problem of billiard ball interactions between a heavy mass and a light mass. In this dissertation, the mass-dependency is fixed and the energy dependence is investigated.

Matsunami et al.[45] adapted the Sigmund formula to include low energy effects through the additional term below

$$Y(E) = \frac{0.042}{U_s}\alpha\left(\frac{M_2}{M_1}\right)S_n(E)\left(1 - \sqrt{\frac{E_{th}}{E}}\right), \tag{2.14}$$

where E_{th} is the sputtering threshold energy. Experimental studies showed that the sputtering yield decreased to zero, or below the detection threshold of the measurements, at some characteristic energy which is now referred to as E_{th}. The threshold energy was found to be larger than the sublimation energy, U_s, and is usually empirically determined. Equation 2.14 modifies Sigmund's original expression with a simple term that drops to zero at E_{th} with a $-E^{-1/2}$ dependence. The empirical equations for the sputtering yield are derived for flat surfaces that neglect surface roughness. Structured materials will reduce the flat sputtering yield but will retain some of the physical dependencies such as the low energy behavior near the sputtering threshold.

2.3.1.1 Sputtering Yield at Glancing Incidence

Several semi-empirical models for the angle of incidence dependence of the total sputtering yield have also been developed. Early measurements were performed by Wehner where metal spheres were bombarded by a low energy mercury ion beam and the relative sputtering yield was measured via thickness changes in shadow micrographs[46]. He found that all materials had an off-normal angular peak in sputtering yield and that certain materials had more pronounced angular effects than others. The dependence on ion-target mass ratios and an off-axis peak yield were found to be fundamental dependencies in following work. In addition, Sigmund predicted that the yield ratio, $Y(\theta)/Y(0)$, was proportional to $\cos^f\theta$ at near-normal angles of incidence where $1 < f < 2$[42].

Yamamura and Shindo extended Sigmund's treatment to account for the full range of polar angles, $0° < \theta < 90°$, with an analytic empirical formula[47]. The equations differ between light-ion sputtering, which is based on collision cascades propagating from the interior of the material, and heavy-ion sputtering, where collision cascades are generated near the surface. For light ions, the empirical equation takes on the form:

$$\frac{Y(\theta)}{Y(0)} = x^f \exp[-\Sigma(x-1)] \tag{2.15}$$

where $x = 1/\cos\,\theta$ and f and Σ are fit parameters. The optimum angle for maximum sputtering yield can be found from

$$\cos\,\theta_{\text{opt}} = \cos^{-1}\left(\frac{\Sigma}{f}\right). \tag{2.16}$$

For heavy-ion sputtering, the effect of the threshold energy is included as follows:

$$\frac{Y(\theta)}{Y(0)} = x^f \exp[-\Sigma(x-1)]\left[\frac{1-(E_{th}/E)^{1/2}/x}{1-(E_{th}/E)^{1/2}}\right]. \tag{2.17}$$

However, Yamamura and Shindo note that the threshold energy, E_{th}, has not been well established due to the lack of accurate experimental data in the low energy sputtering regime. Therefore, the common practice is to use Equation 2.15 and include the threshold effects in the fit parameters. Another empirical formula is derived by Wei et al. (2003):

$$\frac{Y(E,\theta)}{Y(E,0)} = \cos\,\theta\,\exp\left(\frac{a^2\sin^2\,\theta}{2\alpha^2}\right) \tag{2.18}$$

where a is the projected energy range and α is the energy range straggling. Wei et al. fit the equation to several datasets by adjusting a and α, showing many of the same qualitative features as Equation 2.15 such as the optimal peak yield angle and the decay to zero yield at 90°. Similarly to Yamamura's formula, Equation 2.18 extends Sigmund's original cosine scaling to a wider range of polar angles and serves as an appropriate fit for many atom-ion sputtering combinations. However, one major limitation is that both these formulae remain empirical and have difficulties incorporating the energy dependence near the sputtering threshold. Given these caveats, the equations will be utilized in the interpretation of experimental data in the following chapters.

2.3.2 Angular Sputtering Distributions

In addition to formulations for sputtering yield as a function of energy, the angular distribution of sputtered particles has also been obtained both theoretically and with empirical modifications. Yamamura[48] derived the first empirical formula based on the original theory by Sigmund to be:

$$\begin{aligned} S(E,\theta,\alpha) &= 0.042\frac{\alpha'(M_2/M_1,\theta)S_n(E)}{U_s}\cos(\alpha) \\ &\times \left[1-\frac{1}{2}\left(\frac{E_{th}}{E}\right)\left\{\cos(\theta)\gamma(\alpha)+\frac{3}{4}\pi\sin(\theta)\sin(\alpha)\cos(\phi)\right\}\right] \end{aligned} \tag{2.19}$$

where

$$\begin{aligned} \gamma(\alpha) = \frac{3\,\sin(\alpha)^2-1}{\sin(\alpha)^2} \quad &+ \quad \frac{\cos(\alpha)^2(3\,\sin(\alpha)^2+1)}{2\,\sin(\alpha)^3}\times \\ &\ln\left[\frac{1+\sin(\alpha)}{1-\sin(\alpha)}\right], \end{aligned} \tag{2.20}$$

and θ is the incident angle of the ion and α and ϕ are the emitted polar angle and azimuthal angle of the sputterant respectively. Zhang and Zhang[49] showed that Yama-

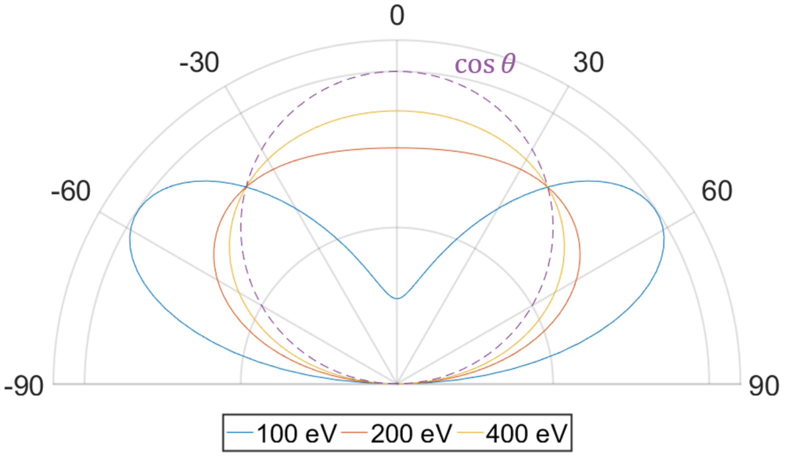

Figure 2.5: Normalized angular sputtering distributions calculated using Equation 2.21 with $E_{th} = 50$ eV. The standard cosine profile is shown as a reference.

mura's derivation included an inconsistency with the threshold energy, E_{th}, and revised Equation 2.19 to be:

$$\begin{aligned} S(E,\theta,\alpha) &= 0.042\frac{\alpha'(M_2/M_1,\theta)S_n(E)}{\pi U_s}\cos(\alpha) \\ &\times \left[1-\frac{1}{4}\left(\frac{E_{th}}{E}\right)\left\{\cos(\theta)\gamma(\alpha)+\frac{3}{2}\pi\sin(\theta)\sin(\alpha)\cos(\phi)\right\}\right] \end{aligned} \tag{2.21}$$

where $\gamma(\alpha)$ is defined in the same way as above. The integration of Equation 2.21 in spherical coordinates yields Equation 2.14 for the special case of normal ion incidence ($\theta = 0$). Figure 2.5 shows several sputtering profiles with a threshold energy of 50 eV. The well-known cosine profile at high ion energies (≥ 1 keV) is shown as a reference. The sputtering profiles can be generally described as under-cosine or butterfly distributions, with maximum probabilities at an off-normal angle. This low energy behavior is well-known and has been measured experimentally[49]. However, there remains ambiguity regarding the E_{th} value for various ion-atom combinations. Typically, the empirical equations are fit to experimental data and E_{th} is used as a best-fit parameter rather than a physical characteristic energy.

The low energy angular behavior will be essential for understanding the sputtering behavior for structured materials.

2.4 Sputtering Reduction via Geometric Structuring

The principles of ion acceleration in a plasma sheath and angular sputtering distributions can be used to understand the sputtering reduction of structured materials. Figure 2.6 shows examples of ion incidence on two types of surface features. Figure 2.6a shows an ion normally incident on the trough of a rectangular groove. The angular distribution for low energy sputtering is a butterfly-shaped profile with the highest ejection probabilities at an off-normal angle, in contrast to cosine sputtering as shown in Figure 2.5. By increasing the depth of the groove, the probability of recapturing the sputtered atom can be increased. Additionally, the recapture probability will depend on the sticking coefficient of the surface which may vary from negligible to near unity. The sticking coefficient for many metals is known to be near unity[50]. Figure 2.6b shows an ion incident on the sloped surface of a faceted surface feature. The corresponding angular distribution is known to be preferentially forward-biased, allowing the ion to have the highest probability of remaining within the line-of-sight of recapture within the faceted groove. The deposition of the sputtering atoms over time will result in evolution of the surface features depending primarily on the geometry, ion energy, and ion-atom combination.

In general, sputtering reduction via geometric structuring can be achieved on the microscale or macroscale. Sigmund first theorized that a microscopically flat surface is unstable under energetic ion bombardment[51]. The surface topography will evolve depending on the sputtering yield at oblique incidence, crystallographic orientation, and defect states. Bradley and Harper[52, 53] further advanced the theory to demonstrate ripple growth of the surface which equates to a micro-roughened surface. Huerta et al.[25] demonstrated the effects of macroscale vs microscale roughening by comparing the normalized sputtering yield

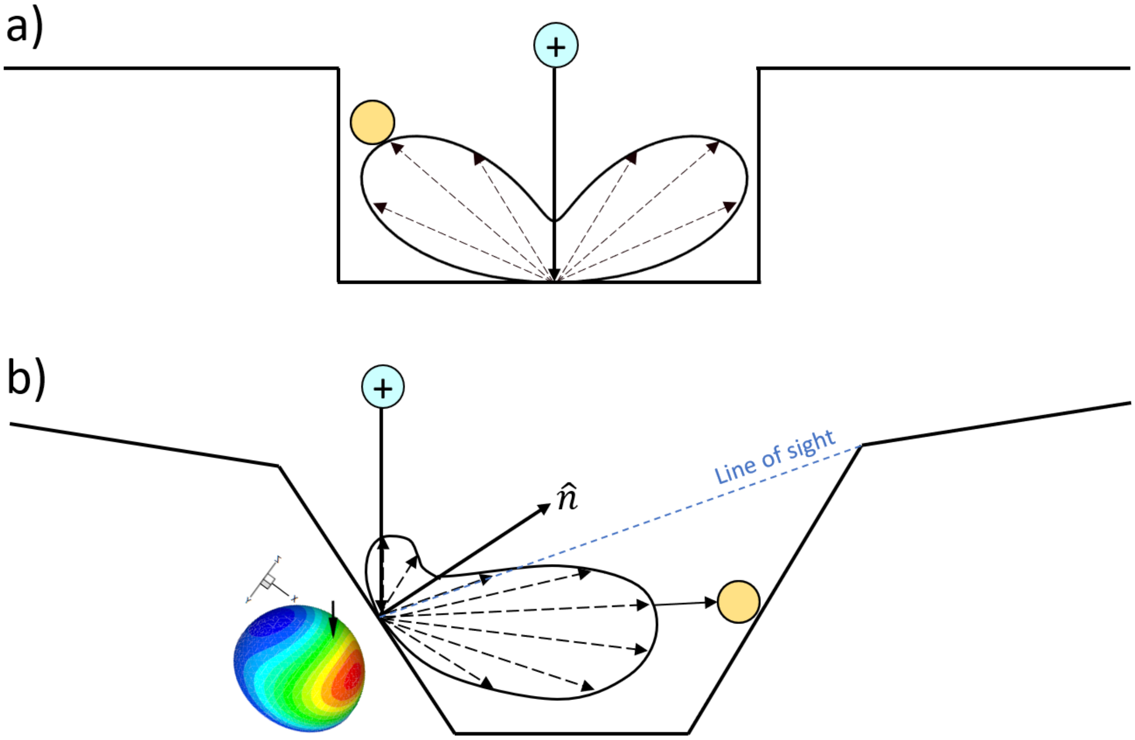

Figure 2.6: Sputtering reduction for two examples of surface featuring: a) normal ion incidence on a rectangular groove and b) oblique ion incidence on a sloped surface resulting in ballistic deposition on adjacent surfaces.

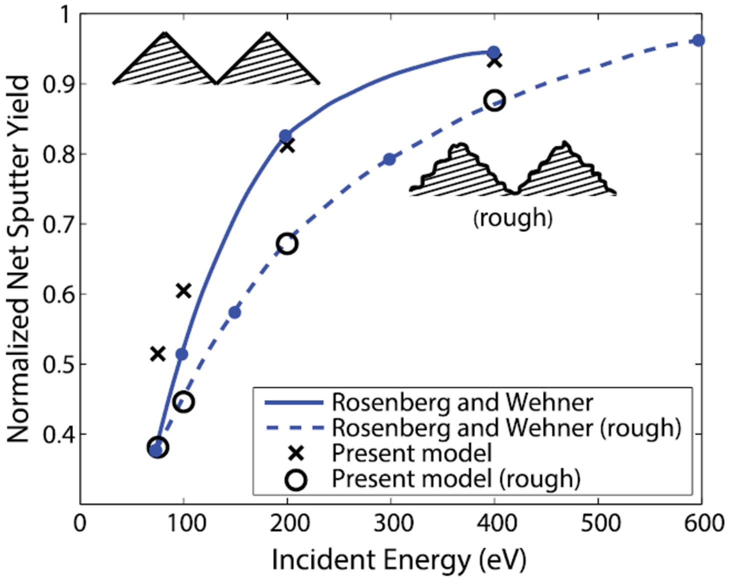

Figure 2.7: The normalized sputtering yield of a ridged surface with and without micro-roughening. The results of a computational model are compared to the experimental data of Rosenberg and Wehner. Source: Huerta et al. (2016)

of a micro-roughened ridge surface to the smooth equivalent as shown in Figure 2.7. The results indicate that both the smooth and micro-roughened surface reduce the sputtering yield compared to a flat surface, and that the micro-roughening provides an additional reduction. Therefore, it can be seen that both macroscale and microscale surface featuring will play a role in the reducing the effective sputtering yield. The implications are endless as the advent of modern manufacturing techniques as discussed in Chapter 1 enable unprecedented control over the material design.

2.5 Summary

At a plasma-material interface, ions are accelerated through the plasma sheath. Ions incident on the surface will result in physical sputtering, a mechanism that has been extensively studied in the past few decades. Semi-empirical formulas in the low energy sputtering regime have been successfully validated on experimental data. While there are still unresolved issues in sputtering theory, particularly that of surface evolution, the sputtering yields and angular distributions of various materials have been characterized in detail. The knowledge gained from past work allows designers to create micro-architectured materials that can take advantage of the angular sputtering distributions in the low energy regime. In particular, geometric trapping using featured surfaces can significantly reduce the effective sputter yield. The discoveries presented in this dissertation are based on this foundational concept.

CHAPTER 3

Design of Sputtering Experiments

The sputtering yield can be measured using a variety of experimental setups, each with its own advantages and disadvantages. The simplified picture consists of (1) an ion source, (2) a material target, and (3) a sputtering yield diagnostic all enclosed in a vacuum facility. Although the setup seems simple, there are many complicating effects that make acquiring a pure measurement of the sputtering yield extremely difficult. As a result, there is a large spread in the sputtering yields reported in literature even when using similar experimental designs. In this chapter, I'll introduce the most common elements of sputtering measurement setups, with a focus on the methods utilized in my dissertation research.

3.1 General Experimental Setup

3.1.1 Test Facility

Since the high pressure and low ambient temperature of atmospheric plasmas obfuscate the sputtering process, measurements of sputtering yield are typically performed in vacuum facilities. By reducing the background pressure below approximately 10^{-5} Torr, the scattering of incident ions and chemical reactions of background gases with the material target can be minimized. In particular, the low background pressure minimizes the probability of forming a chemisorbed impurity layer on the sample surface. A typical vacuum chamber uses a combination of roughing pumps and high vacuum pumps to reach the desired background pressures, and a residual gas analyzer (RGA) can used to assess the partial pressures of "contaminant" background gases such as water or oxygen. By removing background effects, the complicating factors can be reduced to plasma effects, if any, and the nuances of the measurement technique.

3.1.2 Ion Sources

Sputtering is a process that depends heavily on the properties of the incident ions. Therefore, it is essential to identify an ion source that matches the requirements of the experiment. Some of the considerations include the ion energy, the angle of incidence, the ion charge and mass, the background conditions associated with the ion source, and the ion current density. In the early days of sputtering experiments[24], plasma discharges were the method of choice due to their high current densities and ability to clean the target in real-time. However, over time, ion beams began to gain in popularity because of their well-defined beam properties, such as spot size and narrow energy distribution. These two ion sources are described in detail in the following sections.

3.1.2.1 Plasma Discharges

In a plasma sputtering experiment, the material target is immersed in a high density direct current (dc) plasma and the incident ions are accelerated by electrically biasing the conducting target relative to the plasma potential. By measuring the plasma potential with plasma probes, the ion energy to the target can be determined to an order of accuracy of the electron temperature (4-7 eV). This level of accuracy is perfectly acceptable for sputtering experiments with ion energies above 100 eV. In the plasma sheath, the acceleration of ions occurs in the direction normal to the target. For a flat sample with roughness much less than the Debye length, the acceleration is normal to the entire surface resulting in uniform normally incident ion impingement. The normally incident ions can also impact the rough surface features at oblique angles of incidence. For a surface with micro-features on the order of the Debye length or larger, the sheath can conform to the sample surface. In this scenario, the ions are accelerated relative to the local target normal vector. Depending on the experimental objectives, this effect may or may not be desirable.

The main benefit of plasma discharges is the high current densities deliverable to the target. The ion current density to a surface can be estimated by the Bohm current:

$$j_B = \frac{1}{2} n_e e \sqrt{\frac{k_B T_e}{M}}. \tag{3.1}$$

The typical current density in a xenon plasma with $n_e = 10^{17}$ m^{-3} and $T_e = 5$ eV will be around 15 A m^{-2} or 1.5 mA cm^{-2}. This value can be compared to that of the ion beams described in the following section. In test campaigns where materials require high ion fluences, a large ion current density is necessary for the test to completed within a practical amount of time. For example, a sample with a micro-architectured surface will have a transient sputtering yield that changes with the evolving surface morphology. To acquire a complete trace of the sputtering yield curve as a function of time, the sample will need to be eroded until the surface is flat. For sputter-resistant materials tested at UCLA, this process has taken on the order of days using a plasma discharge. In comparison, an ion gun which has a current density an order of magnitude lower could take weeks to complete a single test. Another benefit of plasma discharges is the ability to clean the target surface in real time. Contaminants that deposit on the sample will likely be sputtered off by the plasma due to the high current densities. Finally, the background plasma electrons can also excite the ejected sputterants allowing for spectroscopic measurement of the sputtering yield.

However, sputtering experiments with plasma discharges have several limitations. Firstly, the plasma background can complicate the sputtering yield measurements since the sputterants must travel through the plasma. Due to the electric field in the plasmas sheath, there is a non-negligible probability that the particles will be ionized and be redirected back to the target. This effect, known as plasma redeposition, can result in an underestimation of the sputtering yield. Since ionization scales with electron density and temperature, the plasma must be restricted to lower densities and temperatures to keep the plasma redeposition effect below 10%[54]. If the target is fully immersed in the plasma, the incident ion conditions may not be well-defined near the corners where the sheath begins to curve[55]. Additionally, hotter plasmas may also have multiply-charged species that cannot be filtered as in an ion beam. These multiply-charged ions will result in an overestimation of the singly-charged ion sputtering yield at a given energy. Typically, the multiply-charged ion content is measured using an $E \times B$ probe or via emission spectroscopy to quantify the error. The emitted radiation can also affect the target surface by heating or radiation damage. Finally, the energetic ion bombardment will result in secondary electron emission which can distort direct current measurements. If the secondary electron emission (SEE) yield is known from experiments, the measured current can be corrected in post-processing. However, for many experiments, SEE is taken to be an uncertainty on the sputtering yield measurement.

3.1.2.2 Ion Beams

Ion beams are typically created by extracting ions from a plasma through electrostatic grids. As Kaufman describes[56], most ion sources contain the same elements as that of a gridded ion thruster. First, a plasma is generated via electron-bombardment from a direct current (dc), radiofrequency (rf), or microwave-based ionization in a discharge chamber. The ions are then extracted from the plasma via a set of electrostatic grids with the accelerator grid biased negative relative to the plasma potential. The maximum current density through each gridlet is determined by the Child-Langmuir Law:

$$J_i = \frac{4\epsilon_0}{9}\left(\frac{2e}{M}\right)^{1/2}\frac{\phi^{1/2}}{d^2}, \tag{3.2}$$

where J_i is the gridlet current density [A/m^2], ϵ_0 is the permittivity of free space, M is the ion mass, ϕ is the sheath potential drop where $e\phi \gg k_B T_e$ and d is the sheath size. Physically, the gridlet current density cannot exceed this space-charge limited threshold value.

Ion beams have become the more popular ion source in sputtering experiments due to their well-defined beam properties. Since the ions are decoupled from the plasma source by the electrostatic grid elements, the multiply-charged ions can be filtered to leave a singly-charged ion beam which can impact a target at oblique incidence. By allowing for obliquely incident ions, the sputtering dependence on the angle of incidence can be assessed. Additionally, the focusing elements also allow the ion beam to have a narrow spot size on the target, enabling the point source sputtering approximation and allowing the angular sputtering profile to be measured. The plasma redeposition effect is also negligible in an ion beam experiment since the plasma source is self-contained.

Even though ion beams have addressed several issues associated with plasma discharge sputtering, there are still downsides to this method. Since the ion beam is not charge-neutral, there are space charge effects that cause the beam to expand radially with increasing distance to the target. The ion beam will either be limited in current density as described by Equation 3.2 or in spot size. There are recent improvements in circumventing the inherent space charge limitations[57], but in general, the currents supplied by ion beams will be much lower than that of a plasma discharge ion source. In the sputtering experiments performed by Yalin[58], the ion beam was created in a discharge chamber with a tungsten filament cathode and extracted by a two-grid ion optics system, yielding an average current density of 0.1 mA cm^{-2}. This value is an order of magnitude lower than that predicted by the Bohm current calculation for a plasma discharge. The ion beam was also not filtered for multiply-charged ions and the current uncertainty associated with SEE is still present. There is also the possibility of charge-exchange collisions (CEX) creating energetic neutrals that aren't measured from the ion current to the target, resulting in an overestimation of the ion-induced sputtering yield. Therefore, it can be seen that while ion beams are beneficial for many cases, plasma discharge ion sources can still be advantageous for testing certain samples.

3.2 Sputtering Yield Measurement Techniques

There are a variety of *in situ* and *ex situ* methods for measuring the sputtering yield in the low energy (<1000 eV) regime. Comprehensive reviews of these techniques can be found by Nakles[59] and Duchemin[44] so only a brief discussion will be provided here. The available techniques are categorized into mass loss, thickness change, sputterant collection, and spectroscopic methods below.

3.2.1 Mass Loss

The measurement of sputtering yield by mass loss is typically accomplished by either bulk weight loss measurements using a balance or thin film mass loss using a quartz crystal microbalance. Weight loss methods have been used since the early days of sputtering experiments, particularly with plasma discharge ion sources due to the larger mass losses associated with their higher current densities[24, 60]. Meanwhile, the quartz crystal microbalance is a diagnostic that has emerged in the past few decades enabling sensitive mass loss measurements from thin films. Both of these methods involve combining the measured mass loss with the corresponding ion fluence to calculate the time-averaged sputtering yield.

3.2.1.1 Weight Loss

The weight loss method is often used in the sputtering community due to its relative simplicity. The mass of a sample is recorded before and after ion irradiation using an analytical balance or microbalance with a sensitivity ranging from 1 μg to 0.1 mg. The corresponding ion fluence is obtained by monitoring the ion current from a shunt resistor connected directly to a target. These two quantities provide sufficient information for calculating the sputtering yield of the target material at a given ion energy.

Some of the complications of the weight loss technique include contamination, ion implantation, and for plasma discharges, obliquely incident ions and plasma redeposition. The presence of contaminants, such as sputterants from other interfaces in the chamber, can be inspected visually using a Scanning Electron Microscope (SEM) and spectroscopically using Energy Dispersive Spectroscopy (EDS). Ion implantation can also be assessed using the EDS, which provides the surface composition down to a skin-depth of a few μm. In a plasma discharge, the high current densities allow the surface to be "cleaned" via sputtering so contaminants can also be removed in real-time. However, oxide layers can still form when removing the sample from the vacuum chamber, which is difficult to avoid.

For plasma discharges, the ions are assumed to be normally incident on the target, but this is not necessarily true at the edges of the target where fringe fields exist. Sheridan[55] also notes that the ion dose is higher at the corners of the sample. This effect is often negligible for samples with larger surface areas. A more substantial concern is the error associated with plasma redeposition of the target material. When a sputtered atom is ejected from the surface, it has a probability of becoming ionized in the background plasma and being accelerated by the pre-sheath or sheath electric fields back to the sample. In this case, the measured sputtering yield is underestimated since some of the sputtered particles were effectively not accounted for in the mass loss. An analytical calculation to approximate this effect is described in the Appendix.

3.2.1.2 Quartz Crystal Microbalance Mass Loss

The Quartz Crystal Microbalance (QCM) utilizes the frequency sensitivity of an electromechanically oscillating quartz crystal to measure the absolute mass loss of a thin film deposited on the crystal. By placing the sensor in a vacuum vessel, the mass loss during the sputtering process can be measured in real time. McKeown[61] was an early demonstrator of this technique while Duchemin[62] and Kolasinski[63] applied this method to low energy sputtering experiments for electric propulsion applications.

The operation of a quartz crystal microbalance is based on Sauerbrey's equation[64]:

$$\frac{\Delta\sigma}{\sigma_0} = -\frac{\Delta f}{f_0}, \tag{3.3}$$

where σ_0 is the initial areal mass density and f_0 is the initial resonant frequency of the crystal. The thin film of the sample material is first uniformly deposited on the quartz crystal oscillator, increasing the areal mass and lowering the overall resonant frequency. As the thin film is sputtered away, the areal mass decreases and the resonant frequency increases. The mass loss can be tracked as the frequency changes and when combined with the ion current measured directly from the sample, the sputtering yield can be obtained as in the weight loss method.

In contrast to the weight loss method, the QCM mass loss technique is performed *in situ*, avoiding the necessity of venting the chamber to atmosphere, and provides mass sensitivity on the order of 1 ng. The primary limitation is the requirement that the material be deposited on the quartz crystal as a thin film. The sputtering behavior of a thin film may differ from that of the bulk material due to crystal orientation or surface topography[59]. Therefore, extrapolation to bulk materials is not always possible so application of the results must be done carefully. Additionally, the QCM mass loss method is prone to the limitations of the QCM system itself, such as thermal drifts[65], asymmetric thin film coatings, and non-uniform sputtering. If care is taken to mitigate all of these issues, the QCM mass loss technique can provide a powerful method of measuring very small sputtering yields.

3.2.2 Thickness Change

Assuming a constant area, the mass loss of a sputtered sample can be deduced from its thickness change. Two of the most popular methods that utilize this idea include the intensity attenuation through a thin film and profilometry. The first method involves shining a light source of known intensity through the film and measuring the attenuation. Given that the film isn't optically thick, the thickness can be obtained. Another technique is the use of profilometry with a masked control region for measuring the relative sputter depth. Profilometry has been used by Blandino[66] to find the sputtering yields for several EP materials with xenon ion impingement.

3.2.2.1 Profilometry

In the profilometry method used by Blandino[66], the outer annulus of the target is masked and the volume of the sputtered crater is measured using a microstylus. The sputtered volume is converted to the mass loss by means of the bulk density of the material. Combined with the ion flux, the sputtering yield can be obtained.

The benefit of this technique is the capability to map the entire eroded region to determine overall mass loss. It can also serve as a secondary method for comparing to the simple weight loss technique. The primary considerations are the surface roughness, azimuthal non-uniformities, and additional thickness change effects[59]. The surface must be polished such that the sputter depth is orders of magnitude larger than the roughness length. Therefore, this technique will not work with structured materials that have large surface features. Since 1D chords are measured using the profilometer, any non-uniformities in the azimuthal direction will distort the mass loss measurement. To overcome this issue, a higher density of scans must be taken, but this can be time intensive. Additionally, there are other mechanisms that can result in thickness changes such as irradiation damage or thermal effects. In general, profilometry appears to be a useful technique for well-controlled samples with flat surfaces, but will not be used for the structured material testing in the present work.

3.2.3 Sputterant Collection

The sputtered particles from the sample can be collected on adhering surfaces and analyzed to determine the total amount of sputtered mass. The total collected sputterant mass should equal the mass loss measured directly from the sample. Two popular methods of collecting and analyzing sputtered particles are the Rutherford backscattering and Quartz Crystal Microbalance (QCM) methods which are described in the following sections. Other methods include radioactive tracers[67], collection plates[68], mass spectrometry[69], and cavity ring-down spectroscopy[70], but are not discussed here.

3.2.3.1 Rutherford Backscattering

The Rutherford backscattering (RBS) technique allows the user to analyze a thin film of the sputterant material using a high-energy ion beam and the resulting backscattered ions. By

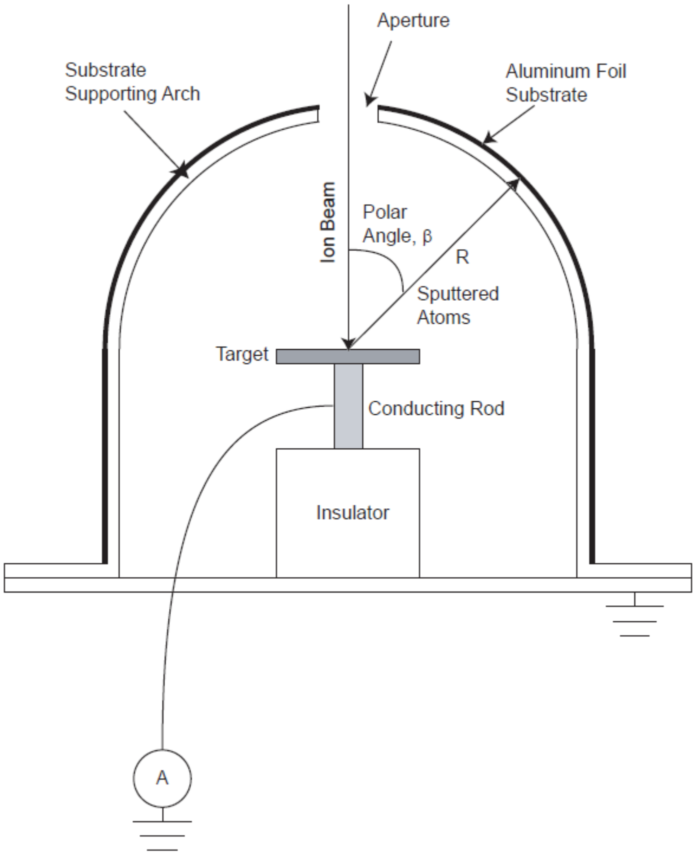

Figure 3.1: Schematic of a Rutherford backscattering sputtering experiment. Source: M. Nakles (2004)

analyzing the behavior of the backscattered ions, information on the thin film depth, areal concentration, and crystal structure can be obtained. Nakles[59] applied this technique to measuring the sputtering yield of molybdenum films by xenon ions using the experimental setup shown in Figure 3.1. The sputterants are collected on thin film aluminum substrates and subsequently analyzed at an RBS facility.

RBS analysis is based on the well-understood theory of binary collisions. A high-energy ion that penetrates the solid surface can collide elastically with a neutral atom and backscatter to a solid state detector. The backscattered ion will have an energy equal to a fraction of its incident energy based on collision properties such as the impact parameter, ratio of masses, and stopping power. By calculating the differential Rutherford backscattering cross section, the relative number of sputtered atoms on the foil substrates can be related to the thin film thickness. Combined with the incident ion flux, the differential sputtering yield of the target material can be obtained. For more details on RBS analysis, see the dissertation by Nakles[59].

The RBS technique is useful for its high sensitivity to sputtered films, allowing for low energy sputtering measurements to be made. However, as Nakles notes, the RBS technique is susceptible to non-ideal experimental conditions such as doubly charged ions, high background pressures, non-unity sticking coefficients of the substrate, and surface topography. Given careful consideration, an RBS experiment that addresses these concerns can be valid method of measuring low energy sputtering yields.

3.2.3.2 Quartz Crystal Microbalance Collection

The QCM collection technique, in contrast to the QCM mass loss method, involves mounting the sensor to a rotary stage to measure the differential sputtering rate at varying polar angles from the target. Similar to the RBS technique, the QCM collection method can provide angular sputtering profiles for beam ions of varying incidence angles. Yalin et al.[58, 71] performed experiments to obtain the angular sputtering profiles and total sputtering

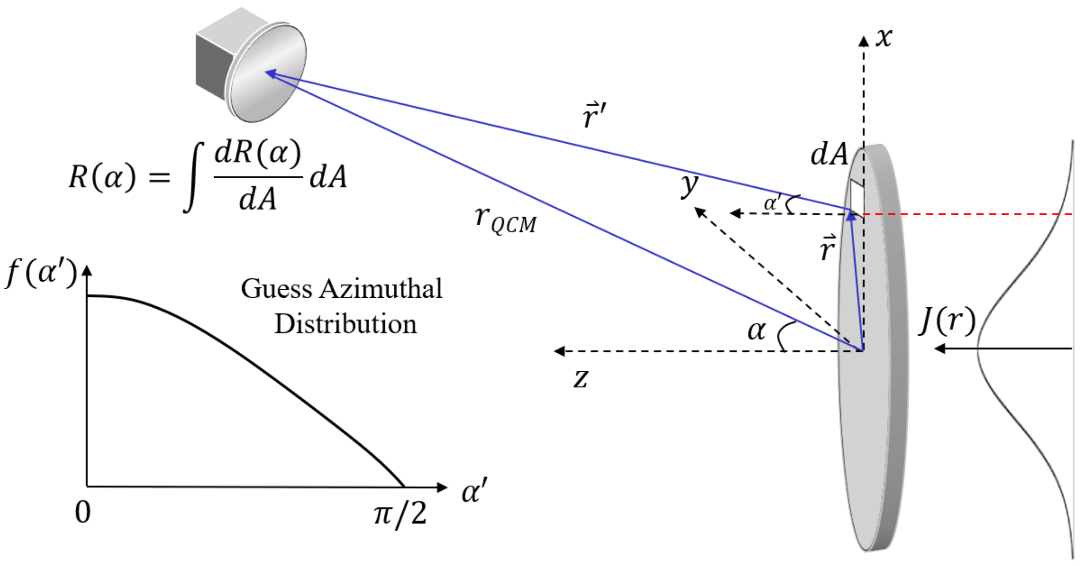

Figure 3.2: An illustration of a QCM experimental setup with a "finite" target.

yields with varying incidence angles for EP-relevant ion-material combinations. As an *in situ* diagnostic, the QCM can measure the angular sputtering profile in real-time, allowing for time-resolved sputtering yield measurements only limited by the scan duration. This capability is particularly useful for structured surfaces which have a transient sputtering yield curve.

The same principles for the QCM that are described in Section 3.2.1.2 apply here. The main difference is that instead of measuring the mass loss from a thin film deposited on the sensor, the sensor is now measuring the incident sputterant flux from the target. The detected sputtering rate depends on the sticking coefficient of the crystal coating, which is typically a gold or silver alloy. Bachmann and Shinn[50] found that the sticking coefficient of gold and silver on a SiO substrate was near unity for film thicknesses above 10 Å, and 10-20% less for thinner films. Therefore, it is imperative to allow a 10 Å thickness film to develop prior to performing the sputtering measurements.

Some of the key considerations in using a QCM to obtain the differential sputtering yield are the beam profile of the incident ions and the validity of the point-source approximation. In essence, these two scenarios are coupled since a beam profile would converge to a delta-function for a point source target. For a "finite" target where the target diameter is comparable to the QCM distance, the incident ions may have a radially dependent beam profile such as a Gaussian. As shown in Figure 3.2, the beam profile, $J(r)$, results in a different ion flux at different radial locations on the target. Even more complicated is the consideration of a finite-sized target for obtaining the angular sputtering profile. In most experiments[58], the sputtering area is assumed to be small enough to be considered a point source such that the measured angular profile is that of a true sputtering point source. However, if target is considered finite, the differential sputtering areas across the target will need to be considered as illustrated in Figure 3.2. Each differential area, dA, has a local sputtering profile, $f(\alpha')$, which is the unknown true angular sputtering profile. Unfortunately, the quantity that is measured by the QCM is $R(\alpha)$ which is the integral of the sputtering contributions from across the target, emitted at an angle $\alpha' \neq \alpha$. Sometimes, empirical formulas or theoretical results can provided a starting point for $f(\alpha')$ but this information is not always available. In the limit that the target becomes a point source ($R_{\text{target}} \ll r_{\text{QCM}}$), $\alpha \to \alpha'$ and the measured angular distribution becomes the true profile. This analysis is performed for the experiments in Chapter 4 to assess the error of assuming a point source for the target. When taking all of these considerations into account, the QCM collection method provides a powerful way to measure the time-resolved angular sputtering profile and total sputtering yield for materials with evolving surface morphologies.

3.2.4 Spectroscopy

Spectroscopic methods of measuring the sputtering yield typically have the highest sensitivity of the diagnostics discussed here. They are also non-intrusive, allowing for minimal disturbance measurements of low energy sputtering experiments. Several different techniques have been applied to sputtering measurements including Rutherford backscattering spectrometry[59], secondary neutral mass spectrometry[72], Auger electron spectroscopy[73], laser induced fluoresence spectroscopy[74, 75, 76], and optical emission spectroscopy[77, 78, 79, 80], among many others not mentioned here. Below, the optical emission spectroscopy technique is briefly discussed.

3.2.4.1 Optical Emission Spectroscopy

The optical emission spectroscopy (OES) method is the simplest in terms of experimental implementation and least perturbing to the plasma due to its passive nature. The only requirements are a spectrometer with gratings designed for the visible regime (300 - 900 nm), a sensitive detector (e.g. charge-coupled device (CCD) or photomultiplier tube (PMT)), collection optics, and a fiber-optic or mirror system. Since the OES technique does not involve laser-based stimulation or *in situ* detectors, the emission of the plasma can be observed passively leading to the purest measurement possible. However, the benefits of the passive and simple data collection are balanced by the difficulties of interpreting the spectroscopic data and the fact that most methods only provide relative sputtering yield measurements, being calibrated against absolute methods such as the weight loss method.

One of the earliest OES sputtering experiments was conducted by Stuart and Wehner[81]. They monitored a strong emission line for the target material and plotted the line intensity as a function of incident ion energy, showing that the intensity demonstrated the same trends as that of absolutely obtained weight loss measurements. Therefore, the relative spectroscopic data was calibrated with the weight loss data. It was therefore assumed that the sputtering yield was linearly proportional to the sputterant emission line intensity, and collisional-radiative effects were not taken into account. More advanced analysis techniques will incorporate collisional-radiative models to better relate the line intensity to excited state population densities, therefore achieving more accurate measurements of the sputterant density. Doerner et al.[77] performed similar experiments with absolute weight loss calibration and single line emission analysis, but included the effect of an ionization/photons ratio (S/XB) to account for both excitation and ionization. Rock et al.[78] discuss a more detailed kinetic steady-state (KSS) approach to collision-radiative modeling for molybdenum sputtering by mercury ions in ion thrusters. His conclusion was that the OES technique is an effective tool for making rapid and sensitive measurements given availability of collisional-radiative cross-sections for the sputtered materials.

Many other experiments report the same findings of high sensitivity measurements for low energy sputtering and lack of experimental cross-sectional data for constructing accurate collisional-radiative models. However, even with its limitations, OES may present an attractive alternative to direct methods for measuring the time-resolved sputtering yield of structured materials.

3.3 Summary

While there exists a basic structure for sputtering experiments, there is no consensus on the best sputtering yield measurement technique to be used. The benefits and detractions of the most popular techniques were discussed and it can be seen that certain methods are more suitable for *in situ* time-resolved sputtering yield measurements for advanced structured materials. In particular, the weight loss and QCM collection methods will be utilized for the present work as discussed in detail in the following section.

CHAPTER 4

Experimental Setup

The sputtering experiments presented in this work were conducted in the Plasma interactions (Pi) test facility at the UCLA Plasma and Space Propulsion Lab. As discussed in the previous chapter, many considerations are necessary in designing a sputtering experiment with the proper diagnostics for measuring the sputtering yield. In particular, since the ultimate objective is to measure the time-resolved angular sputtering profile and total sputtering yield of structured materials, the quartz crystal microbalance collection method has been implemented. In this chapter, the Pi facility, diagnostics suite, QCM sputtering yield analysis, and material samples are discussed.

4.1 Plasma Interactions Test Facility

The Pi facility consists of a 1.8 m diameter by 2.8 m long cylindrical aluminum vacuum chamber and two cryopumps with a combined pumping speed of 5000 L/s on argon. The base pressure is 5×10^{-7} Torr and the typical working pressure (at 27 sccm argon flow) is $(6.0 \pm 0.5) \times 10^{-5}$ Torr. The overall configuration of the Pi source is shown in Figure 4.3. For this study, the Pi facility's DC discharge uses a 250 A lanthanum hexaboride (LaB_6) hollow cathode, located at the far upstream end of the plasma column. The cathode orifice is located at the downstream face of the cathode magnets and is directed into a 5-cm diameter, 30-cm long, cylindrical anode held at ground potential to supply a partially ionized argon or xenon plasma. The gas injection is divided between the hollow cathode and an external anode injector just downstream of the cathode keeper face. The use of an auxiliary anode injector

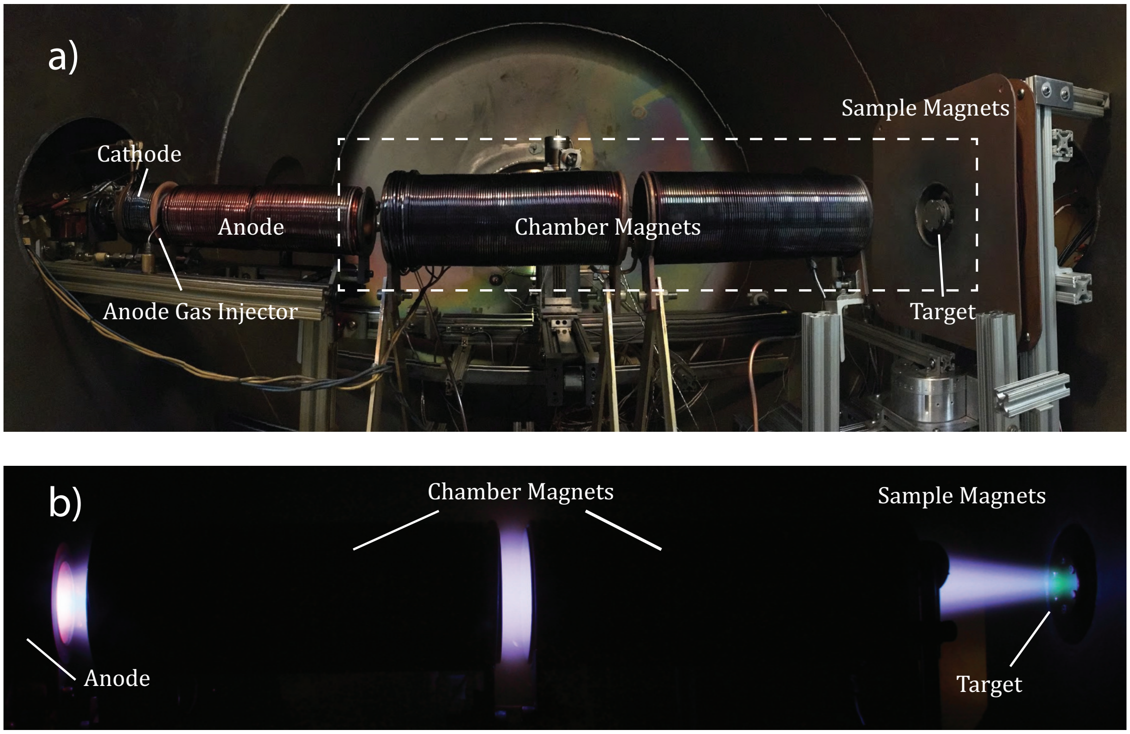

Figure 4.1: The images above show a) the Pi facility experimental set-up and b) the dashed region with the plasma on.

has been shown to reduce cathode plume oscillations and also minimize the production of energetic ions [82, 83]. The plasma discharge is controlled by commanding the gas flow and discharge current. The Pi facility operating conditions have been characterized in detail by Matlock et al. [84, 85].

The plasma is confined by electromagnetic solenoids surrounding both the cathode and anode, and transported downstream via the water-cooled chamber magnets, also held at ground potential. This design isolates the cathode from the target region to prevent sputtered particles from the cathode from depositing on the target (and vice versa)[84]. At the downstream end of the chamber, the sample magnets pinch down the plasma to provide focused impingement on a biased target to avoid interaction with other facility surfaces. Figure 4.2 shows a magnetic field simulation of the near-target region using ANSYS Maxwell, indicating a lensing effect at the location of the target. This operating mode localizes the

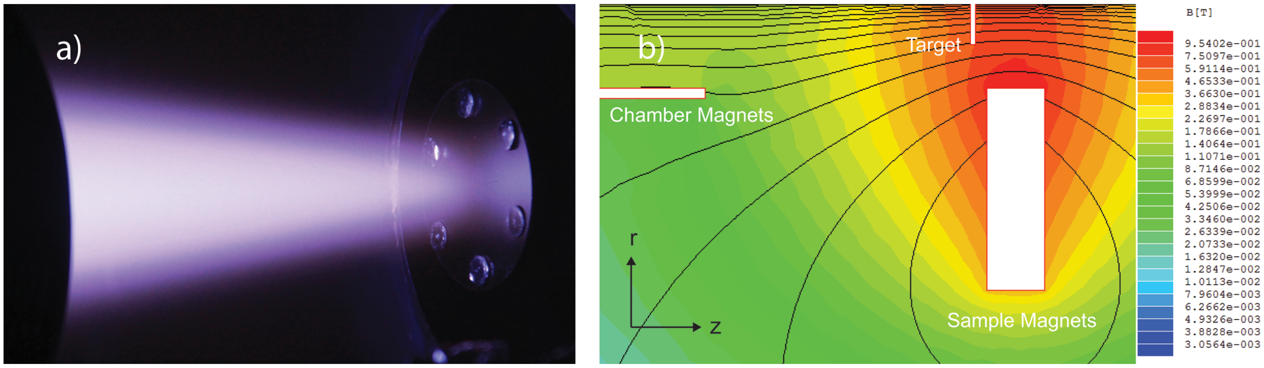

Figure 4.2: The images above show a) the near-target plasma and b) the magnetic field simulation of the near-target region.

erosion region on the target with a beam spot size of around 1.5 cm. A small spot size was chosen to facilitate the interpretation of sputtering from a point source rather than analyze sputtering across the entire target. This simplication makes interpretation of quartz crystal microbalance data significantly easier, and allows an accurate angular distribution to be extracted.

The plasma ions are typically formed within an electron temperature (<10 eV) of ground potential, providing a stable reference for biasing the target negative to control the incident ion energy. The target floats at around -40 V with respect to the chamber magnets, which are maintained at facility ground. To provide a range of incident ion energies, the target can be biased independently, as low as -300 V with the present power supply. This configuration allows normally incident ion impingement upon various conducting samples and for the sputtering rates to be diagnosed within the easily accessible target region.

4.2 Diagnostics

A variety of diagnostics were used to obtain the properties of the near-target plasma and material samples in addition to the sputtering yield diagnostics in order to ensure a well-controlled sputtering experiment. A subset of the diagnostics suite implemented for this

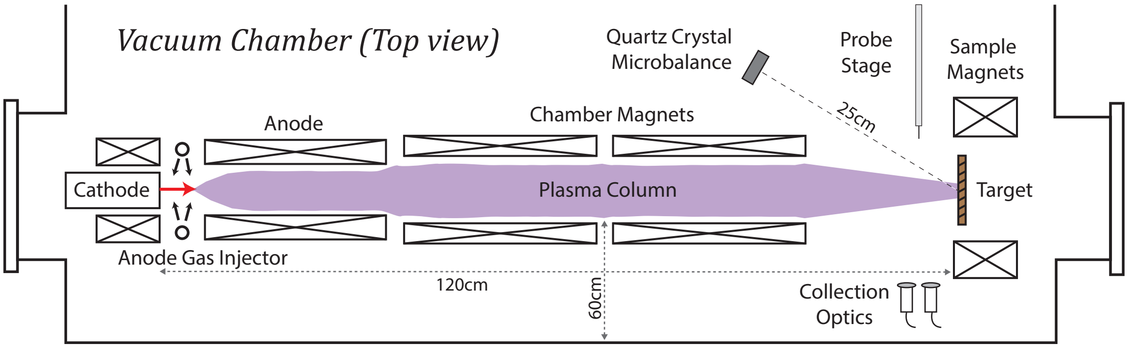

Figure 4.3: Schematic of the front end of the Pi facility vacuum chamber.

study is shown in Figure 4.3, with a comprehensive list of the Pi facility's capabilities presented in Table 4.1.

The Langmuir probe consists of a cylindrical tungsten wire encapsulated by an alumina probe holder. The electron temperature is calculated from the slope of the I-V curve in the transition region (a Maxwellian electron population is assumed), while the plasma density is extracted from the ion saturation region. Based on previous measurements[84], the probe ratio (r_p/λ_D), where r_p and λ_D are the probe radius and Debye shielding length, respectively, indicates that Orbital Motion Limited (OML) and thin-sheath approximations are not valid in our plasma. Instead, a numerical approach by Steinbruchel[86], based on the theory by Laframboise, is needed. This technique provides a measurement of the electron temperature and plasma density by accounting for varying sheath effects.

Table 4.1: Pi facility diagnostics suite

Diagnostic	Measured parameters
Langmuir probe	n_e, T_e
Faraday probe	1-sided ion flux
Emissive probe	plasma potential
Retarding Potential Analyzer	ion energy distribution
Quartz Crystal Microbalance	differential sputtering rate
Emission Spectroscopy	line emission
Residual Gas Analyzer	partial gas pressures
Ionization Gauge	neutral pressure
Long Distance Microscope	in situ surface visualization
Energy Dispersive Spectroscopy	surface composition

The Faraday probe is a planar Langmuir probe with a concentric guard ring used to produce a uniform sheath across the probe face. The circular collection electrode has an area of 0.14 cm^2 and is insulated on the backside with high temperature ceramic cement. Both the guard ring and collector are biased to -100 V to collect ion saturation current, which is related to plasma density, n_e, by $I_{\text{sat}} \approx 0.6 n_e e A_p \sqrt{8kT_e/\pi m}$. Consequently, the 1-sided ion flux can be defined as $\Gamma_i = I_{\text{sat}}/(eA_p)$.

The Retarding Potential Analyzer (RPA) is constructed out of four electrically isolated molybdenum meshes (0.001" diameter, 100 wires/in) with a tungsten collection electrode at the end. The ordering of the grids is as follows: floating attenuation, electron repelling, ion retarding, and secondary electron suppression. The floating attenuation grid minimizes perturbations and reduces the plasma density entering the device. The electron repelling grid is biased to -100 V to repel electrons and only allow ions through. The ion retarding grid is scanned from a typical voltage range of -60 V to +20 V with the upper limit determined by where the ion current disappears. The secondary electron suppression grid is biased at -9 V relative to the collector, which is at -100 V, to reflect secondary electrons from the other grids. In order to measure the spread of ion energies hitting the sample, the RPA is positioned at the location of the target in Figure 4.3.

The spectroscopy set-up consists of two *in vacuo* shadow-shielded collimating lenses leading to an FHR1000 1.0 m focal length monochromator through a multi-fiber optic bundle. The output light from the FHR1000 is projected onto a 2048 x 512 pixel Synapse Charge-Coupled Device (CCD) camera. A 2400 grooves/mm grating is installed to scan the wavelength range from 300 nm to 600 nm, where the majority of neutral molybdenum and ionized argon lines appear. The spectrometer is absolutely calibrated using the 404.656 nm line in an ArHg lamp, with the wavelength error increasing to 0.1 nm at the edges of the spectral range.

The Quartz Crystal Microbalance (QCM) provides in situ measurements of the angular distribution of sputtered particles, which can be integrated to obtain the total sputtering

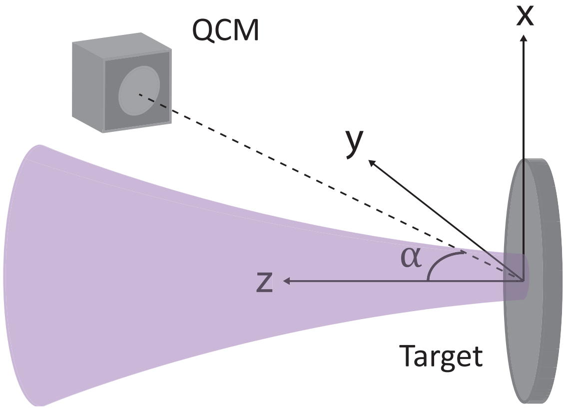

Figure 4.4: Definition of the QCM coordinate system relative to the target. The polar angle is defined relative to the z-axis.

yield. As particles are adsorbed onto the crystal sensor, the resonance frequency decreases linearly in proportion to the deposited mass[64]. The piezoelectric sensitivity of quartz crystals to added mass allows deposition rates as low as 0.4 ng cm^{-2} s^{-1} to be measured.

An INFICON front load single sensor containing a silver-coated AT-cut quartz crystal is employed in the chamber. The crystals have a resonance frequency of 6 MHz and an exposed area of 0.55 cm^2, and are assumed to have a sticking coefficient of order unity for condensable metals[50]. Data is logged using the STM-2 deposition monitor, which also possesses an external oscillator for precise frequency measurements and the IC6 deposition controller for later experiments, which has an order of magnitude higher resolution than the STM-2. To ensure thermal stability, the crystal holder is water-cooled and protected by a pneumatically actuated shutter.

The QCM crystal holder is mounted to a rotary stage with a moment arm of length 25.4 ± 0.2 cm to provide measurements at varying polar angles, α, in the lateral plane. The coordinate system used for the QCM measurements is defined in Figure 4.4. For normally incident ions, the angular distribution of sputtered particles is assumed to be azimuthally symmetric so the differential sputtering rate, $R(\alpha)$ [ng cm^{-2} s^{-1}], is a function of α only.

To obtain polar measurements, the QCM is rotated in 5° increments from $\alpha = 90°$ to

30°, beyond which the QCM becomes blocked by the chamber magnets. Due to vibrations in between measurements, data is recored for 1 minute at each location and the first and last 5 seconds of data are neglected. The differential sputtering rate, $R(\alpha)$, is obtained by performing an arithmetic average of the data over the 50 seconds of measurement.

The remaining diagnostics are described briefly to provide auxiliary information for this work. Emissive probes were used to measure plasma potential fluctuations representative of an azimuthal ion instability[87]. A spectroscopy system, consisting of collection optics leading to an FHR1000 spectrometer through an optical fiber, has been implemented for optical emission spectroscopy to study plasma species and eventually to be developed into a supplementary method of sputtering yield measurement. A Residual Gas Analyzer (RGA) was used to ensure that there were no water leakages or major contaminants prior to testing. The ionization gauge is used to monitor the neutral gas pressure at the rear-end of the chamber. A long distance microscope is being implemented for *in situ* visualization of surface evolution during sputtering. A Scanning Electron Microscope (SEM) was used in conjunction with Energy Dispersive Spectroscopy (EDS) to analyze surface morphology and inspect for contaminants before and after plasma exposure.

4.3 Sputtering Yield Data Analysis

The sputtering yield measurement techniques utilized in this work are the weight loss and QCM collection methods. The details of the implementation of these two methods are described below.

4.3.1 Weight Loss Method

The measurement of sputtering yield by weight loss is used here because of its relative simplicity. The masses of the samples are recorded before and after plasma irradiation, and the ion current is monitored during testing from a 10 Ω resistor connected directly to the target. A cylindrical Kapton shield with 70 μm thickness is wrapped around the target to prevent excess current collection from the sample mount assembly. The mass loss and target current data provide sufficient information for calculating the sputtering yield of the target material at a given ion energy. For a pure-element sample with negligible impurity concentration, the total number of particles sputtered can be calculated as follows:

$$N_s = \left(\frac{|\Delta M|}{m}\right) N_A, \tag{4.1}$$

where N_s is the total number of sputtered atoms, ΔM is the mass loss in grams, m is the atomic weight of the target material in amu, and N_A is Avogadro's constant equal to 6.02×10^{23} atoms/mol. For materials with multiple constituents, the atomic weight, m, can be replaced with an effective mass m_{eff}. The total ion fluence over the burn is calculated by integrating the target current from onset to removal of the target bias:

$$N_i = \frac{1}{e}\int_{t_0}^{t_1} J_t(t)dt, \tag{4.2}$$

where N_i is the total ion fluence, e is the elementary charge (1.6×10^{-19} C), t_0 and t_1 are the sputtering initiation and removal times respectively, and $J_t(t)$ (A) is the time-varying target current. The ratio of these two terms gives the total sputtering yield in atoms per ion:

$$\overline{Y} = \frac{N_s}{N_i}. \tag{4.3}$$

The quantity $\overline{Y}$ is the total sputtering yield averaged over the entire plasma exposure. A time-resolved sputtering yield would be difficult to obtain because the bias time would need to be sufficiently short and the sample would need to be removed from vacuum to be weighed. Additionally, the weight loss method assumes that plasma redeposition is negligible. Appendix B uses a geometric analysis to show that plasma redeposition in the Pi plasma contributes less than 10% to the measured sputtering yield.

4.3.2 Quartz Crystal Microbalance Analysis

The *in situ* QCM method enables time-resolved measurements of the angular distribution of sputtered particles and total sputtering yield. Following the methodology of Yalin[58], the differential sputtering yield, $dy/d\Omega$, can be calculated in terms of the differential sputtering rate, $R(\alpha)$, as follows:

$$\frac{dy(\alpha)}{d\Omega} = \frac{eR(\alpha)N_A r_{\text{qcm}}^2}{mJ_t} \tag{4.4}$$

where A_s is the QCM sensor area (0.55 cm^2), m (amu) is the atomic weight of sputtered particles, N_A (6.02×10^{23} atoms mol^{-1}) is Avogadro's constant, J_t (C/s) is the target current, and r_{qcm} (25.4 ± 0.2 cm) is the distance from the QCM to the target center. To calculate the total sputtering yield, the differential sputtering yield is integrated over all solid angles in the hemisphere in front of the target:

$$Y = \int_0^{2\pi} \int_0^{\pi/2} \frac{dy(\alpha)}{d\Omega} \sin(\alpha)\, \mathrm{d}\alpha\, \mathrm{d}\phi \tag{4.5}$$

For a true steady-state experiment, this calculation would provide the same sputtering yield regardless of when the QCM scan was performed. However, this is not the case for an experiment with a changing sputtering yield. A micro-architectured material will have a transient erosion profile which is a function of the surface features at the erosion site, changing both the overall sputtering yield and angular sputtering distribution. To capture this time-dependent sputtering behavior, the QCM scans must be performed on a time-scale much smaller than the transient erosion time-scale.

The time-dependent sputtering yield equation can be obtained by combining Equation

4.4 and 4.5 as follows:

$$Y(t) = \left(\frac{eN_A}{m}\right) 2\pi r_{qcm}^2 \int_0^{\pi/2} \frac{R[\alpha(t)]}{J_t[\alpha(t)]} \sin[\alpha(t)]\,\mathrm{d}\alpha. \tag{4.6}$$

In this equation, the time-dependence is captured in the dependent variable $\alpha(t)$ which represents the QCM angular location. Since the QCM records data over a finite period of time, the sputter rate $R[\alpha(t)]$ and target current $J_t[\alpha(t)]$ are temporally averaged. The sputter rate will change depending on the angle of collection, the present surface morphology, and the average target current during measurement. Plasma density variations near the sample will result in a changing target current over time. This time-varying current is accounted for in Equation 4.6 by averaging the measurements over a period much shorter than the plasma variations (on order of hours).

In order to perform the integration in Equation 4.6, the differential sputtering yield must be extrapolated to the interior polar angles where data cannot be obtained. This can be done by fitting the data to a physical sputtering profile if one is available. The sputtering profile for normally incident ions on a flat surface is known to have a cosine shape for high energies ($>$ 1 keV). However, for low energy sputtering ($<$ 1 keV), the angular profile tends be more diffuse with a relative maximum near 45°. The sputtering profile derived by Zhang and Zhang[49] and modified by Yalin[58] is used to provide an accurate fit for QCM data. Tthe following expression is termed the Modified-Zhang (MZ) equation and is applicable for normally incident, low energy sputtering of planar samples:

$$\frac{dy_{\mathrm{MZ}}}{d\Omega} = \frac{Y}{1-\sqrt{\frac{E^*}{E}}} \frac{\cos(\alpha)}{\pi} \left[1 - \frac{1}{4}\sqrt{\frac{E^*}{E}}\ \gamma(\alpha)\right] \tag{4.7}$$

$$\gamma(\alpha) = \frac{3\,\sin(\alpha)^2 - 1}{\sin(\alpha)^2} \quad + \quad \frac{\cos(\alpha)^2(3\,\sin(\alpha)^2+1)}{2\,\sin(\alpha)^3} \times \ln\left[\frac{1+\sin(\alpha)}{1-\sin(\alpha)}\right], \tag{4.8}$$

where Y is the total sputtering yield, E^* is a characteristic energy, E is the ion energy (eV), and α is the polar angle. The two free-fit parameters, Y and E^*, are determined from least squares fitting to the data while the remaining parameters are determined from the test conditions. The parameter E^* is inherently related to the threshold sputtering energy, but has been found to disagree with experimental results[49]. Therefore, this expression will be used as an empirical fit only and not attempt to interpret the characteristic energy. The other free-fit parameter Y is the total sputtering yield and is the quantity desired for this study.

Equation 4.7 does not hold for micro-architectured materials where ions impact the surface with a range of non-normal incidence angles. Therefore, an alternative method of extrapolation must be used to determine the integrated sputtering yield for these samples. Ideally, the convolved sputtering profile for a material with well-characterized surface features could be modeled using local sputtering distributions for individual collisions. This process would involve a Monte-Carlo simulation integrating 3D surface mapping, an accurate sputtering theory, and the effects of a radial ion flux gradient. For testing of multiple samples with unique surface features, this sophisticated analysis is not feasible.

Instead, the upper and lower bounds for the integrated sputter yield are determined through a simpler method. The upper bound is obtained by assuming the differential sputter yield is constant from $\alpha = 30°$ to $\alpha = 0°$, while the lower bound assumes the yield drops to zero linearly from $\alpha = 30°$ to $\alpha = 0°$. The reported sputter yield is the average of these two values with the differences from the mean included as a standard deviation. The error due to this extrapolation technique is found to be less than 5%.

The error analysis also includes the point source assumption for both the QCM and target and ion current uncertainties. The QCM is well approximated as a point source because the area of the sensor (0.55 cm^2) is much smaller than the area of the hemisphere that the QCM subtends ($2\pi r_{qcm}^2 \approx 4000$ cm^2). The target can also approximated as a point source since the spot size of the plasma beam (1.5 cm diameter) is much smaller than the QCM distance (25.4 cm). By approximating the target as a point source, the measured $R(\alpha)$ can be taken as the true angular distribution of sputtered particles and the radial dependence of ion flux can be ignored. Simulations with a finite target result in an error of less than 5%. The ion current measurement suffers from uncertainties in the collection area and secondary electron emission (SEE). The sample mount is encapsulated by a Kapton shield to prevent excess current collection, but deviations on the order of 5% are still detected. Additionally, the impacts of 100 - 300 eV ions on the molybdenum surface result in secondary electron yields on the order of 0.1 electrons/ion[88, 89]. However, SEE yields depend strongly on surface characteristics such as oxide layers and roughness so the SEE bias correction is omitted in favor of a 10% error in the reported yield.

4.4 Testing Procedure

In this section, the general testing procedure used for the following experiments is described. First, the sample is weighed using an A&D GR300 precision microbalance and the surface is characterized using an SEM and energy dispersive x-ray spectroscopy (EDS). The SEM images are primarily used to document how the surface morphology changes after plasma exposure, and is also used to inspect for surface contamination. The EDS spectra indicate the level of oxidation before and after testing. The sample is then inserted into the sample mount and the chamber is pumped down to base pressure ($< 5 \times 10^{-6}$ Torr). A residual gas analyzer is used to measure the partial pressures of background gases and ensure a sufficiently low presence of unwanted gases such as water vapor. To begin the test, the hollow cathode is ignited, and the discharge and chamber magnet settings are adjusted to deliver a previously characterized plasma of known ion flux to the target, which floats to approximately -40 V where sputtering is below the detection threshold of our diagnostics. The target is then electrically biased relative to ground potential to bombard the target with plasma ions extracted through the sheath. The ion current to the target is recorded via a shunt resistor for calculating the sputtering yield throughout the test, and can also be used to check for arcing or variations in the near-target plasma conditions. At the end of the test, the target bias is removed and the plasma is turned off. Molybdenum oxidizes at approximately 400°C, so the sample is allowed to cool to 100°C200°C (around one hour after testing) to minimize oxide formation after exposure to atmosphere. In most cases, the sample was allowed to cool for several hours before removal. The chamber is backfilled to atmosphere through a venting port at the rear end of the chamber, and the target is removed and weighed. Post-test analyses are then performed using the SEM and EDS to inspect for contaminants and surface structure evolution.

CHAPTER 5

Surface Sputtering Experiments and Analysis

In this chapter, I present the results of sputtering experiments with flat molybdenum and structured molybdenum samples. The plasma is first characterized to determine the incident conditions of the ions. Afterwards, the flat molybdenum test is conducted as a means of benchmarking the sputtering yield diagnostics on a well-documented ion-target combination. After validation of the diagnostics, a novel structured molybdenum sample is tested to explore the transient sputtering properties of micro-architectured materials. The angular sputtering profiles and total sputtering yields for both samples are presented and the results are discussed.

5.1 Plasma Characterization

For the experiments presented in this dissertation, the operating conditions are set to those shown in Table 5.1 in order to ensure a consistent plasma-sputtering environment. There were fluctuations about the mean values but generally the parameters remained within 10% of the measured values. The mass flow was divided between the cathode (15 sccm) and

Table 5.1: Near-target Plasma Conditions

Parameter	Typical Values
Plasma density	10^{18} m^{-3}
Electron temperature	7 eV
Ion energy to target	40 to 300 eV
Ion flux to target	10^{17} cm^{-2} s^{-1}
Exposure diameter/area	1.5 cm/1.8 cm^2

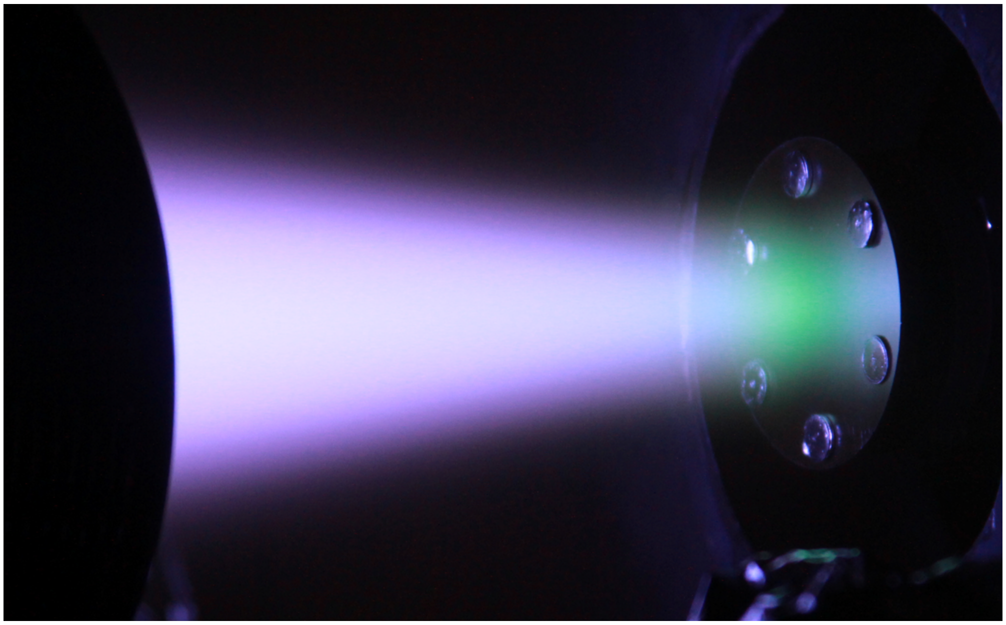

Figure 5.1: The near-target plasma is shown impacting a flat molybdenum sample biased to -300 V. The green glow is due to de-excitation of sputtered molybdenum atoms.

anode (12 sccm) gas injectors to produce a working pressure of 6×10^{-5} Torr on argon and measured using an ion gauge mounted on the chamber wall 4 ft away from the plasma source. The discharge current was fixed to 45 A and the cathode potential floated to an equilibrium value of -40 V relative to the grounded anode. This nominal configuration produced the near-target plasma conditions shown in Table 5.1 which were measured using the diagnostics suite described in Chapter 4.

The near-target plasma must be understood and characterized in detail to provide accurate sputtering yield measurements. As shown in Figure 5.1, the plasma is focused down into a 1.5 cm diameter cusped column in order to provide localized erosion on the center of the test samples. This enables accurate measurement of the angular sputtering profile using the QCM. Martinez-Sanchez[90] found that the ion flux is conserved throughout the axial extent of the cusp. Therefore, I can directly control the delivered ion flux by tuning the discharge parameters.

The 1-D axial ion flux is mapped 5 mm in front of the target using a transverse scanning

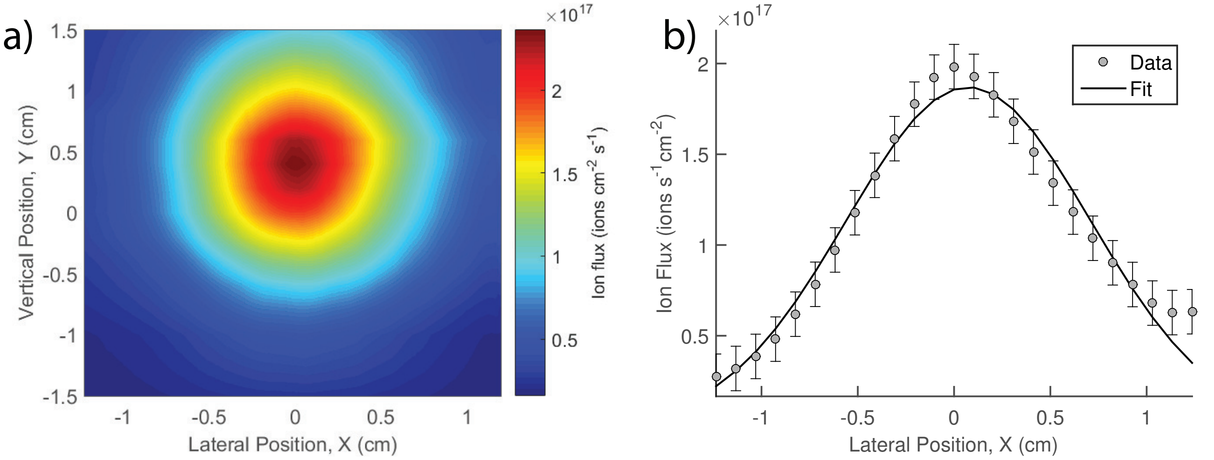

Figure 5.2: The plots above show a) ion flux contours and b) an ion flux profile across the target center-line for the plasma. The plasma is offset by approximately 4 mm in the vertical direction relative to the target.

Faraday probe. These scans are performed before and after target biasing to avoid contamination from sputtering of the probe material. The 2D contour and lateral profile are shown in Figures 5.2a and 5.2b respectively. The plasma at this location is azimuthally symmetric, and is roughly Gaussian with a full-width half-maximum (FWHM) of approximately 1.5 cm, which I define to be the effective exposure diameter of the plasma. The data for $x > 0$ deviate from the Gaussian fit with elevated wings that don't appear to converge to zero flux at infinity. It was discovered post-test that the Langmuir probe holder developed a conducting surface layer of sputtered molybdenum that resulted in extraneous ion collection as the probe holder entered the plasma. Therefore, the left half ($x < 0$) of the Gaussian should be seen as representative of the incident plasma.

An extrapolation of the Gaussian to the radius of the sample (2.5 cm) reveals that there is a non-negligible current at the edges. The effect of this finite edge current on the QCM measurements has been discussed in Chapter 3. One benefit of the radial variation of plasma density across the target region is to allow the characterization of the plasma material interaction behavior (e.g., erosion-deposition) for a range of ion flux and fluence for a single test. This variation in plasma exposure conditions for a single sample is especially

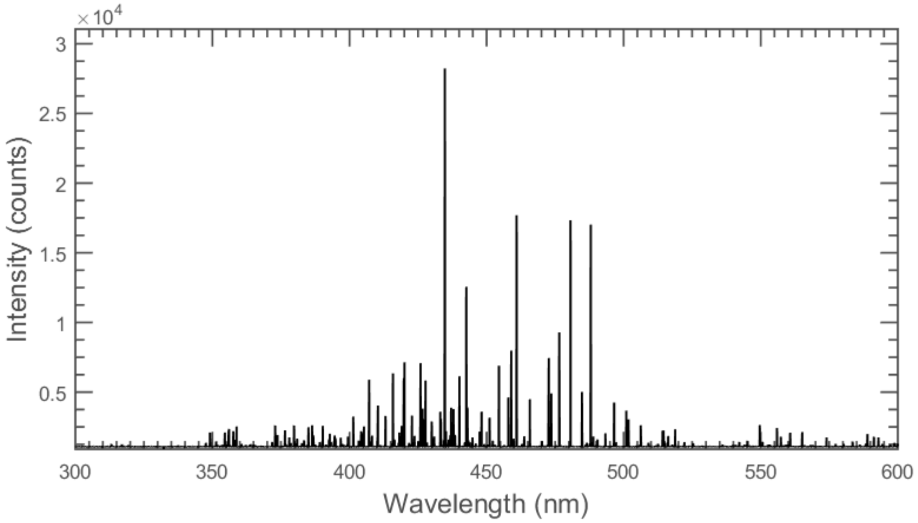

Figure 5.3: Spectrum for 150 eV ions.

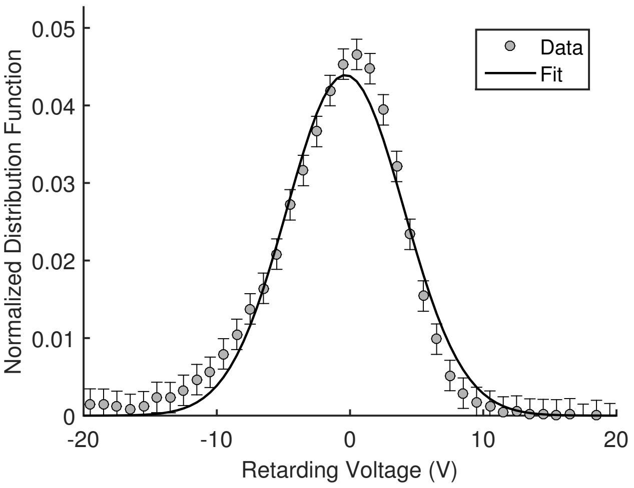

Figure 5.4: The ion energy distribution function is measured at the target using the RPA and fitted to a Gaussian distribution.

informative for analysis of featured and micro-architectured surfaces[91].

Using the spectroscopy system, I record broadband spectra in the 300-900 nm range to guarantee minimal doubly ionized argon in the impinging plasma. Ar^{++} lines with strong intensity levels in low temperature argon plasmas from the NIST database were shown to be lower than the detection threshold of the spectrometer. Representative spectra of the plasma is provided in Ref. [92]. In addition, the axial energy spread of the ions at the target is measured using the RPA described in 4. The normalized ion energy distribution function is shown in Figure 5.4. The distribution is reasonably well approximated by a Gaussian with a standard deviation of 6 V. The retarding potential provides a measure of what plasma potential the ions were created at, implying that the majority of the ions were created near ground potential. Therefore, when the target is biased to a voltage $V_t < 0$, the incident ion energy can be described as $|V_t| \pm 6$ eV.

Deviations in the nominal operating conditions are monitored during each test to accurately characterize the testing environment. The Langmuir and Faraday probes are scanned before and after the target is biased to determine the ion flux profiles and electron temperatures. The ion current time-series is used to monitor changes in the incident ion flux and also allows for time-resolved sputtering yield measurements as described in the following sections.

5.2 Sputtering Experiments

5.2.1 Argon on Flat Molybdenum Test

The Pi facility sputtering yield diagnostics were first benchmarked on an argon ion on flat molybdenum sputtering experiment for ion energies of 100, 150, 200, and 300 eV. The flat molybdenum sample is a 2 in diameter disk that was cut from a rolled finish molybdenum sheet. There are 6 holes for mounting the sample to the sample holder using the assembly shown in Figure 5.5b. Additionally, the caps of the stainless steel screws were milled down and molybdenum disks were spot-welded to the screws. Even though the plasma is localized to the inner 1 in diameter of the disk, molybdenum-capped screws will minimize sputtering from the outer regions. The sample surface was characterized used an SEM with two different magnifications shown in Figure 5.6. The 35x magnification image shows very few distinct features, indicating the surface is flat on the mm scale. At 1180x magnification, there are

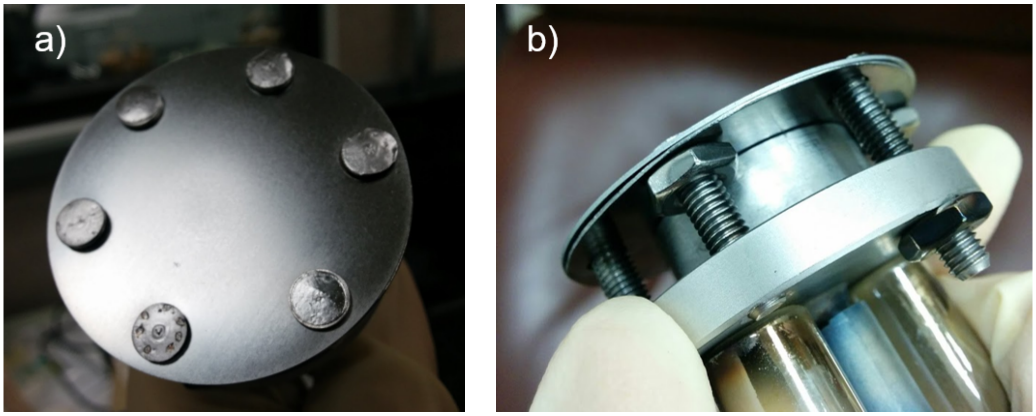

Figure 5.5: The images above show a) the flat molybdenum sample with 6 molybdenum-capped screws and b) the flat molybdenum disk in the sample holder.

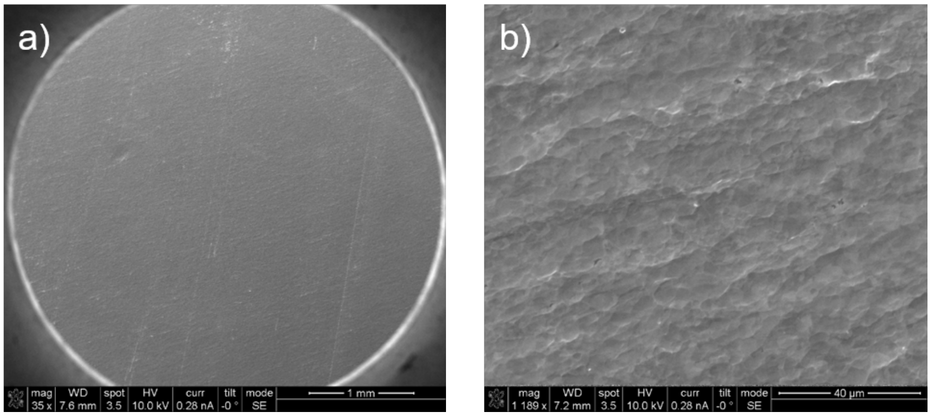

Figure 5.6: The SEM images of the flat molybdenum sample are shown for a) 35x and b) 1180x magnification.

distinct rough features but these do not protrude significantly from the surface. Therefore, the SEM images verify that the flat molybdenum sample is indeed flat to the μm scale. EDS was also performed to assess the purity of the sample and showed that the surface was 100% molybdenum within the error of the device.

The sample was cleaned via low energy ion bombardment, resulting in the sputter-conditioned surfaces shown in Figure 5.6. Prior to testing, the sample was composed of 99.99% molybdenum by weight and contained few surface features larger than 10 μm. The argon plasma was configured into the focused configuration and maintained the near-target plasma conditions given in Table 5.1. The target was exposed to ion bombardment for approximately 1 hour while the ion current was monitored and the QCM was scanned to obtain angular sputtering distributions.

The angular sputtering profiles for the four different test cases are shown in Figure 5.7. Each data set is fit to a Modified-Zhang (MZ) profile using least-squares minimization of the two free parameters, Y and E^*. The MZ fit underestimates the peak values near 50° and drops to zero at a small angle of incidence for 100 eV, but otherwise extrapolates well to the near-normal polar angles. Whether this discrepancy for the peak values is physical or due to experimental error is uncertain. The 100 eV profile drops to zero at 20° which is clearly unphysical. While the MZ-fit is based on low energy sputtering, the theory may be invalid near the sputtering threshold. Zhang uses a value of $E^* = 114$ eV for molybdenum, but he comments that there is disagreement within the literature on the accuracy of this value[49]. For the 100 eV data, the extrapolation to interior angles is redefined as a line from the data point at 30° to the origin at 0° for a more physical representation. These empirical fits allow for integration of the angular distribution to obtain the total sputtering yield.

To determine the temperature dependence of the sputtering yield, QCM scans were obtained at 10 minute intervals for the flat molybdenum test with 300 eV argon ions, as the sample heated from 25°C to approximately 500°C. The variation of the measured sputtering yields were within 5% of the value for 300 eV in Figure 5.8, showing that there was no clear dependence of sputtering yield on temperature within this temperature range.

The total sputtering yields were measured using both the weight loss and QCM techniques as described in Chapter 4. Results for the four different ion energies are shown in Figure 5.8 and compared to previous measurements. When comparing sputtering yields, it is important to note the ion source, the method of measurement, and surface characterization. Weijsenfeld et al. [93] and Laegreid et al. [60] performed weight loss measurements in a low-density plasma discharge with a fully immersed target. Zoerb et al.[94] performed QCM measurements using an ion beam at various incident angles. All experiments did not correct

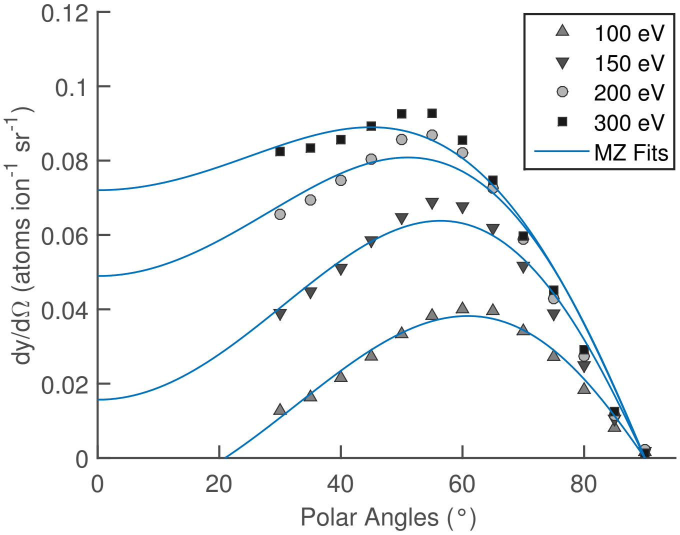

Figure 5.7: Angular distributions for $Ar^+ \rightarrow Mo$ with ion energies of 100 - 300 eV. The uncertainties are not shown here to clearly show the different profiles, but are included in the final error analysis for the sputtering yield.

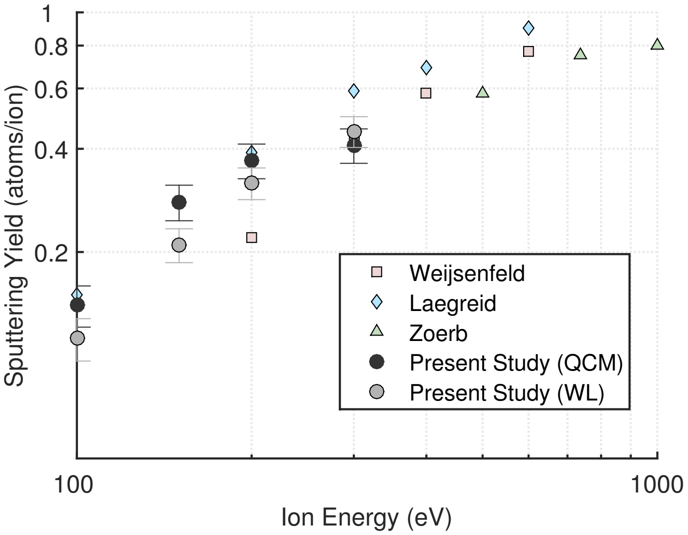

Figure 5.8: The sputtering yields for $Ar^+ \rightarrow Mo$ are compared to results from literature.

for secondary electron emission and did not inspect the surfaces for contamination or surface features. Due to the abundance of experimental factors, a direct quantitative comparison is difficult.

Overall, the sputtering yields from this study fall well within the scatter of published results. The weight loss and quartz crystal microbalance results obtained in this study are consistent within experimental error. However, the trend in the energy dependence for the QCM yield appears to deviate from the others, particularly influenced by the data point at 300 eV. This discrepancy is attributed to the QCM method having more sources of error (see Chapter 3) than the weight loss technique, with several potential problems based on alignment. To truly determine whether the energy dependence measured by the QCM continues on that trend, an additional validation test from 300 eV to 1000 eV would need to be performed. Fortunately, this problem is not critical to the micro-architectured test described in the following section. Since the QCM setup will remain the same throughout the test, the transient sputtering yield should possess generally the same shape, potentially with an offset due to misalignment.

5.2.2 Argon on Structured Molybdenum Test

After the *in situ* diagnostics were benchmarked on a flat molybdenum sample, the time-dependent sputtering yield of the micro-architectured molybdenum sample was measured. This experiment presents the next level of validation as the sputtering yield of a textured molybdenum sample exposed to plasma will eventually converge to the flat sample result when the surface structure has eroded away.

The 2 in diameter micro-structured molybdenum sample was sourced from Ultramet Inc. in collaboration with Professor Nasr Ghoniem and is shown in Figure 5.9a. The fractal geometry shown in Figures 5.9b and 5.9c was created using a Chemical Vapor Deposition (CVD) process that resulted in self-similar bulbous structures on the material surface. Ultramet applies varying CVD conditions to control the scale lengths of the features as well as the depth and feature density. The structures protrude from the surface allowing sputtered atoms to be ballistically deposited on the tower. This sample is unique in that both the substrate and deposited material are both molybdenum, as verified using EDS. Ultramet

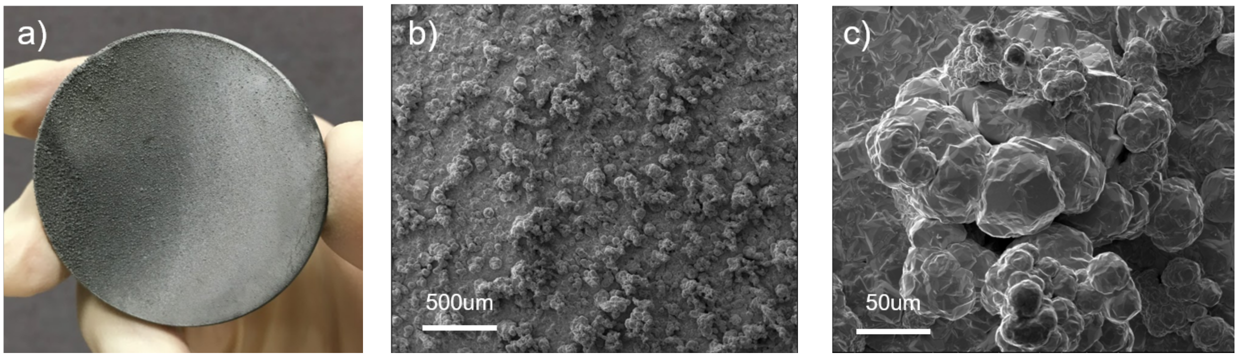

Figure 5.9: The above images show a) the structured molybdenum sample b) a magnified SEM image showing a field of bulbous surface features and c) a zoom-in on a particular protrusion.

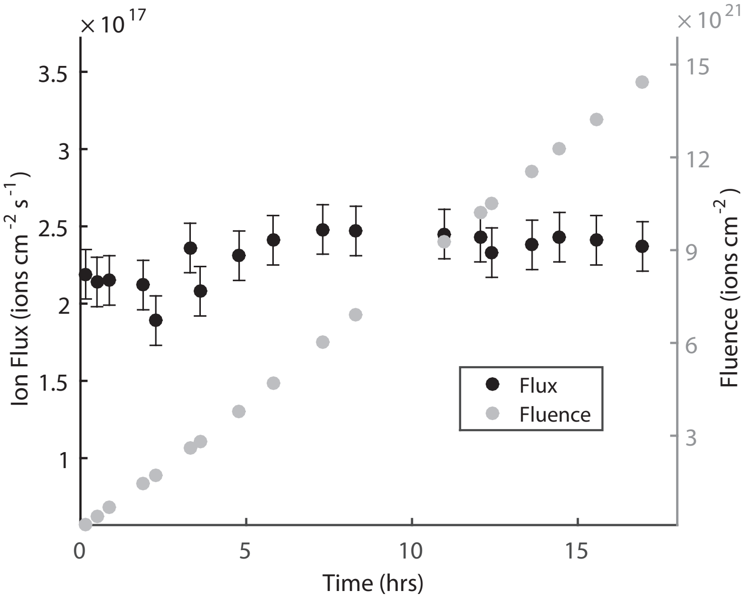

Figure 5.10: The ion flux is monitored over the total test duration and combined with the exposure time to calculate the ion fluence. Time is found to be approximately linearly proportional to the fluence due to the relatively unchanging ion flux.

also produces other micro-featured surfaces with varying substrates and surface topologies such as reticulated metallic foams and dendritic surfaces with spears and caps[33, 91].

The sample was tested for a total duration of 17 hrs for the sputtering yield to converge to a constant value. The ion energy was fixed at 300 eV and the plasma was operated using the same conditions as the flat molybdenum test. The plasma density and electron temperature were constant to within 10% of the values shown in Table 5.1, and the average ion flux was measured to be $(2.3 \pm 0.2) \times 10^{17}$ ions cm^{-2} s^{-1}.

The QCM was used to measure the angular sputtering distribution at discrete time intervals during plasma exposure. By using a QCM scan duration (13 min) shorter than the characteristic erosion time (about 1 hr based on previous experiments), the time-dependent angular sputtering profile was measured. The integrated sputtering yield is described as a function of the ion fluence, $\mathscr{F}$, which is defined as the total number of ions incident on the target per unit area:

$$\mathscr{F} = \int_{t_0}^{t_1} F_i(t)\ dt, \tag{5.1}$$

where $F_i(t)$ is the measured ion flux. As shown in Figure 5.10, the ion fluence can be used in place of time as the dependent variable through the above calculation.

The featured surface is modified based on the total ion fluence and produces a unique sputtering profile that evolves in time. Since the plasma sheath size is much larger than the height of micro-features, the ions will strike the surface at varying angles, which also influences the ejection angle of sputtered particles. When an ejected target atom intercepts a nearby surface structure, it re-deposits on the material. This geometric re-trapping of sputtered particles is known as ballistic deposition and both modifies the angular sputtering distribution and decreases the overall sputtering yield[91, 95].

The evolution of the angular sputtering distribution for the micro-architectured molybdenum sample is shown in Figure 5.11. The initial measurement at t = 0.16 hrs shows a profile that is overall lower in magnitude and not significantly peaked off axis. The relatively flat profile for the interior angles results from ions striking the surface structures at varying incidence angles, which depends on the specific geometry of the features. The intermediate profile at t = 3.31 hrs develops a local maximum near 45° and increases in magnitude relative

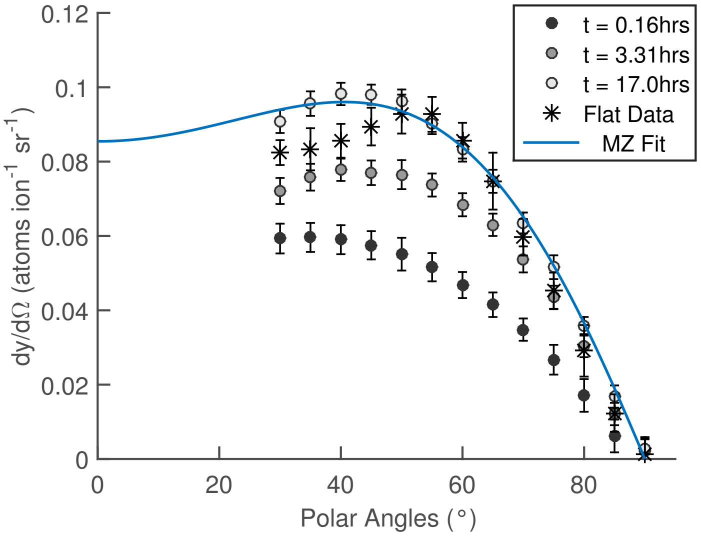

Figure 5.11: The differential sputtering yields for micro-architectured molybdenum are shown at three different times in comparison with the flat molybdenum results. The fluences for t = 0.16, 3.31, and 17.0 hrs are $\mathscr{F} = 1.2 \times 10^{20}$, 2.6×10^{21}, and 1.4×10^{22} ions cm^{-2} respectively. The final dataset at t = 17.0 hrs, or $\mathscr{F} = 1.4 \times 10^{22}$ ions cm^{-2}, is fit to the Modified-Zhang (MZ) profile.

to the initial profile, indicating an increase in sputtering yield. For the final measurement at t = 17.0 hrs, the angular distribution closely matches the results presented for the flat molybdenum sample at 300 eV for $\alpha > 50°$, but shows some deviation for the interior angles. Due to the presence of the plasma column, the QCM does not record data at angles $\alpha < 30°$, thus data are not available to confirm whether the discrepancy remains for ejection angles closer to $\alpha = 0°$.

The classical picture of the dependence of differential sputtering yield on the incidence angle for flat surfaces appears to be violated in samples with micro-architectured surfaces. The surface structures modify the distribution of incidence angles from purely normal to a function that depends on the surface geometry. As shown in Figure 5.11, the angular sputtering profile is also a function of time, and equivalently the ion fluence, evolving as the surface morphology changes. The surface features suppress the $1/\cos(\alpha)^f$ dependence at small fluence and give a flat angular dependence, up to angles of about 50 degrees. As

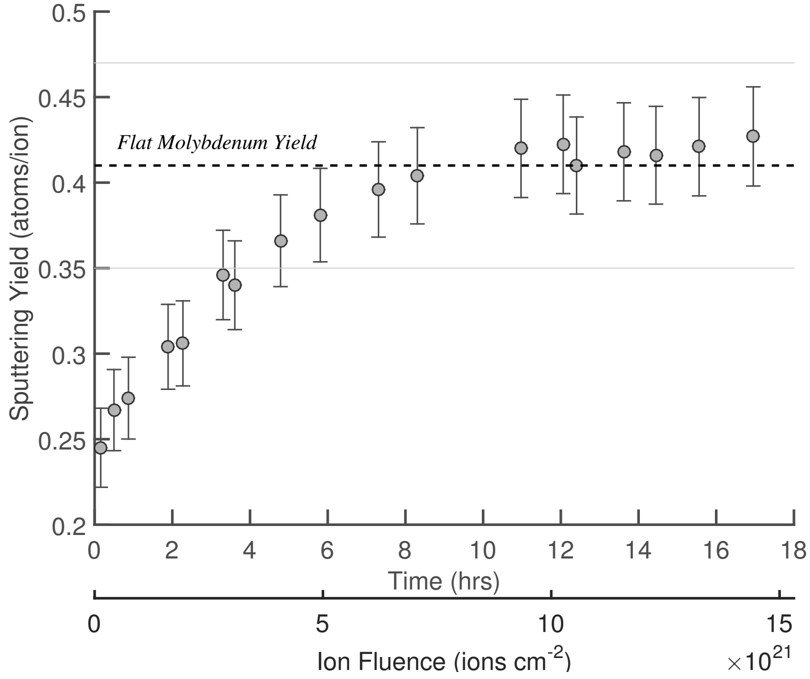

Figure 5.12: The time-dependent sputtering yield for 300 eV argon ions incident on micro-architectured molybdenum is shown converging to the flat molybdenum result. The gray lines signify error bars for the flat sample measurement.

the surface is eroded, the angular dependence approaches the classical picture, where the competition between the two physical mechanisms produce a marked maximum around 50 degrees.

By integrating the differential sputtering profiles, the total sputtering yield is obtained as a function of time, or fluence, as shown in Figure 5.12. The sputtering yield begins at approximately 0.24 atoms/ion when the micro-features are all intact. As the surface is sputtered, the yield is measured to increase until the structures are entirely eroded, leaving a flat surface sputtering yield of around 0.42 atoms/ion. The converged yield closely matches the value measured for the flat molybdenum tests reported in the previous section, and the small deviations are well within the error bars. Since the incident plasma has a Gaussian profile, the center of the target is eroded at a significantly higher rate than the edges. Therefore, the surface features at the edges may continue to erode and the sputtering yield

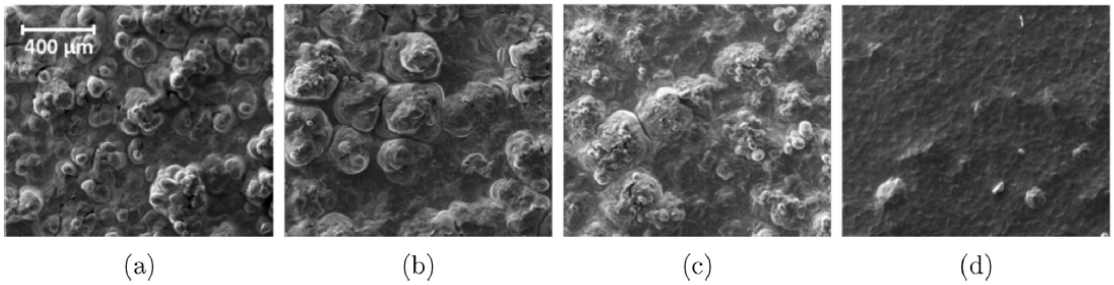

(a) (b) (c) (d)

Figure 5.13: The morphological changes of the structured molybdenum sample are shown in a) to d). Source: C. Matthes et al. (2017)

will increase slightly, although the change will likely be much smaller than the error bars of the measurement.

Contamination of the surface layer by oxidation can strongly affect the surface structure evolution and reduce the measured sputtering yield. To ensure the ballistic deposition of the surface is due to the sample material, EDS spectra are acquired to provide a measure of the gross contamination. Ref[91] shows that the surface composition was initially 7.58% oxygen by weight as a result of the fabrication process. After testing, the oxygen content was reduced to 1.93%, indicating that the surface was cleaned during plasma exposure. Residual gas analyzer measurements taken prior to testing revealed water and oxygen partial pressures of 10^{-7} Torr. At such low partial pressures and large ion fluxes, the oxide monolayer formed at a sample temperature of 500°C can be expected to be eroded away relatively quickly compared to the multi-hour exposure time, minimizing the presence of dynamic contamination. Additionally, the erosion scales are on the order of hundreds of microns, well beyond the scale of any surface contamination, which would be on the order of around 10 nm. Therefore, in situ measurements of dynamic contamination are outside the useful scope of the present experiment.

In Figure 5.13, SEM images of the structured molybdenum sample show the surface evolution. The images were taken between exposures and show how the surface structures erode under ion bombardment and grow via ballistic deposition. After the final plasma exposure, the effective exposure area of the sample ($d < 1.5$ cm) is essentially flat, with lightly eroded structures just outside the center that transition to almost untouched structures at the edges. The gradient in erosion characteristics is a result expected for the Gaussian ion flux profile. Overall, the microscopy observations demonstrate the overall flattening of the micro-architectured surface which explains the convergence of the sputtering yield to the flat sample result.

5.3 Conclusions

These results validate the Pi facility diagnostics for both characterizing the incident plasma and the sputtering of the material samples. The QCM collection method was benchmarked using an argon ion on flat molybdenum experiment and showed good agreement with results from the literature. Following this work, the time-resolved sputtering yield of a structured molybdenum sample was measured for the first time. The angular sputtering profile and total sputtering yield as well as the surface morphology were shown to evolve with ion fluence and converge to the flat sample result.

CHAPTER 6

Plasma Foam Sputtering Experiments

The micro-architectured molybdenum test showed that any featured surface will have a transient sputtering yield that increases over time and approaches the flat yield as surface features are eroded away. While the temporary reduced yield may be sufficient for applications requiring short lifetimes, a sustained reduced sputtering yield is desired for most plasma devices. The solution to this problem of limited erosion time is solved by using a volumetrically architectured material such as an open cell foam which retains structure as the top layers are removed. In this section, the fundamentals of plasma-foam sputtering theory is discussed and the first experiments measuring the effective sputtering yields of aluminum foam are presented.

6.1 Literature Review

Early studies of foam sputtering in the 1970s were motivated by cosmic ray bombardment of lunar regolith[96]. Hapke and Cassidy assert that previous calculations of sputtering yield from the lunar regolith assuming a flat surface overestimated the true yield and that the complex micro-geometry in the lunar soil will result in a reduced yield. Subsequent investigations modeled the regolith as nanoporous foam bombarded by high energy (> 1 keV) ions using molecular dynamic (MD) simulations. Anders et al.[97] simulated the bombardment of Au by 10 keV Au^+ and found a general reduction in the sputtering yield compared to a flat target. They studied the thermal spike behavior as high energy ions effectively melt the surface and cause a transient ejection of molten material. Their results emphasized the need to study the sputtering or porous structures as an ensemble of nanorods as opposed to individual ligaments. Rodriguez-Nieva et al.[98, 99] also used MD simulations to model the electronic sputtering of nanoporous solids. The authors explain that models of the sputtering yield require knowledge of the foam porosity and filament size compared to the ion range. Thermal spike sputtering have ion ranges typically much larger than the ligament diameter which leads to impacting ions scattering through multiple filaments. Their results also indicate that sputtering of microporous foam has significantly different characteristics compared to nanoporous foam.

Cassidy and Johnson[100, 101] developed a Monte Carlo model to simulate the sputtering of microporous lunar regolith or planetary rings by high energy solar radiation. The lunar regolith is represented as a matrix of spherical grains with micrometer dimensions in contrast with the nanofoams discussed in the previous paragraph. The sputtering model incorporated the ion angle of incidence and intrinsic material properties such as grain size and shape. The authors found that the regolith yield was generally less than that from flat material and depended on the sticking probability. The sticking probability is used as an adjustable parameter in the model and allows the authors to explore variations in the yield. The angular sputtering profile from the regolith was found to be insensitive to changes in sputtering parameters and the grain shape had little effect on the total effective sputtering yield. The approach in this paper is adopted for the analytical plasma-foam sputtering model discussed in Chapter 7.

Gao et al.[102, 103] tested the sputtering of micro-engineered tungsten foams under low energy helium ion bombardment. The experiment was conducted in the PISCES test facility at UCSD with a plasma discharge and the primary focus was to assess helium bubble and fuzz formation. The foams were 45 and 80 Pores Per Inch (PPI) and had nanofeatures deposited onto the foam ligaments. The authors found that the sputtering yield of the reduced compared to planar tungsten when nano-nodules were used and increased when rhenium nano-pillars were used. The helium-exposure was also found to produce modified

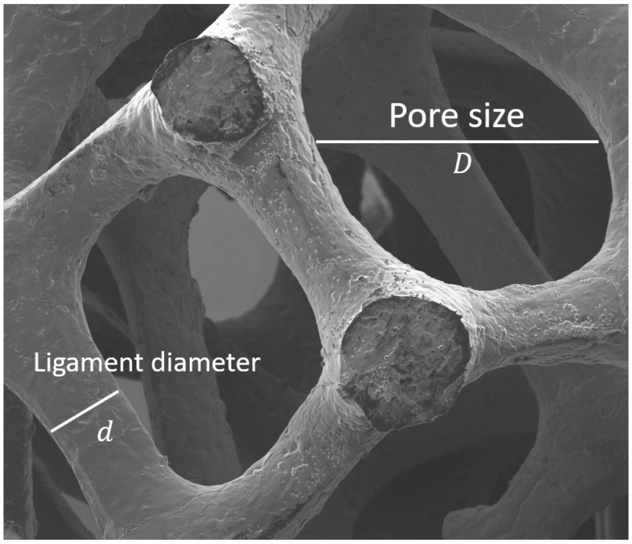

Figure 6.1: General foam structure and important geometric parameters.

fuzz and bubble formations relative to planar tungsten. The results are promising and indicate that there are a plethora of plasma-foam interactions that remain to be understood. The next section will introduce the theory of plasma-foam sputtering and present the first experimental measurements of the time-dependent sputtering yield for low energy heavy ion sputtering.

6.2 Plasma Foam Sputtering Theory

Plasma-foam sputtering is a complex non-linear process in which plasma can potentially infuse the foam and cause a cascade of sputtering and redeposition events throughout the material. A plasma-exposed foam is particularly unique in that the acceleration mechanism occurs through the plasma sheath, which is a finite thickness boundary layer with an electric field. The sheath can be located outside the foam or inside the foam itself depending on both the foam and plasma properties. The ejected material from bombardment by energetic ions is likely to be recaptured by adjacent filament structures and thereby reduce the effective sputtering yield.

Fundamentally, the plasma-foam sputtering behavior will depend on the interaction of the plasma sheath with the foam structure. The basic geometry of a metallic foam is shown in Figure 6.1. The Debye length, λ_D, is a physical length scale representing the plasma sheath while the pore diameter, D, is the natural length scale for the foam. The sheath thickness is typically 5 - 20 times the Debye length and is given by the Child-Langmuir law for a negative-going cathode sheath, $L_s/\lambda_D = \sqrt{2}/3(2e\Delta\phi_s/T_e)^{3/4}$ where $\Delta\phi_s$ is the sheath voltage drop and T_e is the electron temperature. When $D \ll L_s$, the sheath is planar relative to the macroscopic surface of the foam as is typically seen for plasma sputtering experiments. However, in the opposite limit where $D \gg L_s$, the sheath begins to conform to the foam ligaments and the plasma is allowed to enter through the foam pores. Kim and Economou[104, 105] termed the conforming effect plasma molding in the context of plasma processing with ion optics grids or surface microfeatures. For foams, the plasma infusion effect is volumetric and allows for the definition of a plasma-infusion parameter, $\xi = D/\lambda_D$. In order for the plasma to begin infusing the foam, the criterion $D > L_s$ must be satisfied. The expression can be rearranged to give

$$\xi = \frac{D}{\lambda_D} > \frac{\sqrt{2}}{3}\left(\frac{2e\Delta\phi_s}{T_e}\right)^{3/4} = \xi_c. \tag{6.1}$$

where the Child-Langmuir sheath thickness is substituted in the plasma-infusion criterion. The limit $\xi \ll \xi_c$ is the familiar case where the sheath size is much larger than the characteristic pore size or any surface features. This scenario is seen for typical plasma sputtering of planar surfaces where any microfeatures and significantly smaller than the sheath thickness. Therefore, the plasma-facing regime can be defined for this limit where all ions are accelerated normal to the foam surface via the sheath electric field and given an energy $E = \Delta\phi_s$. As shown in Figure 6.2, ions will either impact the surface ligaments or penetrate the foam through the pores with some characteristic depth, δ_f. The solid substrate beneath the foam layer will not be exposed to plasma if the thickness of the foam is sized to be larger than the penetration depth ($t > \delta_f$). For fixed plasma conditions (n_e, T_e), this regime can be examined by utilizing the smallest pore sizes possible.

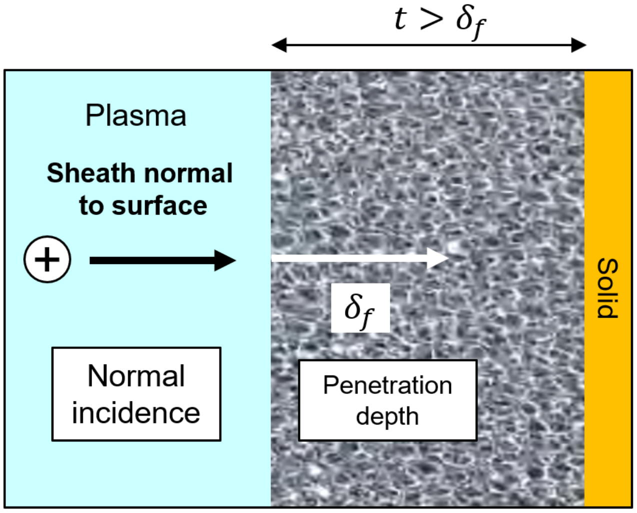

Figure 6.2: Plasma-facing regime: the plasma sheath is external to the foam and ions are accelerated normal to the foam surface.

In the opposite limit where the pore sizes are much larger than the sheath size $\xi \gg \xi_c$, the bulk plasma infuses the foam structure in what I define as the “plasma-infused regime”. As shown in Figure 6.3, the sheath conforms to the ligament surfaces and ions impact the ligaments locally at normal incidence. In this simplified picture, 1D sheath theory applies and it can be assumed that the ion energy is equal to $E = \Delta\phi_s$ for ions generated in the bulk plasma. If the ion is born in the foam itself, there may potential gradients from the external bulk plasma into the foam that result in lower energy ions $E < \phi_s$. In addition, the ion flux to the ligament surfaces is determined by the local plasma density from the Bohm current, $I_B = n_e e\sqrt{k_B T_e/M}$. The local ion flux is therefore sensitive to any plasma density gradients in the foam which may result from an increase in effective plasma loss area. The ligament sputtering area is also significantly larger than the plasma-facing case since all ligaments are sputtered instead of only the plasma-facing cross-sectional area. Therefore, it can be predicted that the sputtering yield will increase relative to the plasma-facing case due to this larger effective sputtering area.

If the thickness of the foam is smaller than the characteristic plasma penetration depth, then the plasma will reach the solid substrate. Sputtering of the solid surface will result in backsputtering towards the entrance plane with some characteristic length, δ_b. This scenario typically occurs for samples with large pore sizes on the millimeter scale. Full plasma-infusion allows the sputtering process to occur throughout the volume of the foam and can even serve as an intermediate medium between the plasma and the underlying solid surface. If the solid surface is exposed to the plasma, the material can be sputtered and deposited on the nearby ligaments and the amount of material ejected into the plasma itself is limited. The selective sputtering transport of a plasma-infused foam enables new possibilities for plasma devices that are sensitive to contaminants from the material surfaces.

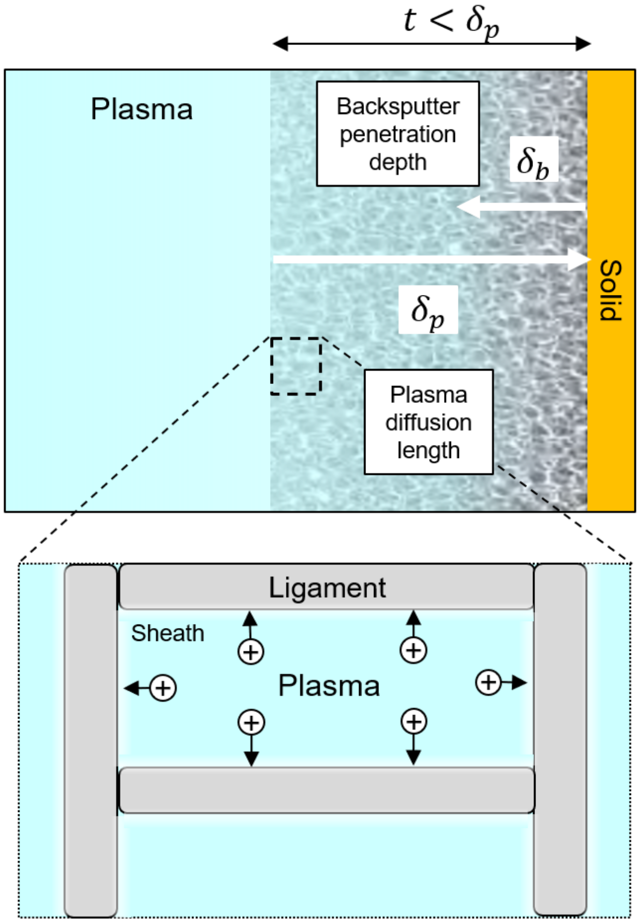

Figure 6.3: Plasma-infused regime: the plasma infuses the foam and sheaths are formed parallel to the ligament surfaces, accelerating ions normal to the ligaments throughout the foam volume.

In the transitional regime where $\xi \sim \xi_c$, many of the simplifications of the two extreme limits do not apply. In both the plasma-facing and plasma-infused regimes, the sheath geometry is simplistic because the 1D sheath theory can be applied either for the macroscopic surface or the local ligaments. However, in the transitional regime, the sheath size is on the same order as the pore size in which case 2D/3D plasma molding effects are present[104, 105]. Kim and Economou study the effects of plasma molding on the ion flux, ion energy distribution, and ion angular distribution which are heavily dependent on the sheath edge geometry. Watterson[106] shows that a 2D plasma sheath results in a higher ion flux rate and oblique angles of incidence on a wedge surface, which can consequently increase the effective sputtering yield of the foam. In contrast to the plasma-infused case where the effective sputtering area is increased due to the plasma-exposed ligaments, the transitional regime sputtering yield increases due to the higher flux and larger local sputtering yields at oblique angles of incidence. In general, the transitional regime behavior is important to understand as many relevant plasma devices operate in this realm of $\xi \sim \xi_c$ and computational models may be necessary to extract detailed ion trajectory behavior.

The length scales described thus far include the sheath thickness, L_s, the pore size, D, the foam thickness, L, the ion penetration depth, δ_f, and the backscatter penetration depth, δ_b. The additional length scales of interest include the ion range, R, and the ligament width, d. The ion range is the characteristic depth that ions penetrate a solid surface due to the ion-material interaction calculations, while the ligament width is determined by the foam fabrication process. If the ion range is much larger than the ligament depth ($R \gg d$), then the ion can penetrate through the ligament and scatter to a different ligament behind it. In the limit that the pore sizes go to zero, then the ion essentially sees the foam as a solid material and the sputtering behavior will be the same as that of a flat surface. If the ion range is much less than the ligament width ($R \ll d$), then the ion impact will cause a local collision cascade of the ligament atoms and only the impacted ligament will be affected. The ion range is a function of the incident ion energy and is larger for thermal spike regime sputtering. Past studies have shown that the ion range is less significant for linear cascade sputtering in low energy ion bombardment which is the focus on this dissertation.

The "effective" sputtering yield of a foam structure can be expressed in terms of the value for a flat material[97]. Consider a foam material with flat elemental sputtering yield $Y(p = 1)$ and porosity, $0 < p < 1$, which is equivalent to the open area fraction of the plane normal to the incident ion. The minimum effective sputtering yield can be found by assuming all normally incident ions that enter the foam through the pores produce sputterants that are trapped within the foam:

$$Y_{\text{min}}(p) = pY(p = 1). \tag{6.2}$$

However, the sputtered atoms that are emitted from the ligaments from within the foam has a finite probability of traversing to the entrance plane. Therefore, the actual effective sputtering yield must be modified by an escape factor, $\eta > 1$:

$$Y_{\text{eff}}(p) = p\eta Y(p = 1). \tag{6.3}$$

The effective sputtering yield is difficult to calculate analytically due to the complex non-linear nature of calculating the escape factor. A simple model capturing the physics of plasma-foam sputtering will be discussed in the following chapter. The next section will present the results of plasma-foam sputtering experiments and the first reports of the time-dependent sputtering yield.

6.3 Aluminum Foam Sputtering Experiments

The Duocel aluminum foams tested in this dissertation are manufactured using investment casting with polymer foams[107]. The foam structures are isotropic and have interconnected 14-faceted cells connected by thin cylindrical ligaments as shown in Figure 6.4a. These foams can be either metallic or ceramic, have a range of pore sizes from 100 PPI to 5 PPI, and have relative densities from 2% to 20% ($\rho_{\text{foam}}/\rho_{\text{solid}}$).

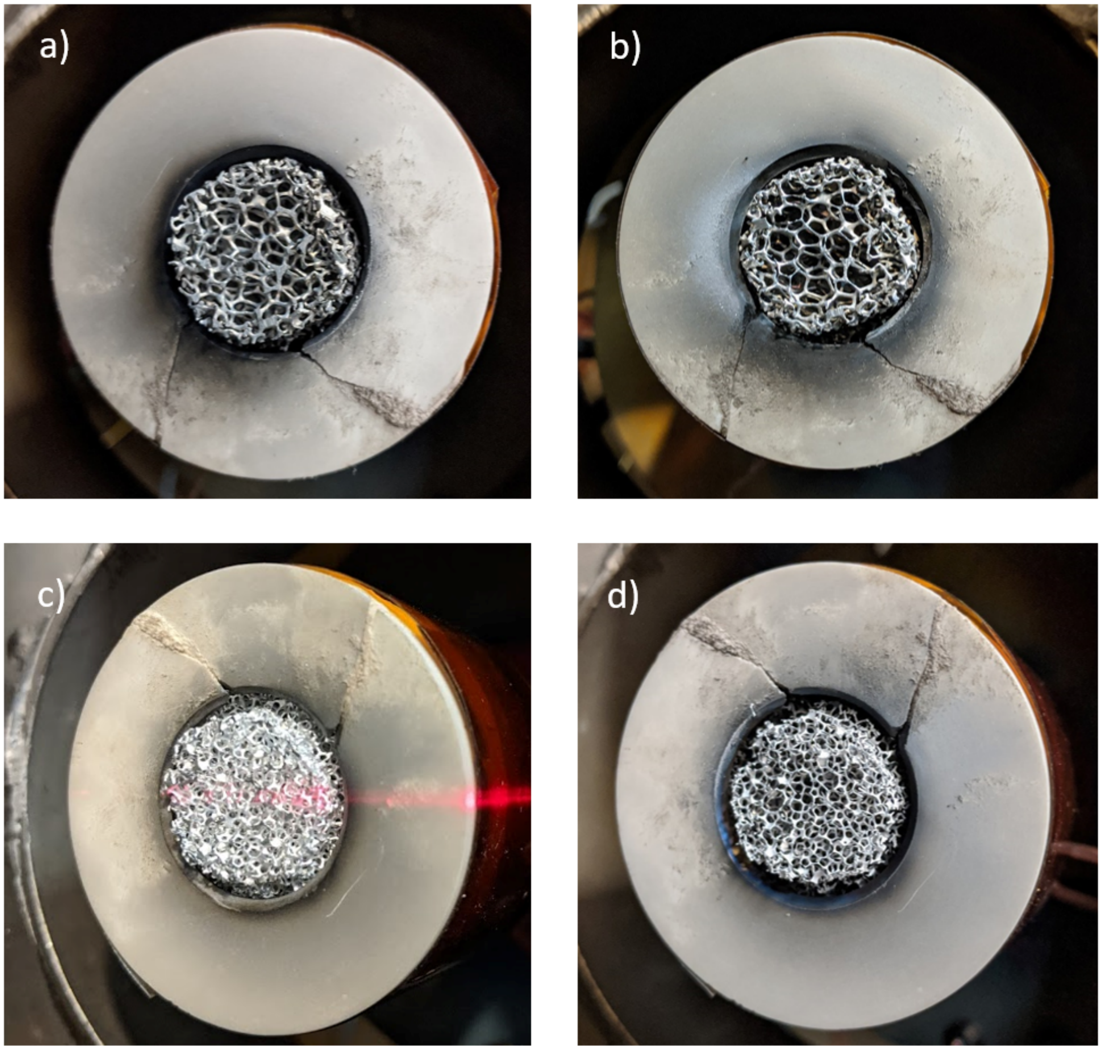

Figure 6.4: Figures a) and b) show the 10 PPI aluminum foam before and after plasma exposure and figures c) and d) show the 40 PPI foam before and after plasma exposure in a macor mounting structure.

The samples used in this dissertation are 10 PPI and 40 PPI aluminum foams with 8% relative density shown in Figures 6.4a and 6.4c respectively prior to plasma exposure. The samples are milled into a disk with a 0.84 in central diameter and a lip with an outer diameter of 1.22 in for mounting the sample. The 10 PPI sample is shown in a ceramic mount which is placed into the plasma column for testing. The foams have pore diameters of $D \approx 0.6/\text{PPI}$ and ligaments are cylindrical struts with diameter, d. The calculated pore sizes are 1.5 mm and 380 μm for 10 PPI and 40 PPI foams respectively and ligament diameters are 415 μm and 112 μm. The aluminum chemical composition is approximately the same as that of the casting 6101 aluminum alloy. Samples were cleaned prior to measurements to remove surface impurities and round sharp corners. The surface cleaning was achieved using low energy ion bombardment with 100 eV Ar^+ bombardment with an ion flux of $F = 2 \times 10^{17}$ ions/(cm^{2}s).

The samples were both tested for a total 30 hours with similar conditions to the flat and structured molybdenum tests. The test time was determined based on a thickness erosion calculation for foam ligaments. For 300 eV Ar^+ with a flux of 2×10^{17} ions/(cm^{2}s), the aluminum sputtering yield is taken to be 0.5 atoms/ion[108]. The thickness of one layer is given by the filaments which have diameters of 415 μm and 112 μm for 10 PPI and 40 PPI foam respectively. The erosion time for a single ligament is found to be 2 hrs and 7 hrs for 10 PPI and 40 PPI foams respectively. For a 30 hour exposure, the 10 PPI foam will have on order of a single layer of erosion while the 40 PPI foam should have multiple layers removed.

The 10 PPI and 40 PPI aluminum foams were tested in the Pi facility with the same plasma conditions as described in Chapter 5. The average centerline plasma properties are $n_e = 10^{17}$ m^{-3} and $T_e = 5$ eV. The Debye length is calculated to be $\lambda_D = 50$ μm and the corresponding sheath size is $L_s = 855$ μm with a sheath potential of 300 V. Therefore, the plasma-foam sputtering regime can be determined by the parameters $\xi_{10} = D/L_s = 48.3$ and $\xi_{40} = 12.1$ with $\xi_c(300\ V) = 17.1$. The ξ parameters are fixed for these experiments based on the measured centerline plasma properties and pore dimensions while ξ_c is a function of the applied bias voltage. Given these parameters, the 10 PPI foam is near the plasma-infused regime with $\xi_{10} > \xi_c$ while the 40 PPI foam is in a transitional regime, $\xi_{40} \sim \xi_c$, with expected behavior from both regimes as described previously.

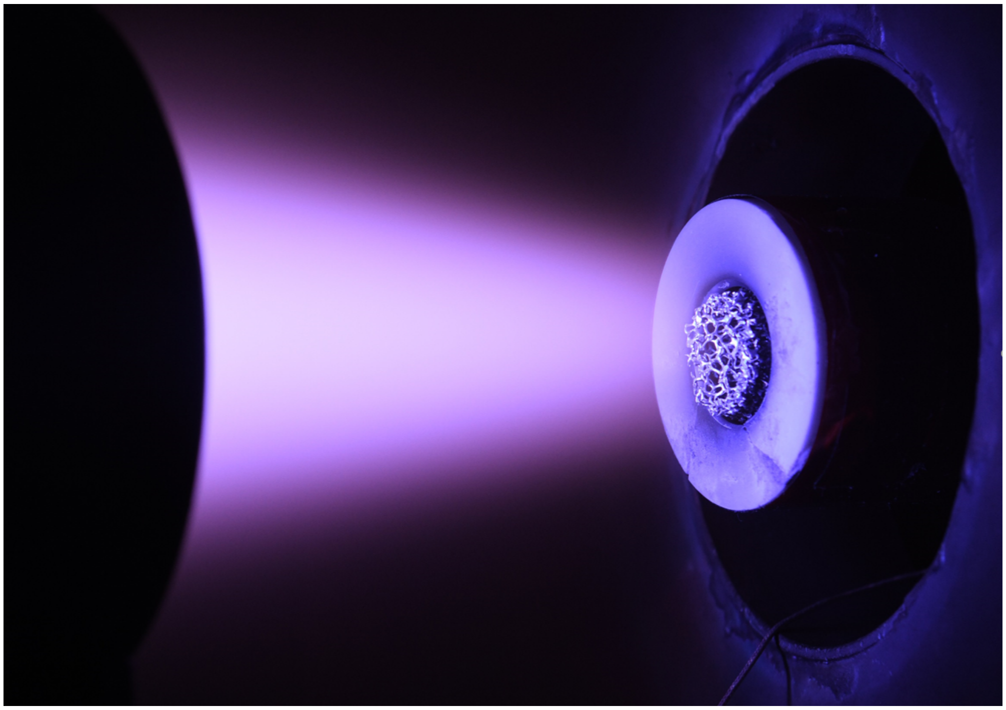

Figure 6.5: 10 PPI foam in the Pi facility.

6.3.1 Scanning Electron Microscopy Results

Figure 6.6 show Scanning Electron Microscope (SEM) images of the 10 PPI and 40 PPI aluminum foams. Figure 6.6a and 6.6b show the 10 PPI foam before and after plasma exposure respectively at a location 4.3 mm radially outward from the center of the sample. The overall structure appears to be unchanged after plasma erosion but the ligaments in the front layer are clearly thinned. The second layer seems slightly eroded but the difference could be attributed to a varying viewing angle in the SEM. Since the erosion was primarily on the top layer, it is unlikely that the foam was fully plasma infused as predicted by $\xi_{10} > \xi_c$. Figure 6.7 shows a thin film deposited on the solid surface behind the 10 PPI foam after plasma exposure. The ligament-shaped deposition indicates that the shadowed, or backsides, of the ligaments were indeed sputtered which is only possible with at least partial plasma infusion. As the backsides of ligaments are sputtered, the layer of filaments near the mount surface intercept sputtered particles to create the shadowing effect.

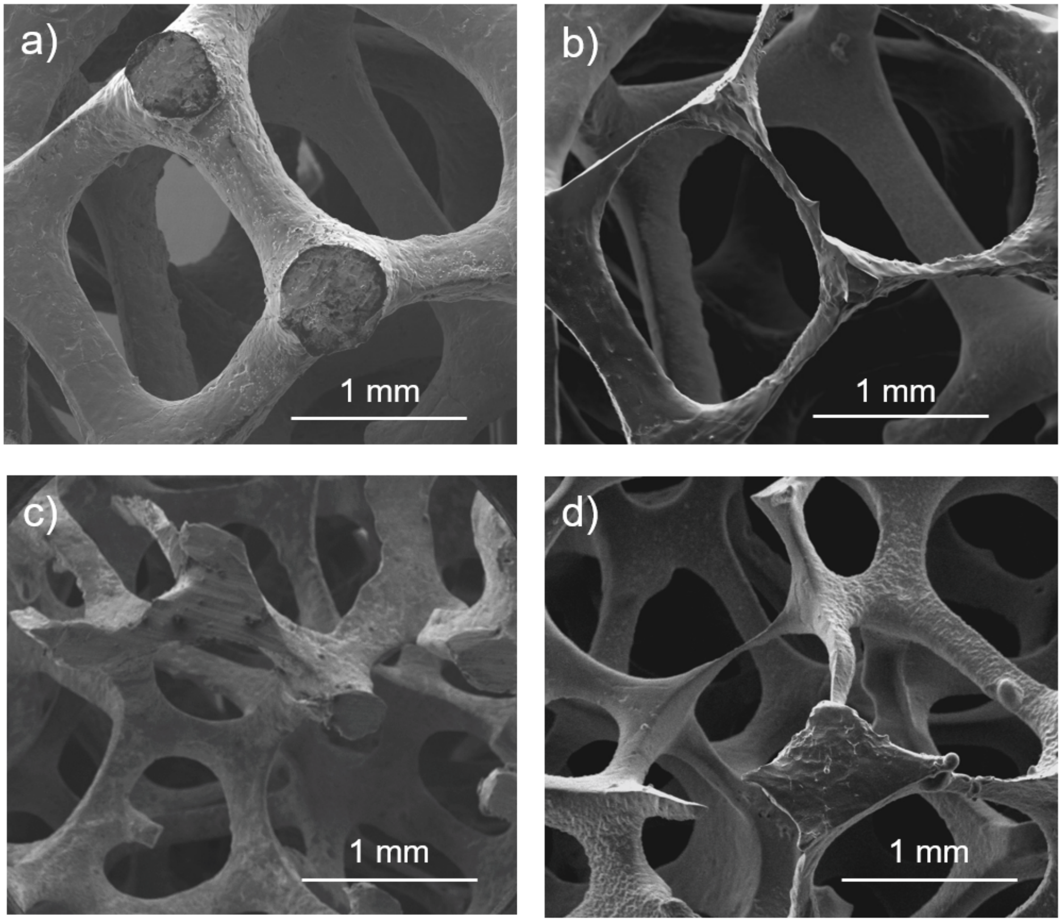

Figure 6.6: The figures show the 10 PPI aluminum foam at a location 4.3 mm radially outward from the center a) before and b) after plasma exposure and the 40 PPI aluminum foam 10 mm outward from center c) before and d) after plasma exposure.

It is also possible that the partial plasma infusion was due to the density gradient across the sample resulting in a larger Debye length and therefore larger ξ_{10} required for plasma-infusion. A Gaussian density profile results in a 41% decrease in the plasma density at the location corresponding to Figures 6.6a and 6.6b. A 41% decrease in density will result in a 33% increase in the Debye length with $\lambda_D = 68.0$ μm and gives $\xi_{10} = 37.4$ with the same $\xi_c = 17.1$. A lower ξ implies the plasma is closer to the transitional regime where the sputtering will have partial plasma-infusion but also plasma-facing ion characteristics. The

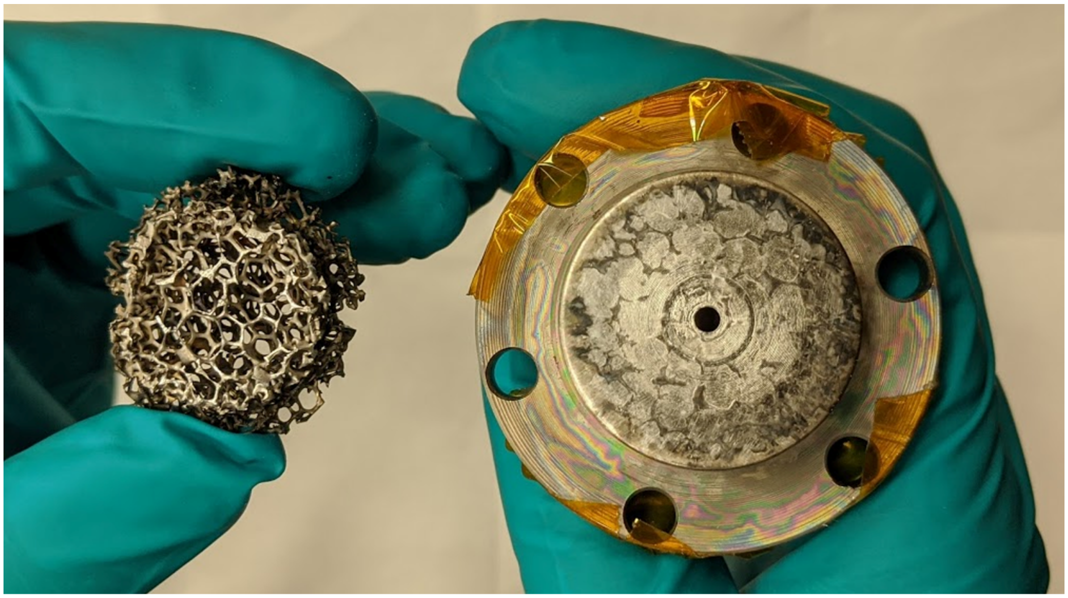

Figure 6.7: The 10 PPI foam and mounting structure after exposure showing the sputter coating of the surface.

observation of ligament shadowed deposition on the mount was also not seen on the 40 PPI sample which has a lower ξ.

The 40 PPI sample shown in Figure 6.6c and 6.6d show the pre- and post-exposure image. As predicted in the thickness erosion calculation, multiple layers were removed so the two images look completely different. The foam retains the self-similar structure after long duration erosion rather than eroding to a flat surface like a material with only microfeatures on a plane. Based on this observation, the sputtering yield should remain relatively constant as shown later in Figure 6.9. The general sputtering characteristics can be seen as the cylindrical struts are eroded into triangular struts with wider sections at the section. On some ligaments, there are rough surface features generated from the deposition of sputtered particles as shown in Figure 5.6d. The ion bombardment results in smoothing of surfaces where there is a large ion flux, but the regions with lower bombardment will allow the growth of deposited features. Both the 10 PPI and 40 PPI foams had similar deposition on the less perturbed ligaments.

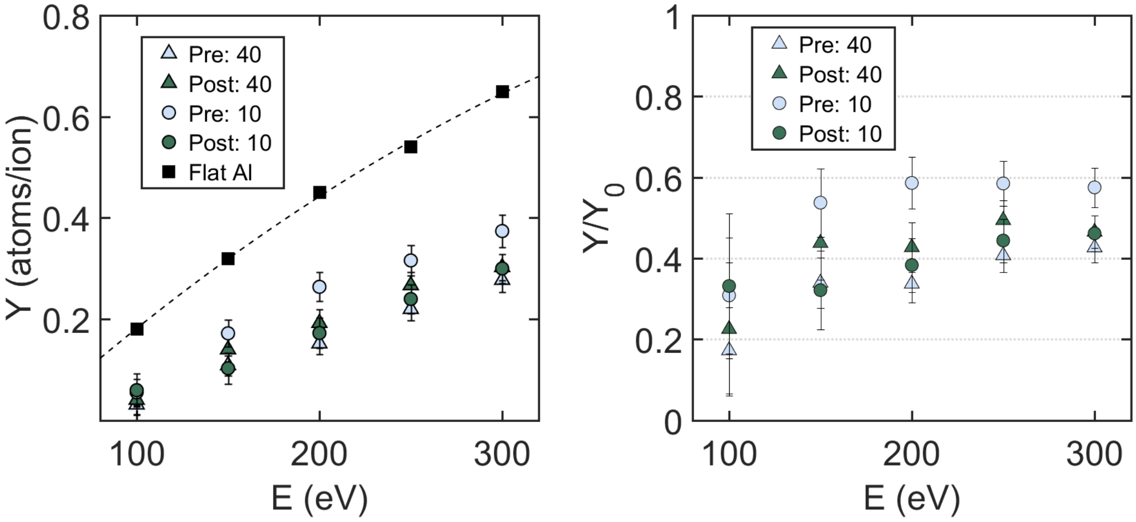

Figure 6.8: The figures show (left) the effective sputtering yield of 40 and 10 PPI aluminum foams as a function of energy before and after plasma exposure and (right) the same sputtering yields normalized by the flat aluminum yields.

6.3.2 Sputtering Yield Results

QCM measurements were performed during plasma exposure as a function of varying ion energies at the beginning and end of test and also as a function of time at a fixed ion energy of 300 eV. Figure 6.8 shows the effective sputtering yield at ion energies of 100 eV to 300 eV in increments of 50 eV. The data is also shown normalized by the flat aluminum yield which is shown at each energy setpoint[20]. The 40 PPI yields increase slightly after exposure and the 10 PPI decreases by as much as 20%. The erosion of several layers in the 40 PPI foam explains why the yield has minimal change since the exposed layers have the same structure as the initial top layer. The ligament thinning in the 10 PPI foam may explain the larger decrease in yield at most energy setpoints. The main observation is that there is a larger reduction in yield at lower energies, particularly 100 eV. Since 100 eV is close to the sputtering threshold energy, the angular distribution is expected to have larger deviations from the standard cosine profile. The off-axis peaks in angular sputtering profiles may lead to a higher recapture fraction which can decrease the yield even further. An 80% reduction in effective sputtering yield at 100 eV may be revolutionary in plasma devices

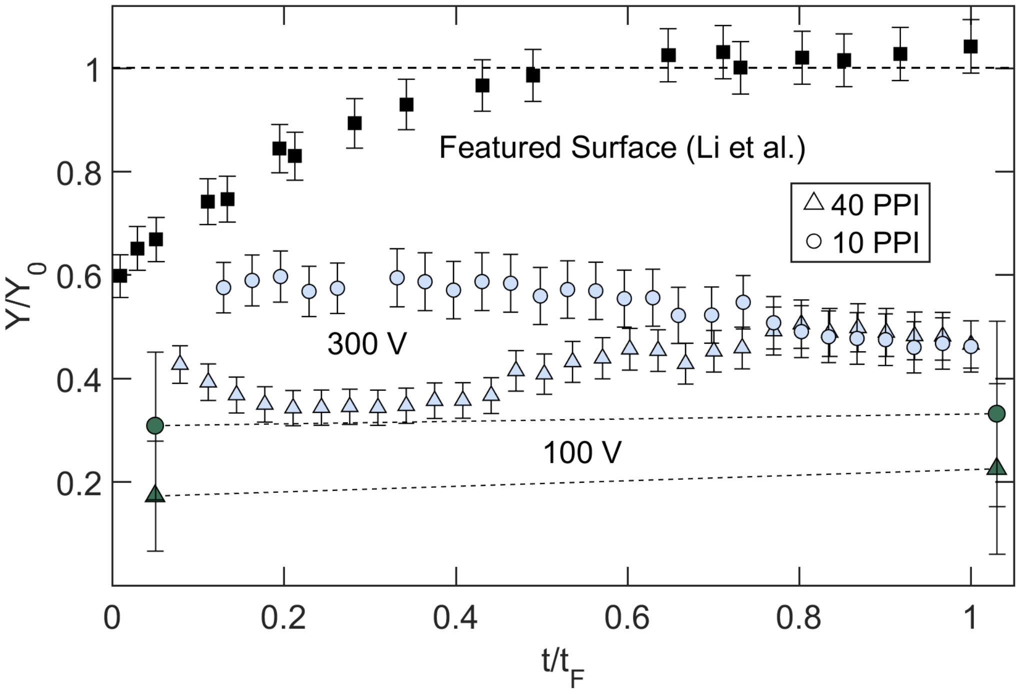

Figure 6.9: The normalized sputtering yield of 40 and 10 PPI aluminum foams as a function of normalized time. The 300 V data was taken over a 30 h exposure while the 100 V data was taken before and after the long duration exposure. The data from Li et al. (2017) is shown for a featured molybdenum surface.

with sputtering in the sub-100 eV regime. Hall thruster channel erosion and tokamak first wall and divertor erosion all have sheath-accelerated ion energies in this range. Another technique to utilize this effect would be to operate in conditions where the wall potential drop is near the sputtering threshold energy.

Figure 6.9 shows the time-dependent sputtering yield of the 10 PPI and 40 PPI foams with 300 eV Ar$^+$ bombardment. The sputtering yield and time are normalized by the flat aluminum yield of 0.5 atoms/ion and 30 hour total test time respectively. The sputtering yield of a featured molybdenum surface presented in Chapter 4 shows the characteristic approach to a flat yield as surface features are eroded away. The foams, on the other hand, show for the first time a sustained reduced sputtering yield due to self-similar structures being exposed as plasma-facing layers are removed. The 10 PPI yield has a normalized yield of 0.6 which decreases to 0.45 as the ligaments in the top layer are thinned. As shown in the SEM images, the top layer is not removed fully, leading to a decreasing yield over the 30-hr exposure. The 40 PPI yield starts with a normalized yield of 0.4 which oscillates roughly 0.1 about the mean value. The changes in yield can be attributed to structural changes as foam ligaments evolve over time and layers are removed. Based on the data, there is no clear dependence of the yield on the pore density in terms of PPI. In the following chapter, an analytical model is introduced to capture the key physical phenomena present in plasma-foam sputtering and interpret some of these experimental observations.

6.4 Conclusions

A basic plasma-foam sputtering theory introduces a plasma infusion parameter, ξ, which separates the behavior into two regimes: the plasma-facing regime where the plasma sheath is much larger than the pore size and forms external to the foam and the plasma-infused regime where the sheath forms locally next to all ligaments and surfaces are sputtered throughout the volume. The transitional regime where the pore size, D, is on order of the sheath thickness, L_s, has plasma molding effects where the 2D sheath structure is important for understanding the ion bombardment of the ligament surfaces. 10 PPI and 40 PPI aluminum foams are tested in the UCLA Pi facility with ξ parameters yielding transitional and plasma-infused behavior. Effective sputtering yields were measured as a function of energy and time. The yields were found to be reduced by up to 80% at lower energies showing the effects of sputtering near the threshold energy. In addition, both aluminum foams were exposed to 300 eV argon ions for 30 h, demonstrating for the first time a sustained reduction in yield of 40% to 60% compared to flat aluminum. The merits of plasma-facing foams undergoing low energy heavy ion bombardment are clear when compared to standard featured surfaces, and the low energy performance can be utilized for relevant plasma applications. The following chapter analyzes the experimental observations in the context of an analytical model.

CHAPTER 7

Plasma Foam Sputtering Modeling and Analysis

The aluminum foam experiment in the previous chapter presented the first sputtering yield results for low energy sputtering of microfoams. The yield was shown to be consistently reduced compared to a flat sample and revealed a dependency on ion energy and pore density. The experimental observations can be analyzed from a combination of plasma sheath and geometrical considerations. The objective of this chapter is to present an analytical model that can capture the key physical mechanisms in plasma-foam sputtering and interpret the results from the previous chapter.

7.1 Model Overview

Plasma-foam sputtering involves competing mechanisms that can reduce or enhance the effective sputtering yield. As a volumetric, open-cell material, foam has a lower density than a solid and allows sputtering to occur at sublayers below the surface. The separation into layers instinctively lends itself to layer-specific contributions to the effective sputtering yield. Each sublayer will include properties such as material opacity, effective sputtering area, ballistic deposition, and plasma density gradients which will be elaborated upon in the following sections.

A simple analytical model that captures all of these effects is summarized by the following equation

$$Y_{\text{eff}} = Y_{\text{flat}} \sum_{k=1}^{N} (1 - p^{(k)}) f_A^{(k)} f_\beta^{(k)} (1 - f_{\text{dep}}^{(k)}) f_{\nabla n}^{(k)} \tag{7.1}$$

where $p^{(k)}$ is the open area fraction of the k^{th} layer, f_A is the ratio of the sputtering area compared to a flat surface, f_β is the backsputter factor, $f_{\text{dep}}^{(\text{k})}$ is the ballistic deposition factor for the k^{th} layer, and $f_{\nabla n}^{(k)}$ is a plasma density gradient term. The sputtering yield contribution from the top-layer is given by $k = 1$ and has $Y_{\text{eff}} = Y_{\text{flat}}(1 - p^{(1)}) f_A f_\beta$ where $f_{\text{dep}}^{(1)} = 0$. The base case is an opaque flat surface which has $p^{(1)} = 1$ and $f_A = f_\beta = 1$ and the effective sputtering yield reduces to $Y_{\text{eff}} = Y_{\text{flat}}$. The intrinsic sputtering theory is captured in Y_{flat} and the focus of this analysis is on the additional effects introduced by the volumetric structure of the foam.

A 3D cage geometry with cylindrical ligaments is used to represent a simplified foam as previously utilized for a Secondary Electron Emission (SEE) model[109]. The cage has cells with pore size, D, and ligaments of diameter, d. The stochastic nature of the foam cell positioning is approximated by offsetting each subsequent sublayer by $D/2$ compared to the previous layer.

7.1.1 Material Opacity

The material opacity refers to the percentage of a planar layer covered by sputtering area. The opacity and the open area fraction, $p^{(k)}$, sum up to unity. The open area fraction can be calculated for each layer by considering a single pore opening and calculating each sublayer individually as shown in Figure 7.1.

The open area fraction of layer k is determined to be

$$p^{(k)} = \frac{\text{open area}}{\text{total remaining area}}. \tag{7.2}$$

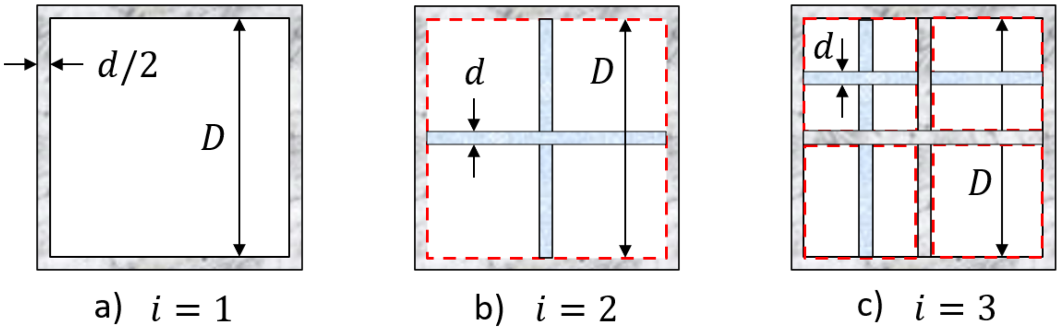

Figure 7.1: The diagrams show the individual layers $k = 1$ to $k = 3$ for a single pore used to calculate the open area fractions. The red dotted lines indicate the total area being considered for each layer, ignoring the sputtered area from the previous layers.

where the total remaining area denominator is meant to exclude sputtering area accounted for in previous layers. The first layer, $k = 1$, as shown in Figure 7.1a has

$$p^{(1)} = \frac{D^2}{D^2 + 4(\frac{d}{2}D) + 4(\frac{d}{2})^2} = \frac{1}{1 + \frac{2d}{D} + \frac{d^2}{D^2}} \tag{7.3}$$

where $d/2$ is used for the thickness of the half-ligaments to exclude overlap with adjacent pores. In the limit $d \ll D$, the open area fraction for layer $k = 1$ can utilize a Taylor expansion to simplify the expression to

$$p^{(1)} = 1 - \frac{2d}{D} \tag{7.4}$$

where the error in the approximation is $\mathcal{O}(d^2/D^2)$. Similarly, for the second layer, $k = 2$, the open area fraction is

$$p^{(2)} = \frac{D^2 - (2dD - d^2)}{D^2} \approx 1 - \frac{2d}{D} \tag{7.5}$$

where the 2nd layer is oriented such that the ligament intersection is at the center of the pore, maximizing the sputtering area. The denominator corresponds to the total remaining area after subtracting out the ligament area in the 1st layer. In an alternative configuration where the ligaments are aligned in the same orientation, the open area fraction would be 1 since the 1st layer completely shadows the second area. This arrangement results in an upper bound estimate of the effective sputtering yield in terms of viewable sputtering area per layer. The 2nd layer open area fraction is seen to be identical to the 1st layer after neglecting terms of $\mathcal{O}(d^2/D^2)$. To confirm the uniformity of open area fraction for each sublayer using this configuration, the 3rd layer open area fraction is found to be

$$p^{(3)} = \frac{D^2 - (2dD - d^2) - (2dD - 3d^2)}{D^2 - (2dD - d^2)} = \frac{1 - \frac{4d}{D}}{1 - \frac{2d}{D}} \approx 1 - \frac{2d}{D}. \tag{7.6}$$

The 3rd layer is shown to have the same open area fraction as the previous layers which implies this pattern holds for all underlying layers given the prior assumptions. In particular, this approximation breaks down with additional layers depending on the specific ratio of d/D, which determines how fast the pore area is filed up by underlying ligaments. For many manufactured foams such as Duocel, the ratio is on the order of $d/D = 1/6$.

The above equations show that the open area fraction is independent of the layer considered and is identically

$$p^{(k)} = 1 - \frac{2d}{D} \tag{7.7}$$

which can be used to find the opacity

$$1 - p^{(k)} = \frac{2d}{D} \tag{7.8}$$

which is linearly proportional to the ratio d/D. Physically, the material opacity describes how much a layer's planar area is available for sputtering. In the plasma-facing regime ($\xi/\xi_c \ll 1$), the ions have open area fraction given by the previous derivation and do not see ligaments that are in the shadow of upper layers. However, in the plasma-infused regime

($\xi/\xi_c \gg 1$), the plasma is omnipresent in the foam and will sputter even shadowed ligaments such that the open area fraction for each layer is identical and independent of the specific arrangement of sublayer ligaments. The plasma-facing foam only has identical open area fractions if the expressions are approximated to 1st order and arranged to maximize the sputtering area. The effective sputtering yield for plasma-infused foams and plasma-facing foams will therefore be the same to 1st order, and otherwise larger for plasma-infused foams. The following section calculates the effective area of the sputtered ligaments for the opaque material regions.

7.1.2 Relative Area Factor

The relative area factor of a foam in plasma is dependent on the ratio of the plasma-infusion parameter to the critical parameter, ξ/ξ_c, which determines the regime of behavior. If $\xi/\xi_c \ll 1$, the ions in the plasma-facing foam will impact the circular cross-section of ligaments as shown in Figure 7.2a. Since the ions' velocities are parallel, they will impact the ligaments at various angles with an effective area of dD where D is the 3rd dimension perpendicular to the page. Here, the projected area is the same as the area for a sample with the same open area fraction but flat ligaments. The relative area factor f_A is therefore 1 since the area for the plasma-facing foam is identical to the flat surface base case.

Similar to the thin sheath approximation for Langmuir probes, plasma-infused foams with $\xi/\xi_c \gg 1$ have a thin plasma sheath formed parallel to each ligament surface as shown in Figure 7.2. Ions are accelerated through the plasma sheath and are normally incident on the local ligament surface producing an symmetric angular sputtering profile. The effective area is given by the surface area of a cylindrical ligament which is $2\pi(d/2)D$ which gives an area factor of $f_A = \pi dD/dD = \pi$. The relative area factor of a plasma-infused foam is therefore π or about 3 times larger than that for both plasma-facing foams and flat surfaces. The larger area factor enhances the sputtering yield for plasma-infused foams compared to plasma-facing foams.

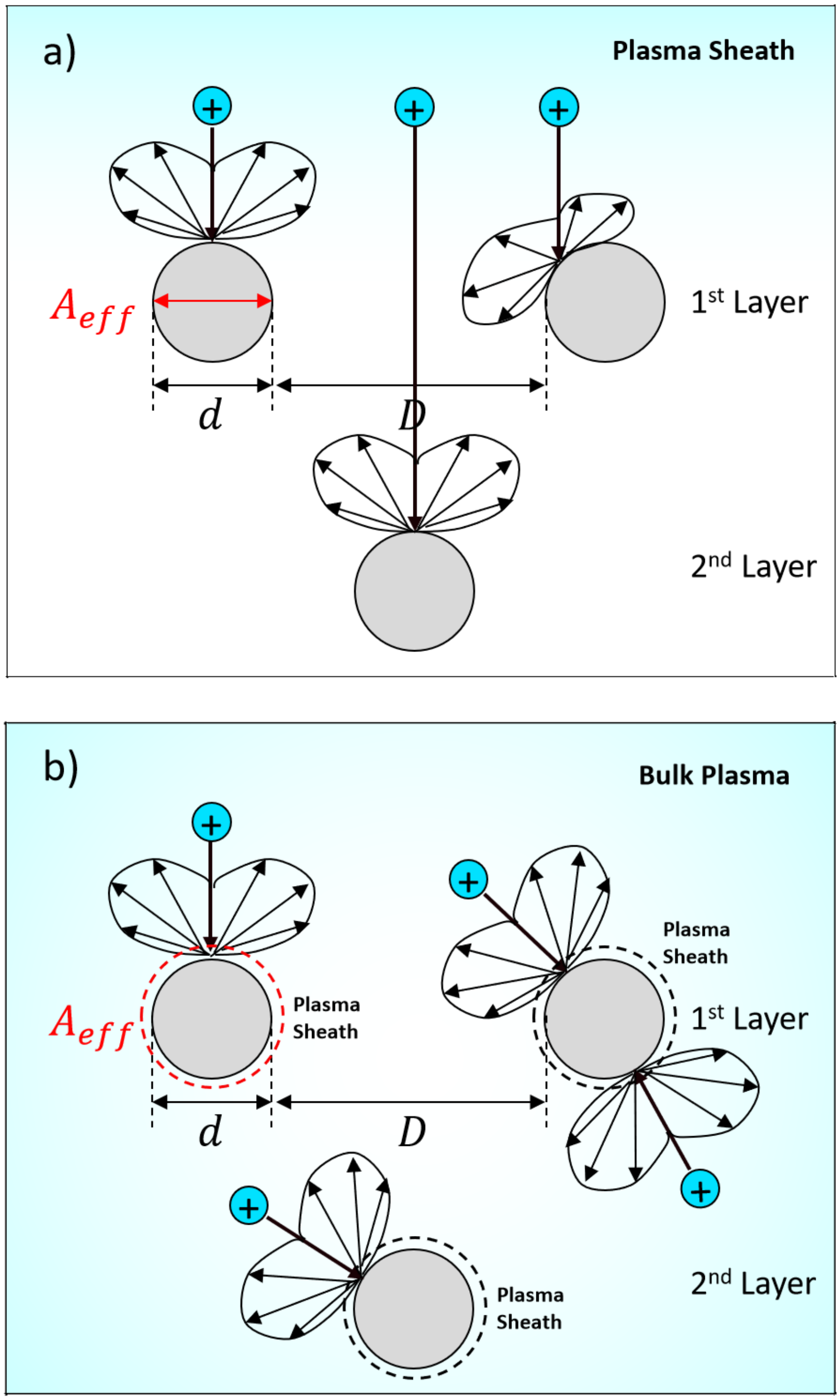

Figure 7.2: The effective sputtering areas and example angular sputtering profiles are shown for a) the plasma-facing regime and b) the plasma-infused regime.

7.1.3 Backsputter Factor

The effective sputtering area is defined as the fractional area per ligament cross section that can contribute to the effective sputtering yield measured for a given foam and is the product of f_A and f_β. The backsputter factor, f_β, dictates what fraction of that sputtered material is ejected back into the plasma and adds to the measured sputtering yield. Sputtered material that is ejected in the forward direction is assumed to remain in the foam. In order to calculate the backsputter factor, the angular sputtering profiles are needed for ions bombarding ligaments at oblique angles of incidence.

Equation 2.21 for the angular sputtering profile is repeated here:

$$\begin{aligned} S(E,\theta,\alpha) &= 0.042\frac{\alpha'(M_2/M_1,\theta)S_n(E)}{\pi U_s}\cos(\alpha) \\ &\times \left[1-\frac{1}{4}\left(\frac{E_{th}}{E}\right)\left\{\cos(\theta)\gamma(\alpha)+\frac{3}{2}\pi\sin(\theta)\sin(\alpha)\cos(\phi)\right\}\right] \end{aligned} \tag{7.9}$$

where

$$\begin{aligned} \gamma(\alpha) = \frac{3\,\sin(\alpha)^2-1}{\sin(\alpha)^2} \quad &+ \quad \frac{\cos(\alpha)^2(3\,\sin(\alpha)^2+1)}{2\,\sin(\alpha)^3}\times \\ &\ln\left[\frac{1+\sin(\alpha)}{1-\sin(\alpha)}\right] \end{aligned} \tag{7.10}$$

and E is the ion energy, θ and α are the ion incidence angle and sputtered particle ejection angle respectively, ϕ is the azimuthal ejection angle, and E_{th} is the sputtering threshold energy. The sputtering profiles are considered in the 2D plane of the incident ion with $\phi = 0$ for the left and $\phi = \pi$ for the right in Figure 7.3.

In Figure 7.3a, the plasma-facing regime has parallel ions accelerated by the sheath external to the foam impacting the ligament at oblique angles of incidence. The net backsputter

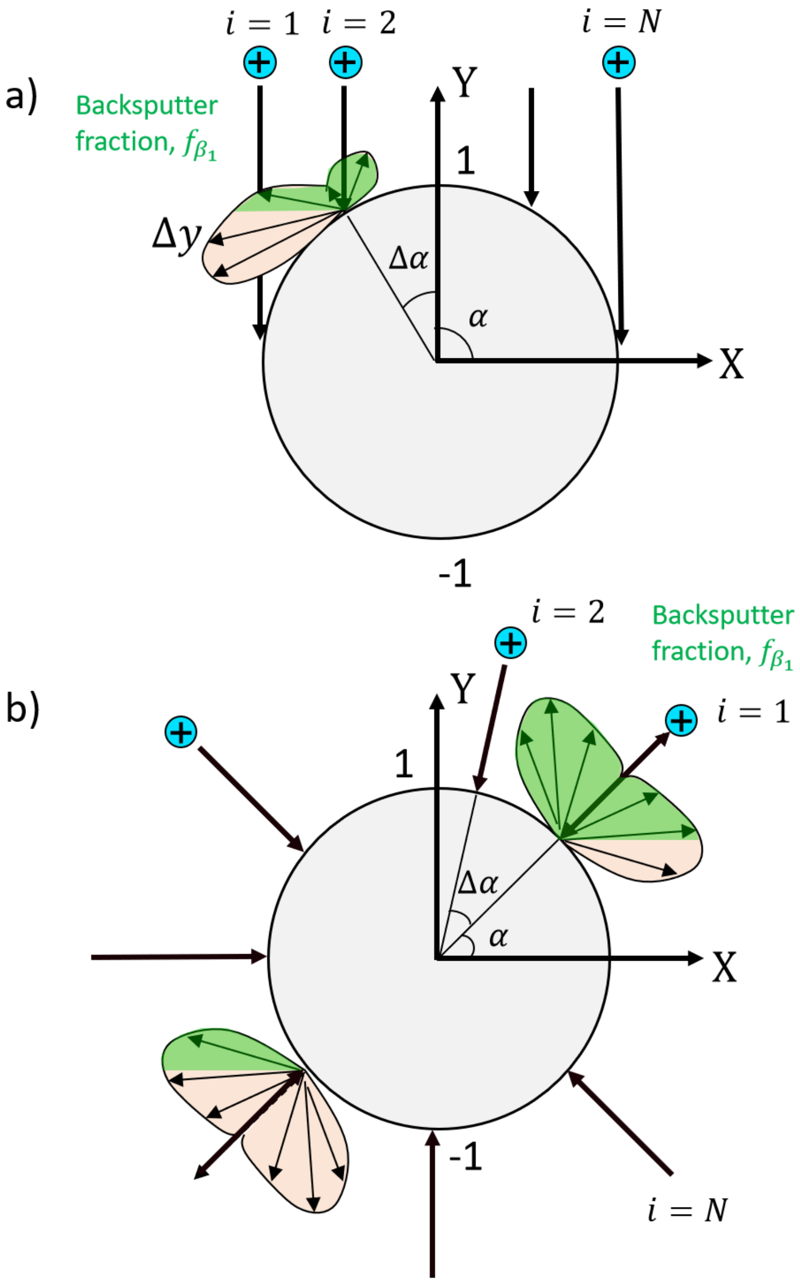

Figure 7.3: Diagrams for the backsputter fraction calculation are shown for a) the plasma-facing regime and b) the plasma-infused regime. The green filled area in the sputtering profiles show the fraction of backsputtered particles for a given ion impact. The angle α is defined counterclockwise from the x-axis.

factor is calculated by iterating through ions separated by equal increments in the vertical direction to simulate a uniform ion flux density at each ligament. The backsputter factor

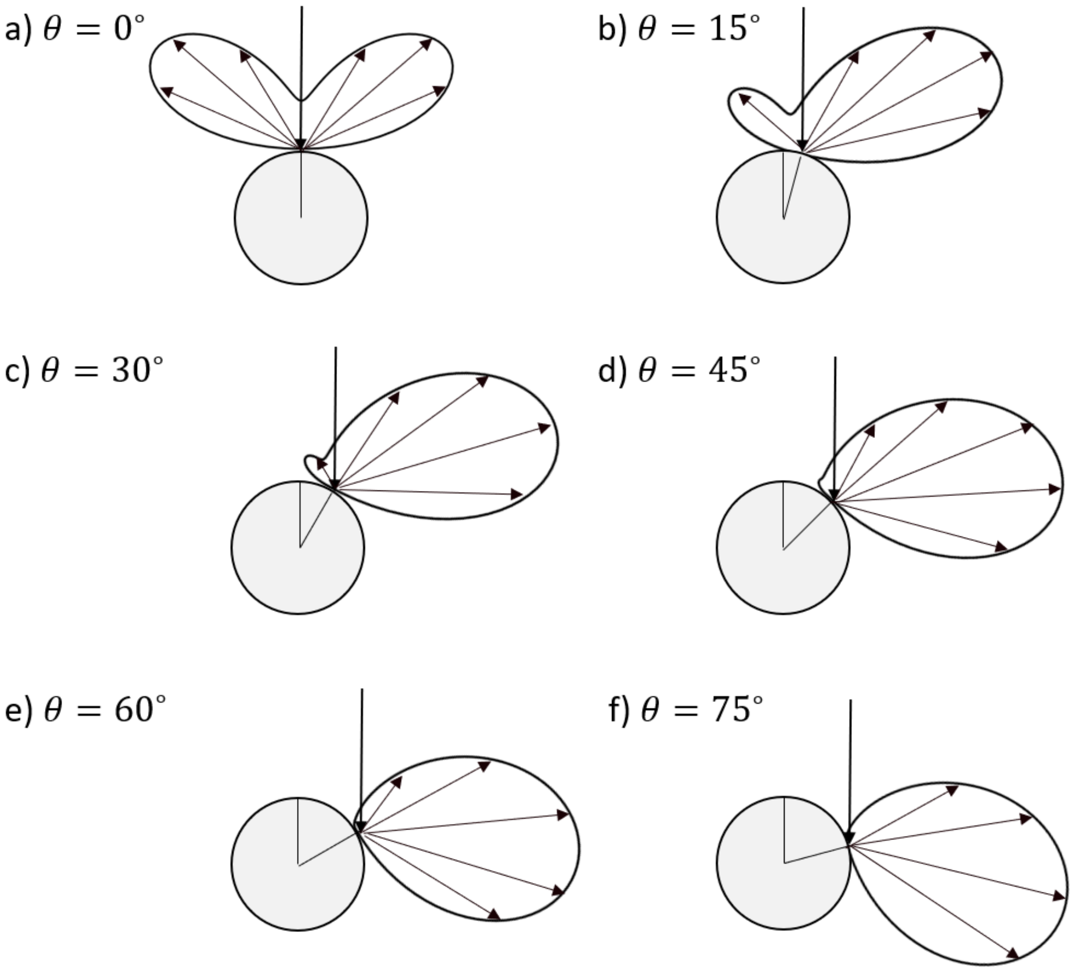

Figure 7.4: Angular sputtering profiles for an ion impacting a ligament at various angles of incidence. Profiles are calculated using Equation 7.9 with $E_{th} = 50$ eV for $\theta = 0°$ (normal incidence) to 75°.

is calculated for each ion, $f_{\beta,i}$, and the average value over all ion locations is found. The angular sputtering profile for a given ion impact is calculated via Equation 7.9 above and is a function of the incident ion energy.

It is important to note that the shape of the angular profile is dependent on the threshold energy chosen. Zhang and Zhang[49] report that the threshold energy is often used as a fitting parameter for angular sputtering data and the values are often not available for given ion-target combinations. A value of 50 eV was chosen for $Ar^+ \rightarrow Al$ following a similar profile for Ar^+ →Ni used by Huerta[25]. Moreover, the energy dependence in Equation 7.9 is derived from a semi-empirical model by Matsunami[110] that accounts for the behavior of the sputtering yield at low ion energies. While the total sputtering yield has been shown to fit yield data as a function of energy, the angular profiles have a significantly smaller pool of data for validation.

The plasma-infused regime is described in Figure 7.3b. The setup is similar to the normally incident ion case, but the ions are now locally perpendicular to the ligament at all locations. The ions are iterated from $\alpha = 0$ to $\alpha = 2\pi$ with the backsputter profiles calculated from Equation 7.9. For normal incidence ($\theta = 0$) Equation 7.9 simplifies to

$$S(E,\theta,\alpha) = 0.042\frac{\alpha'(M_2/M_1,\theta)S_n(E)}{\pi U_s}\cos(\alpha) \times \left[1 - \frac{1}{4}\left(\frac{E_{th}}{E}\right)\gamma(\alpha)\right] \tag{7.11}$$

where the profile is now independent of ϕ and is therefore symmetric with respect to the normal vector. A representative profile is shown in Figure 7.3b for two ion impact locations. The backsputter fraction is averaged over 1000 ion impacts and gives a net value of 0.5, indicating that half of the particles sputtered from a circular ligament in the plasma-infused regime will be ejected in the backwards direction ($-X$). Based on the symmetry of both the ligament and the angular sputtering profile, an equal probability of going left and right is physically intuitive. The result found for the plasma-infused case is found to be independent of ion energy and sputtering threshold energy.

7.1.3.1 Effects of Sputtering Yields at Oblique Incidence

The backsputter factor in Section 7.1.3 only includes the angular dependence in Equation 7.9 and neglects the weighted sputtering yield contribution of each ion due to oblique incidence. The following approach adds a weighting factor to each ion based on the sputtering yield at the oblique angle of incidence as discussed in Chapter 2. The averaged impact of the oblique sputtering yield on the backsputter factor can be calculated as

$$f'_\beta = f_\beta \times \frac{\bar{Y}_{\text{oblq}}}{Y_{\text{flat}}} \tag{7.12}$$

where $\bar{Y}_{\text{oblq}}$ is the oblique sputtering yield averaged over the ion impacts as a function of θ. The integration of the angular sputtering distribution in Equation 7.11 gives the semi-empirical total sputtering yield

$$Y(E,\theta) = 0.042\frac{\alpha(M_2/(M_1)S_n(E)}{U_s}\left[1 - \sqrt{\frac{E_{th}}{E}}\cos\theta\right]. \tag{7.13}$$

where the averaged yield can be found by integrating over the top hemisphere of the ligament in Figure 7.3 as

$$\bar{Y}_{\text{oblq}} = \frac{1}{y_1 - y_0}\int_{y_0}^{y_1} Y(E,\theta)dy. \tag{7.14}$$

The normalized oblique sputtering yield is therefore

$$\frac{\bar{Y}_{\text{oblq}}}{Y_{\text{flat}}} = \frac{1 - \frac{\pi}{4}\sqrt{\frac{E_{th}}{E}}}{1 - \sqrt{\frac{E_{th}}{E}}}. \tag{7.15}$$

Equation 7.15 can be used to investigate the effects of varying ion energy on the modified backsputter factor. However, Equation 7.13 has not been rigorously validated against experimental data and only the normally incident equation ($\theta = 0$) has been compared by Matsunami et al.[110]. Recently, authors have developed a range of empirical fits to sputtering yield data as a function of incidence angle as described in Chapter 2. A geometric sputtering model by Cassidy and Johnson[100] uses the approximation

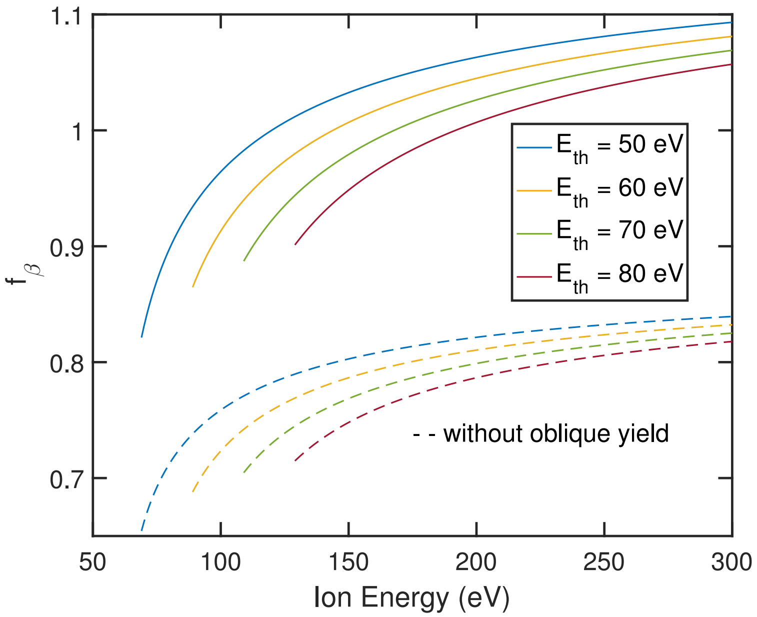

Figure 7.5: Backsputter factor calculated as a function of ion energy for various threshold energies.

$$\frac{Y_{\text{oblq}}(\theta)}{Y_{\text{flat}}} = \begin{cases} \cos^{-n}\theta & \text{if } \theta_i < \theta_c \\ 0 & \text{if } \theta_i > \theta_c \end{cases}$$

where the critical angle is where the sputtering yield drops to zero and n is typically between 0 and 2. The angular dependence is removed for $n = 1$ which corresponds to very low energy ions or rough surfaces where the angular variations are averaged out[100]. This approach leverages the well-known conclusion that the sputtering yield increases with incidence angle and then sharply drops to zero at some critical angle. Depending on the values of θ_c and n, the averaged oblique yield, $\bar{Y}_{\text{oblq}}/Y_{\text{flat}}$ can vary within an order of magnitude. Since the ion weighting term is a non-negligible effect, the Cassidy and Johnson approach is used with $\theta_c = 80^\circ$ and $n = 1$ for the current model as a modifier to the backsputter factor in Equation 7.12.

The backsputter factor for a plasma-facing foam is shown in Figure 7.5 as a function of ion energy. The plasma-infused case is not shown because it f_β is independent of energy due to the symmetry of ion bombardment on circular ligaments. The backsputter factor without the oblique sputtering yield modification is shown in dotted lines, and f_β with the included effect is shown in solid lines. The inclusion of the oblique sputtering yield appears to affect both the shape of the curve and the magnitude, showing that the oblique yield plays a major role in the energy dependence of the effective sputtering yield. Several curves for different sputtering threshold values are also plotted to illustrate the effects on the backsputter factor. The curves shift to higher energy as the threshold energy increases due to the change in where the sputtering yield drops to zero. Some angular profiles calculated closer to E_{th} using Equation 7.9 resulted in unphysical distributions (e.g. negative probabilities) and were omitted from the plot. The dominant mechanism here is the undercosine, i.e. butterfly shaped, angular sputtering distributions found near sputtering threshold energies. The peak of the sputtering profile shifts from the normal direction to an off-normal angle that allows a majority of sputtered particles to be ejected back into the plasma. The backsputtering factor for the plasma-facing foams can be used to calculated effective sputtering yields from Equation 7.1.

7.1.4 Ballistic Deposition

The ballistic deposition process is the primary means for reducing the effective yield via geometric structuring. In the cage geometry, the ligaments are the sputtering source and the backsputtered fraction of particles calculated previously is reduced due to intercepting ligaments. A simple iterative model is used here to estimate the ballistic deposition factor which captures this effect.

Figure 7.6 shows the simplified 2D cage geometry where the sputtering ligament is approximated as a point source. The ligaments are self-similar and only dependent on the ratio d/D. The angular sputtering distribution is approximated to be uniform with polar angle, θ_i, and the mean free path of sputterants is assumed to be much greater than the foam dimensions. The sticking coefficient is assumed to be unity for the self-deposition of

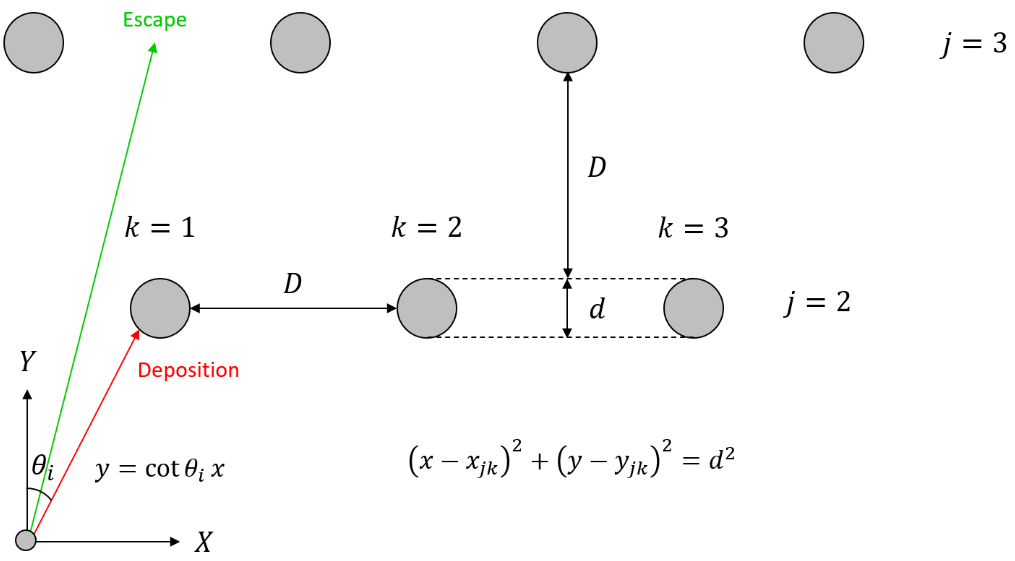

Figure 7.6: The schematic for the ballistic deposition model is shown with a point sputtering source at the origin and circular ligament cross-sections in 2D arrayed above. The ions are ejected uniformly at polar angles from 0 to $\pi/2$ and the fraction that intercepts ligaments is the ballistic deposition factor.

metals, although it should be noted that a non-unity sticking coefficient can lead to large differences in effective sputtering yield[100].

A numerical model iterates through N_S emitted sputtered particles, N_Y layers, and N_X ligaments per layer. The intersection of sputterant trajectories and ligament boundary equations is defined to be a deposition event. The solution for the intersection point is given by

$$x^{\pm}_{ijk} = \frac{(2x_{jk} + 2y_{jk}\cot\theta_i) \pm \sqrt{(2x_{jk} + 2y_{jk}\cot\theta_i)^2 - 4\csc^2\theta_i(x^2_{jk} + y^2_{jk} - d^2)}}{2\csc^2\theta_i} \tag{7.16}$$

$$y_{ijk} = x_{ijk}\cot\theta_i, \tag{7.17}$$

where a real solution is given for an deposition event and an imaginary solution is an escape event. The index $j = 2, ..., N_Y$ considers all layers preceding j for backsputtered deposition (e.g. $j = 1$ has $f_{\mathrm{dep}} = 0$ since it's the surface layer). A sufficient number of ions, ligaments, and layers is simulated for a convergent solution for an infinite foam medium. Practically, a limited number of ligaments and layers corresponding to real foam thickness or width can also be simulated.

The ballistic deposition factor is dependent on the ratio d/D which describes the self-similar nature of the ligament sputtering picture. Given the assumptions presented in Section 7.1.4, the ballistic deposition factor will be identical regardless of the exact length scale of the ligaments and pores as long as the ratio d/D is the same. Therefore, a microporous foam can have the same ballistic deposition factor as a millimeter pore size foam. The main differences arise when certain physical assumptions are violated such as the large ion range relative to ligament diameter at the nanometer scale particularly at thermal spike energies. The ballistic deposition model is used to iterate through several values of d/D as shown in Figure 7.7. The number of foam layers and ligaments are limited to 5 and 20 respectively while 100 ions are iterated through to illustrate representative deposition events.

The deposition processes are localized near the sputtering source and the sputtered particles are better contained by larger ligaments as can be seen for Figure 7.7a ($d/D = 1/4$) compared to 7.7d ($d/D = 1/10$). The larger ligaments subtend a larger angular radius relative to the sputtering source and therefore intercept more sputtered particles. Essentially, the ratio d/D as determined by the manufacturer plays a large role in the reduction of the effective sputtering yield. The 10 PPI and 40 PPI aluminum foams tested in Chapter 6 have $d/D \approx 1/6$. Even though the 40 PPI foam has four times the pore density, the ratio d/D is the same due to the same relative increase in ligament diameter. This simple model for the ballistic deposition process can be utilized to identify the correct dimensional scaling to the level required by the application.

Using the model, the ballistic deposition factors, f_{dep}, are calculated and plotted as a function of number of layers for varying d/D in Figure 7.8. $N_S = 1000$ particles and $N_X = 200$ ligaments were used to obtain converged results for an infinite foam medium. The

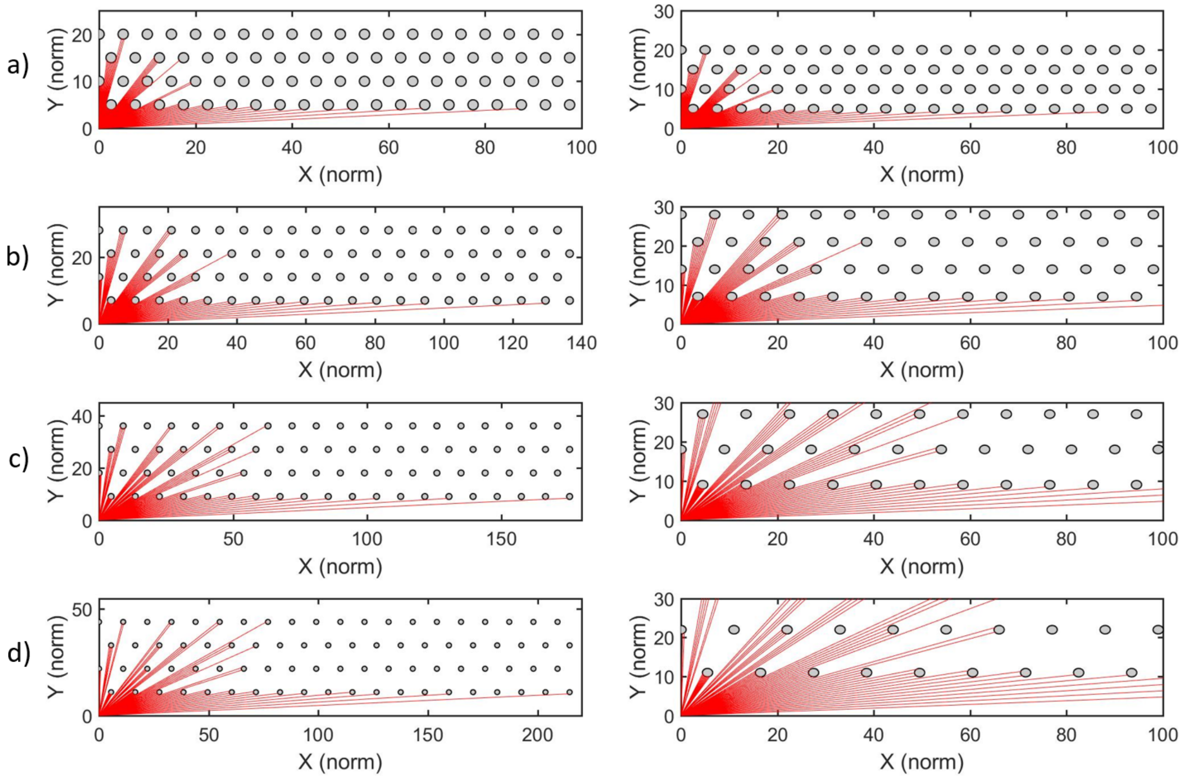

Figure 7.7: Ballistic deposition models are shown above for a) $d/D = 1/4$ b) $d/D = 1/6$ c) $d/D = 1/8$ and d) $d/D = 1/10$ with $N_S = 100$, $N_Y = 5$, and $N_X = 20$. The red lines are linear ion trajectories. The same plot is reproduced in the column to the right with fixed axes for a better comparison between plots.

simulation data in Figure 7.8 were found to be well fit by the empirical equation

$$f_{\text{dep}} = f_0 + \left[1 - \exp\left(\frac{-N_Y}{N'}\right)\right], \tag{7.18}$$

where N' and f_0 are fit parameters. The parameter N' represents an e-folding length describing the characteristic number of layers for near complete ballistic deposition of sputterants. Table 7.1 shows the N' value for each curve in Figure 7.8. As observed with the ballistic deposition ion trajectories, the thicker ligaments with smaller d/D approach complete deposition with fewer number of layers due to the large angular radius of each ligament. In a foam with fixed pore size, the ligaments can be made smaller until the desired ballistic deposition factor is achieved. Similarly, the model can be used to size the thickness of

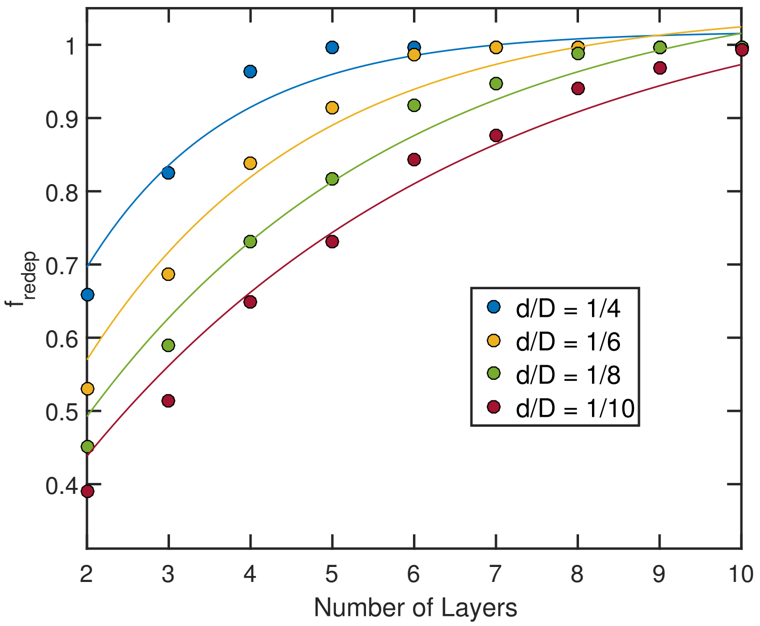

Figure 7.8: The deposition factor is shown as a function number of layers for varying ratios of d/D with $N_S = 1000$, $N_Y = 10$, and $N_X = 200$. An empirical equation is fit to each set of simulation results with fit parameters shown in Table 7.1.

foams in terms of the number of layers required for full ballistic deposition of sputterants. In general, foams with smaller d/D, or thin ligaments, will require a larger number of layers to achieve this effect.

d/D	N_S	N_Y	N_X	f_0	N'
1/4	1000	10	200	0.02	1.8
1/6	1000	10	200	0.05	2.7
1/8	1000	10	200	0.10	4.0
1/10	1000	10	200	0.10	4.8

Table 7.1: Model and fit parameters for Figure 7.8

7.1.5 Sputtering Yield Reduction Compared to Flat Surfaces

The reduction of the effective sputtering yield compared to a flat surface is a key metric for discerning the design efficiency of a foam material. The large parameter space of plasma and foam properties include the plasma-foam sputtering regime (i.e. plasma-facing to plasma-

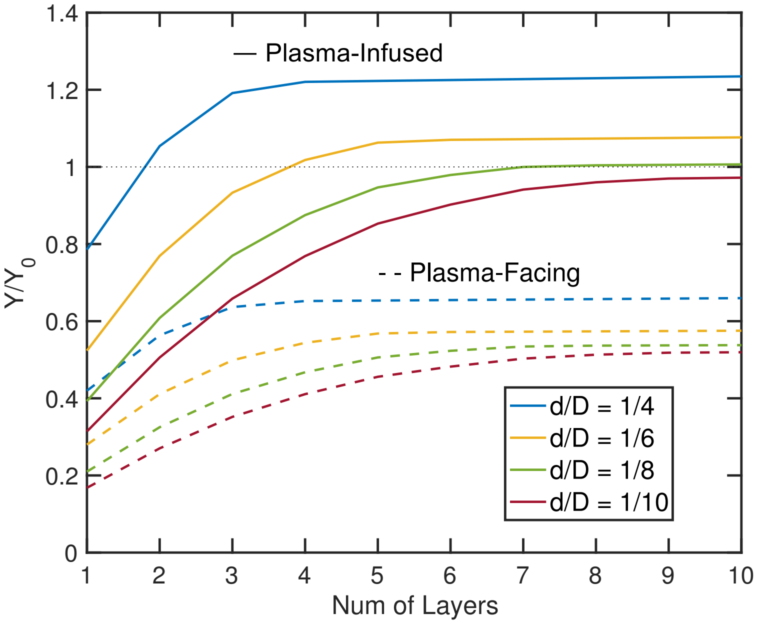

Figure 7.9: The normalized sputtering yield calculated for foams with various ligament-to-pore-diameter ratios are shown as a function of the number of layers for 300 V sheath voltage. The plasma-infused and plasma-facing cases are plotted in solid and dashed lines respectively.

infused), the number of layers, the ligament-to-pore-diameter ratio (d/D), and the ion energy. Based on the simplifications described in the previous sections, the analytical equation for the effective sputtering yield can be simplified to

$$\frac{Y_{\text{eff}}}{Y_{\text{flat}}} = \sum_{k=1}^{N} \frac{2d_k}{D_k} f_A^{(k)}(\xi) f_\beta^{(k)}(E,\xi) \left[1 - f_{\text{dep}}^{(k)}\left(\frac{d_k}{D_k}\right)\right]. \tag{7.19}$$

While the ratio d/D is non-dimensional, the absolute foam thickness depends on the number of layers and the pore diameter. By calculating the Debye length of a target plasma, the foam thickness can be determined based on the desired plasma-foam sputtering regime. For example, a plasma-infused foam can be defined as $\xi = D/\lambda_D = 10\xi_c$ if 10 times the critical parameter is deemed sufficient for full plasma infusion. Once the plasma conditions and sheath voltage have been fixed, the pore size can be calculated as $D = 10\xi_c\lambda_D$. Similarly, the plasma-facing regime can be achieved by setting $D = 1/10\xi_c\lambda_D$.

Finally, the absolute foam thickness is calculated by plotting the effective sputtering yield as a function of the number of layers to determine the desired yield reduction. Figure 7.9 shows the normalized sputtering yield from Equation 7.19 as a function of the number of layers for plasma-facing and plasma-infused foams with varying d/D ratios at a fixed sheath voltage of 300 V. For a given foam d/D, the plasma-infused foams have a larger yield due to the greater effective sputtering area term, $f_A f_\beta$, discussed previously. A fully plasma-infused foam may have a reduced or enhanced yield compared to a flat surface, while a transitional regime foam will likely have a reduced yield. On the other hand, the plasma-facing foam has a significantly reduced yield. As the number of layers increases, the yields for both plasma-foam sputtering regimes are seen to approach an asymptotic value as the increasing layers lead to full sputterant recapture due to ballistic deposition. Note that the approximation $d/D \ll 1$ was made for this simplified expression so the yield analysis may deviate as the number of layers increases. The ion energy dependence is discussed in Section 7.2.3.

Plasma-infused foams are defined to range from fully plasma-infused ($\xi/\xi_c \ll 1$) to the transitional regime $\xi/\xi_c \sim 1$ where foam sputtering carries aspects of both the plasma-facing and plasma-infused regimes. The quantitative analysis shown above implies that a fully plasma-infused foam will have the largest effective sputtering yield in a given plasma environment due to the effective sputtering area. The same foam placed into a low density plasma will have a lower sputtering yield. In general, a plasma-exposed foam is seen to have a reduced sputtering yield compared to a flat surface and the enhanced yield regimes (i.e. full plasma infusion) can be avoided by selecting the appropriate foam dimensions. By understanding the different design parameters in Equation 7.19, a foam can be designed for any given plasma environment. A computational model that relaxes many of the assumptions in this treatment will predict a more accurate value of the effective sputtering yield.

7.2 Model Results

The analytical model as derived is appropriate for foams in either limit of full plasma-infusion or plasma-facing, and can capture behavioral trends in the transitional regimes where characteristics from both regimes are present. The ideal experimental validation would be performed for each regime separately using a cage-structured material with cylindrical struts. The plasma-facing regime would involve an ion gun for the ion source which would be independent of any plasma properties. The plasma-infused foam would be tested with a steady dc plasma with no magnetic field and a cage with sufficiently large pores for full infusion. A single ligament, or rod, experiment similar to that of Byrne, Meyer, et al.[111, 112] which investigated the sputtering of a meshed reflector could benchmark specific behavior such as the backsputter factor or effective sputtering area. Ballistic deposition would require at least 2 layers of ligaments and also be studied with the appropriate experimental design. While a full validation of the model with a simplified experiment remains for future work, Equation 7.1 can be used to examine experimental trends by simplifying to the form

$$\frac{Y_{\text{eff}}}{Y_{\text{flat}}} = \sum_{k=1}^{N} \frac{2d_k}{D_k} f_A^{(k)}(\xi) f_\beta^{(k)}(E,\xi) \left[1 - f_{\text{dep}}^{(k)}\left(\frac{d_k}{D_k}\right)\right] f_{\nabla n}^{(k)} \tag{7.20}$$

where the key dependencies are the ligament-pore size ratio d/D, ion energy E, and plasma-infusion parameter ξ. The Pi facility plasma includes a 200 G centerline magnetic field with cusped field lines which is not included in the analysis. The ions are unmagnetized and the electrons are magnetized with gyroradii of 3.6 cm and 0.4 mm respectively. The background pressure in the chamber was $P \sim 10^{-4}$ Torr with 27 sccm of argon gas flow, giving a solid-sphere collisional mean free path of ~ 2500 m which is much larger than any characteristic lengths in the foam. The local neutral density is higher in the foam due to neutral influx from ion neutralization at the foam surfaces, but this is also neglected in the current analysis. The plasma density density gradient term, $f_{\nabla n}$, is only relevant for plasma-infused foams, $\xi > \xi_c$, since a plasma-facing foam has the ion flux fixed by the plasma conditions external

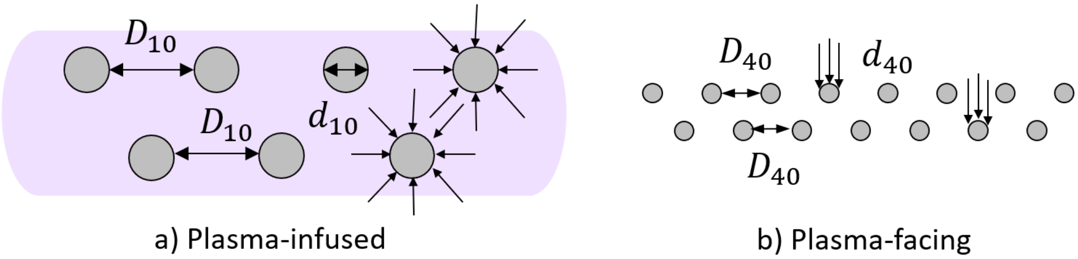

Figure 7.10: The 2-layer diagram shows the a) 10 PPI and b) 40 PPI foams in the plasma-infused and plasma-facing regimes respectively. The plasma is incident from the upwards direction.

to the foam. Generally, $f_{\nabla n}$ is taken to be unity since a self-consistent plasma-foam conservation model hasn't been implemented. Given these considerations, Equation 7.20 is used to analyze the observations and measurements made from the aluminum foam sputtering experiment presented in Chapter 6.

7.2.1 Case Study 1: Plasma-Infused vs. Plasma-Facing Yields

The first observation is that the effective sputtering yield for 10 PPI aluminum foam at 300 eV was initially larger than the 40 PPI foam with a value of 0.60 compared to 0.40. At first glance, the 10 PPI foam by definition has a lower pore density than the 40 PPI foam which may suggest a smaller area of material to sputter. However, two complicating factors are the increasing thickness of ligaments with lower pore density (PPI) and the effects of increased sputtering area with plasma-infusion of the foam. Equation 7.20 can be used to quantitatively assess the relative importance of different effects on the effective sputtering yield.

A 2-layer approximation is used based on the observation that the 2nd layer ligaments were largely uneroded in Figure 6.6. The ratio of ligament to pore diameter d/D is found to be approximately 1/6 based on calculated parameters and measurements. In the cage geometry, each cell has 6 pores with effective pore diameters which is assumed to approximate

Duocel foams which have 14 pores per cell. The calculated plasma-infusion parameters are $\xi_{10} = 48.3$ and $\xi_{40} = 12.1$ with a critical parameter of $\xi_c = 17.1$ at $\Delta\phi_s = 300$V, which give $\xi_{10}/\xi_c = 2.8$ and $\xi_{40}/\xi_c = 0.7$. The 10 PPI foam is seen to be plasma-infused while the 40 PPI is in the transitional regime. For the purpose of comparing the magnitude of the effective sputtering yields for the two foams, I assume the 10 PPI foam is fully plasma-infused ($\xi_{10}/\xi_c \gg 1$) and the 40 PPI foam is fully plasma-facing ($\xi_{40}/\xi_c \ll 1$) based on $\xi_{10} > \xi_{40}$. The goal is to assess whether the relatively more plasma-infused foam, 10 PPI, has a larger yield than the transitional foam, 40 PPI, as measured in the experiment.

Given the previous definitions, Equation 7.20 simplifies to

$$\frac{Y_{\text{eff}}}{Y_{\text{flat}}} = \underbrace{\frac{2d}{D} f_A(\xi) f_\beta(E,\xi)}_{\delta Y_1} + \underbrace{\frac{2d}{D} f_A(\xi) f_\beta(E,\xi) \left[1 - f_{\text{dep}}^{(2)}\left(\frac{d}{D}\right)\right]}_{\delta Y_2} \tag{7.21}$$

where δY_1 and δY_2 are the yield contributions from the 1st (top) and 2nd layers respectively. Figure 7.10 shows the 2-layer ligament orientation in 2D with the plasma-infused 10 PPI foam and plasma-facing 40 PPI foam. The ligament diameter, d, and pore diameter, D, are different for each foam, but the ratios d/D are the same since the two foams are self-similar by manufacturer design.

The effective sputtering area, $f_A f_\beta$, is equal to $0.5 \times \pi$ for the plasma-infused case as presented in Section 7.1.3. The plasma-facing case will have a fixed $f_A = 1$ but an ion energy-dependent f_β which is solved for numerically at a given ion energy E. For 300 eV ions, $f_\beta = 1.09$ which includes the effect of oblique sputtering yields. The deposition factor for the 2nd layer is numerically calculated to be $f_{\text{dep}}^{(2)} = 0.53$ using the code described in Section 7.1.4.

The calculated yield contributions from the 1st and 2nd layers for the 10 PPI and 40 PPI foams are shown in Table 7.2. The total yield for the plasma-infused 10 PPI is almost double the plasma-facing 40 PPI foam. Since the foams are self-similar ($d/D = 1/6$), the

Case	d/D	f_A	f_β	$f_{\text{dep}}^{(2)}$	δY_1	δY_2	$Y_{\text{eff}}/Y_{\text{flat}}$
Plasma-infused	1/6	π	0.5	0.53	0.52	0.25	0.77
Plasma-facing	1/6	1	1.09	0.53	0.28	0.13	0.41

Table 7.2: Effective sputtering yield calculations for plasma-infused (10 PPI) and plasma-facing (40 PPI) aluminum foams.

primary reason for the increased yield is due to the effective sputtering area

$$\frac{f_A(10\text{ PPI})f_\beta(10\text{ PPI})}{f_A(40\text{ PPI})f_\beta(40\text{ PPI})} = 1.9 \tag{7.22}$$

which corresponds to full plasma-infusion for the 10 PPI foam and plasma-facing behavior for the 40 PPI foam. The plasma-infused and plasma-facing scenarios define upper and lower bounds for the yield as these cases represent the extreme limits of effective sputtering area. Since $\xi/\xi_c \sim 1$ for both foams, the transitional regime implies both foams only have partial characteristics from both regimes, but $\xi_{10} > \xi_{40}$ so a relative comparison can be made by examining the limits. Therefore, the 10 PPI foam can be said to have a larger yield due to having an increased effective sputtering area from more plasma infusion. Since the 2nd layer was seen to be scarcely eroded, the plasma-infusion effect was most likely limited to the 1st layer. The separate yield contributions for each layer show that the 1st layer is the dominant contribution to the total yield because sublayer contributions are reduced due to ballistic deposition. The lowest possible yield would be obtained with a single layer "foam" or mesh with no ballistic deposition. However, most applications require a material of finite thickness for structural integrity so a stacked matrix of layers which replaces a solid material for a reduced yield. In summary, it can be concluded that foams with more plasma infusion will have a larger yield due to increased effective sputtering area.

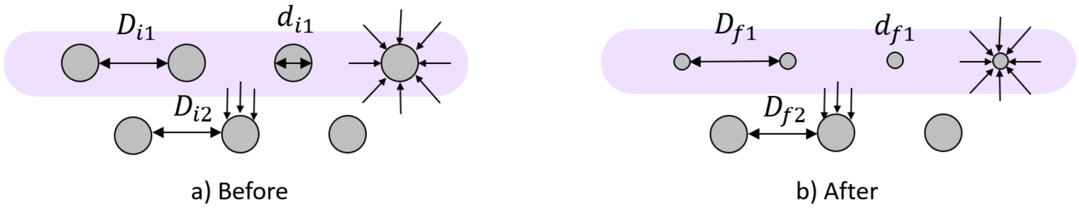

Figure 7.11: The 2-layer diagram shows the 10 PPI foam a) before and b) after plasma exposure with the thinning ligaments reflected in the changing 1st layer variables. The 1st layer is treated as plasma infused and the 2nd layer is plasma-facing with the plasma incident from the top.

7.2.2 Case Study 2: Thinning Ligaments

The ligaments for the 10 PPI foam were found to decrease in thickness as shown in the before and after SEM images shown in Figure 6.6. The corresponding sputtering yields at 300 eV decreased from 0.60 to 0.45 at the end of the 30 h exposure. An intuitive explanation would be that the yield decreases as there is fewer material to sputter as the 1st layer ligaments become thinner. However, the thinner 1st layer also serves to decrease the ballistic deposition factor from the 2nd layer, allowing more sputterants to escape the foam. Here, the goal is to use Equation 7.20 to determine quantitatively which effect is dominant and whether there are alternative explanations to the observation of thinning ligaments.

Similar to the previous section, the 2-layer approximation is used here to represent the 10 PPI before and after plasma exposure as shown in Figure 7.11. To more adequately represent the transitional regime behavior ($\xi_{10}/\xi_c \sim 1$), the 1st layer is treated as plasma-infused while the 2nd layer is plasma-facing. The true physical picture would require a computational model to investigate 2D sheath effects where the presheath would play a major role in the ion accelerating structure. However, for the purpose of this analysis, the hybrid assumption of plasma-infused/plasma-facing layers is used. The initial pore diameter, $D_{i1} = D_{i2} = 2540$ μm, was calculated using an approximated Duocel formula $D = 1/PPI$ and the initial ligament diameter, $d_{i1} = 364$ μm was measured using the SEM image from Figure 6.6. The final ligament diameter, $d_{f1} = 94$ μm, was also measured to find the change

Case	d_1/D_1	d_2/D_2	$f_A^{(1)}$	$f_A^{(2)}$	$f_\beta^{(1)}$	$f_\beta^{(1)}$	$f_{\text{dep}}^{(2)}$	δY_1	δY_2	$Y_{\text{eff}}/Y_{\text{flat}}$
Before	0.14	0.14	π	1	0.5	1.09	0.49	0.45	0.16	0.61
After	0.03	0.14	π	1	0.5	1.09	0.18	0.10	0.20	0.30

Table 7.3: Effective sputtering yield calculations for the 10 PPI foam before and after plasma exposure.

$\Delta d = 270$ μm and the corresponding final pore diameter, $D_{f1} = D_{i1} + \Delta d = 2810$ μm. The resulting ratios d/D for each layer are shown in Table 7.3.

The effective sputtering area at 300 eV is identical to the plasma-infused and plasma-facing parameters provided in Table 7.2 from Case 1. Other than the varying dimensions, d and D, which are used to calculate a new deposition factor, the assumptions for the analysis remain the same. The resulting effective sputtering yields are shown in Table 7.3. The first major observation is that the sputtering yield does indeed decrease after plasma exposure from 0.61 to 0.30, similar to the experimental result of 0.60 dropping to 0.45. The decrease can be traced down to the contributions from the two layers before and after plasma exposure. The first layer ratio d_1/D_2 is seen to drop from 0.14 to 0.03 which results in a drop in deposition factor from 0.49 to 0.18. The material opacity, or fraction of a planar layer occupied by material, is linearly proportional to the ratio d/D so the decrease in yield from the 1st layer, δY_1 drops linearly as well from 0.45 to 0.10. The reduced material opacity results in larger open area fraction for 2nd layer sputterants to escape so the 2nd layer contribution increases from 0.16 to 0.20. However, the increase in δY_2 is much smaller than the decrease in δY_1, resulting in an overall decrease in sputtering yield. Therefore, the model agrees with the experimental observation that sputtering yield decreases due to thinning ligaments in the top layer. In addition, the model has shown that the decrease in yield is due to the reduced material opacity dominating over the increase in escaped 2nd layer sputterants. The interdependency of the material opacity and ballistic deposition factor will always result in a lower sputtering yield for thinning ligaments given that the effective sputtering area remains constant.

7.2.3 Case Study 3: Low Energy Yield Dependence

The sputtering yield measurements in Chapter 6 revealed a low energy dependence with the yield decreasing by as much as 80% at a 100 V sample bias. The energy-dependent measurements were performed before and after plasma exposure and showed the same trend. For low energy ion sputtering, the angular sputtering distribution at normal incidence is known to transform from a cosine profile to a butterfly shaped distribution. Similarly, the angular profile for oblique incidence is sensitive to the angle of incidence. For a review of angular sputtering profiles, see Chapter 2. The angle of incidence is an ion-material property and is independent of the plasma interface. However, the plasma sheath thickness is dependent on the sheath voltage which accelerates the plasma ions, with larger voltages increasing the sheath thickness. Furthermore, a plasma-infused foam can have a plasma density gradient which may be sheath voltage dependent and can reduce the ion flux at a given distance into the foam. The goal of these case study is to investigate the dependence of the sputtering yield on the sheath voltage, which is assumed to be equivalent to the ion energy.

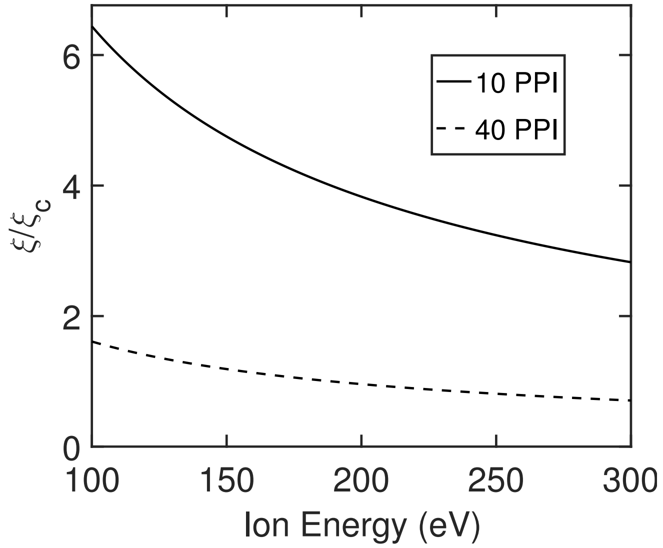

Figure 7.12: The plasma-infusion parameter for aluminum foams in the Pi plasma as a function of ion energy (i.e. sheath voltage).

In Equation 7.20, the energy dependence manifests in the backsputter factor, f_β, for plasma-facing foams and the plasma-infusion criterion, $\xi_c(\Delta\phi_s)$. The simplified equation using the 2-layer approximation including the plasma density gradient term is shown below.

$$\frac{Y_{\text{eff}}}{Y_{\text{flat}}} = \frac{2d}{D}\underbrace{f_A(\xi)f_\beta(E,\xi)}_{f(E)} + \frac{2d}{D}\underbrace{f_A(\xi)f_\beta(E,\xi)}_{f(E)}\left[1 - f_{\text{dep}}^{(2)}\left(\frac{d}{D}\right)\right]\underbrace{f_{\nabla n_e}^{(2)}(E)}_{f(E)} \tag{7.23}$$

The plasma-infusion parameter determines the plasma-foam sputtering behavior based on the energy-dependent plasma-infusion criterion, ξ_c. Here, the Child-Langmuir sheath thickness is related to ξ_c by $\xi_c = L_s/\lambda_D = \sqrt{2}/3(2e\Delta\phi_s/T_e)^{3/4}$. The sheath thickness, L_s, increases with sheath voltage, $\Delta\phi_s$, where it is assumed that ions are born at the plasma potential of 0 V. Assuming ions are not generated at lower potentials, i.e. through double sheaths in the foam, the ion energy will be equivalent to the sheath voltage, $E = \Delta\phi_s$. Figure 7.12 plots the ratio ξ/ξ_c as a function of ion energy for the 10 PPI and 40 PPI foams. The general trend is an increase in ξ/ξ_c with lower ion energies. As the ratio increases, the foam becomes more plasma-infused.

The effective sputtering area, $f_A f_\beta$, depends on both the plasma-infusion parameter and the ion energy. In Section 7.1.3, the fully plasma-infused case ($\xi/\xi_c \gg 1$) was shown to be independent of energy. As long as the sheath thickness is much less than the pore size, the symmetry of fully plasma-infused sputtering removes ion energy dependent effects. The plasma-facing foam ($\xi/\xi_c \ll 1$) will experience varying angles of incidence for ions impacting the ligament at different vertical locations. Therefore, the backsputter fraction, f_β will be strongly dependent on the angular sputtering profile, $S(E,\theta,\alpha)$ used. Recall, the angular profile by Zhang and Zhang[49] used in the current model is

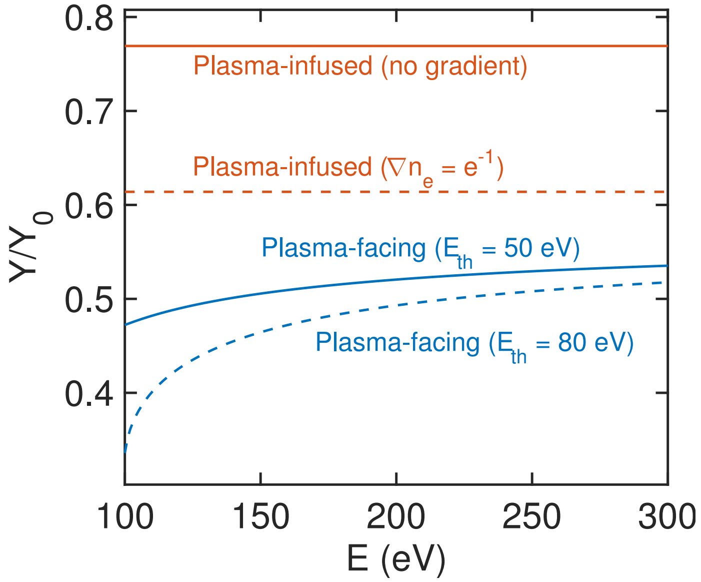

Figure 7.13: The effective sputtering yield is calculated for the plasma-facing case with two different E_{th} values and the plasma-infused case with and without a plasma density gradient where $n_e^{(2)} = (1/e)n_e^{(1)}$.

$$\begin{aligned} S(E,\theta,\alpha) &= 0.042\frac{\alpha'(M_2/M_1,\theta)S_n(E)}{\pi U_s}\cos(\alpha) \\ &\times \left[1-\frac{1}{4}\left(\frac{E_{th}}{E}\right)\left\{\cos(\theta)\gamma(\alpha)+\frac{3}{2}\pi\sin(\theta)\sin(\alpha)\cos(\phi)\right\}\right] \end{aligned} \tag{7.24}$$

In addition to the ion energy dependence, the threshold energy, E_{th}, plays a major role in modifying the sputtering profile. In general, the sputtering threshold has been used as an experimental fit parameter for angular sputtering data. However, the threshold is known to depend on the angle of incidence as well due to interdependency of the surface penetration depth and the projected ion velocity relative to the surface normal. Due to the lack of consensus on threshold energies, this dissertation has used $E_{th} = 50$ eV as an approximate fit value for similar sputtering data[25].

Figure 7.13 shows the sputtering yield for four different cases. The plasma-facing case shows the energy dependence from the backsputter factor which comes from the angular sputtering profile. The model is run for two different threshold energies, $E_{th} = 50$ eV, which is used for all the case studies presented in this dissertation, and $E_{th} = 80$ eV, which demonstrates the sensitivity of the yield on the threshold energy. The general trend is similar with the yield decreasing at lower energies, in agreement with the experimental observation. However, the rate of decrease is highly dependent on the threshold energy with the yield dropping to zero faster with higher E_{th}. Theoretically, the threshold energy is the critical point where the sputtering yield decreases to zero. In Equation 7.24, the angular profile changes shape with varying E_{th} and the effects cascade through to the sputtering yield as expected. Therefore, the large reduction in yield at low energies measured in the experiment is successfully reproduced by by a plasma-facing foam with a high threshold energy.

Based on the plasma-infusion parameters in Figure 7.12, both foams should be near the transitional regime with partially plasma-infused behavior. The plasma-facing aspect will introduce the low energy dependence, however, the increase in ξ/ξ_c with lower energy should increase the sputtering yield due to higher sputtering area. The increased yield from the sputtering area may compete with the backsputter factor dependence with the plasma-facing behavior dominating in the yield curve. Another explanation may be due to a plasma-density gradient in the plasma-infused regime. Equation 7.11 allows for a plasma gradient modification term in the 2nd layer which effectively acts as an ion flux reduction term. In Figure 7.13, the plasma-infused yield is plotted with no gradient and with a gradient equal to $\nabla n_e = e^{-1}$ such that $n_e^{(2)} = (1/e)n_e^{(1)}$. The fully plasma-infused yield is seen to decrease by 0.15 due to the addition of a negative plasma density gradient into the foam. In summary, the backsputter fraction and the plasma density gradient for plasma-infused foams have both been identified as possible contributors to the low energy reduction in the foam sputtering yield. A more sophisticated model is required to examine transitional regime behavior where the plasma-foam sputtering takes on both plasma-facing and plasma-infused effects.

7.3 Summary

An analytical model for the effective sputtering yield of a plasma-exposed foam has been presented. The key physical phenomena captured in the simple equation are the material opacity, effective sputtering area, ballistic deposition, and plasma density gradients. Based on the plasma-foam sputtering behavior determined by a plasma-infusion parameter, the effective sputtering yield can be calculated and compared to experimental data and analyzed to determine physical trends. The model was used to analyze three experimental observations from Chapter 6. Foams with higher plasma-infusion characteristics are shown to have a larger sputtering yield due to an increased effective sputtering area. Furthermore, fully plasma-infused foams will define an upper bound to the yield while plasma-facing foams define a lower bound. The thinning ligaments observed in the 10 PPI foam experiment were shown produce smaller sputtering yield due a linear decrease in material opacity dominating over an increase in escaped sputterants from sublayers. Finally, the higher reduction in yield at low ion energies was shown to be due to the particular angular sputtering profiles near the sputtering threshold. In addition, fully plasma-infused foams which are ion energy-independent are hypothesized to have a yield reduction due to plasma density gradients into the foam. The general trends in the experiment have been successfully validated, and more detailed investigations into phenomena such as the presence of density gradients or transitional regime behavior are left for future work.

CHAPTER 8

Conclusions and Future Work

8.1 Conclusions

This dissertation has presented novel results for the plasma sputtering behavior of structured materials. The time-dependent sputtering yield of a micro-featured surface was measured for the first time, showing that the yield was initially reduced compared to a flat surface but eventually approached the flat value as the surface features were eroded away. The transient yield proved that a volumetrically structured material, such as a foam, was necessary for a persistent reduction in sputtering yield.

The sputtering yields for two aluminum microfoams were found to be consistently reduced by 40 – 80% for a 30 h plasma exposure, demonstrating for the first time that a foam can persistently maintain a reduced yield as layers are sputtered away. Furthermore, the reduction in yield was found to be more pronounced at low energies, reaching a maximum reduction of 80% at 100 eV. Analytical modeling revealed that the low energy dependence is due to the angular sputtering profiles leading to more efficient geometric recapture of sputterants. The overall reduction in yield was shown to be dominated by geometric effects, angular sputtering distributions, and negative plasma density gradients in the foam.

An open-cell foam in a plasma has two fundamental regimes that characterize the sputtering behavior: the plasma-facing regime and the plasma-infused regime. The two regimes are defined by the plasma-infusion parameter, ξ, that relates the pore size of the foam to the plasma sheath thickness. Traditional plasma sputtering experiments will achieve ion acceleration through a thick sheath that forms external to the macroscopic surface. However, sheaths that are much smaller than the pore size will allow plasma to infuse the material volume. A plasma-infused material alters the long-standing notion that the plasma sheath forms external to the surface and modifies the plasma-surface interactions from superficial to volumetric phenomena.

Fundamentally, plasma infusion is a process that can be generalized to any open material given the right plasma background conditions. The development of advanced manufacturing processes will allow materials of many open geometries, including but not limited to foams, to be investigated. Although plasma infusion leads to a larger effective sputtering area, geometric recapture facilitates an overall reduction in sputtering yield. The unique characteristics of reduced sputtering yield and volumetric plasma-surface interactions motivates the categorization of plasma-infused materials as a new metamaterial. As a wall material, plasma-infused materials can influence future applications that encounter intense plasma environments such as nuclear fusion reactors and high-power electric propulsion. Ultimately, each plasma application can have a corresponding plasma-infused material design tailored for desirable performance and lifetime.

8.2 Future Work

The present work has provided a preliminary investigation into the plasma sputtering behavior of structured materials and more specifically foams. The sputtering yield of foams has been found to be persistently reduced compared to flat materials and there appears to be a strong dependence on the plasma conditions. While the initial results are promising, there remains many questions left unanswered. The following list provides suggestions for future work.

1. **Sputtering Behavior** – The experiments and analysis in this dissertation have provided sputtering yield measurements for two aluminum foams with 10 PPI and 40

PPI pore density. There remain many more parametric studies to be performed including varying pore density, ion species, foam elemental composition, and ion energy (electrical bias).

- **Pore Density** – Available pore densities range from 100 PPI to 5 PPI from industry providers based on manufacturing limitations. Over time, a larger range of pore densities will be available, allowing a more detailed study of plasma-infusion parameters. The present experiments involved foams in the transitional regime of plasma-infusion. Foams with significantly smaller or larger pores will allow for investigations of fully plasma-facing ($\xi/\xi_c \ll 1$) and plasma-infused foams ($\xi/\xi_c \gg 1$). Results in the two limits of plasma-infusion will provide better validation of the analytical model introduced in Chapter 5.
- **Elemental Composition** – The ion-atom combination can also be varied with different plasma species and foam elemental compositions. The Pi facility is capable of using helium, argon, xenon, and other noble gases for its $\mathrm{LaB_6}$ hollow cathode. The foam composition is limited by manufacturer capabilities. Duocel foams are limited to aluminum, carbon, copper, and silicon carbide materials, while competitors such as Ultramet Inc. use chemical vapor deposition to deposit a larger variety of surface coated elements onto a carbon foam substrate.
- **Ion Energy** – Finally, the ion energy which is achieved by means of an electrical bias can be studied in further detail. Below 100 V, the measured sputtering rate is close to the detection threshold of the Pi facility quartz crystal microbalance. The foam also floats at roughly 40 V below ground potential setting a lower limit at 40 eV ions which is near the sputtering threshold energy for most materials. For the higher limit, the foam bias voltage is limited by high voltage arcing, whether from sharp corners or adjacent materials. At present, there is a major shortage of foam sputtering data in the literature and any additional experiments will provide novel and insightful data to the community.

2. **Computational Modeling** – The analytical model presented in Chapter 7 provided an initial look into the physical mechanisms present in plasma-foam sputtering. The effects included in the model are material opacity, effective sputtering area, ballistic deposition, and plasma density gradients. While material opacity and ballistic deposition are a function of the foam geometry, the effective sputtering area and plasma density gradients were identified to depend on the plasma-foam sputtering regime. The sputtering behavior was defined for the limits of plasma-facing ($\xi/\xi_c \ll 1$) and plasma-infused foams ($\xi/\xi_c \gg 1$) but the transitional behavior where ($\xi/\xi_c \sim 1$) requires 2D effects and relaxing assumptions.

    - **Multidimensional Sheath Effects** – The sheath was assumed to be planar (1D) for both plasma-facing and plasma-infused foams. Here, the ion is accelerated perpendicular to sheath, either external to the foam or locally normal to each ligament. The simplified behavior is appropriate for each extreme case, but the transitional regime behavior will involve multidimensional (at least 2D) sheaths and ions with angular momentum similar to orbital ion motion in probes. Similar analysis has been performed for the plasma molding effect in ion optics systems by Kim and Economou[104, 105]. Their studies revealed non-uniform ion flux densities and energy distributions for ions affected by the 2D sheath in a transitional regime. The present model assumes uniform flux densities and monoenergetic ions. To investigate further, the 2D sheath must be extended from the top layer as in the plasma molding scenario to the interior volume of the foam to represent a volumetric plasma-infusion scenario. A 2D computational model with sheath effects will reveal variations in ion impact conditions on ligaments as a function of density, incidence angle, and energy distributions.

    - **Plasma Transport** – The organization of open-cell foams as individual cells with pore boundaries lends itself well to a finite volume transport model for plasma and neutral species. Current unknowns include the plasma density, neutral density, and sheath potential profiles. In general, plasma is transported from the bulk plasma external to the foam. Depending on the neutral density, there may be an ion generation rate within the foam as well. In addition, the neutral density will affect the sheath in the form of collisional effects. The plasma potential is unlikely to be identical to the bulk plasma potential which is near ground for the Pi plasma system. The existence of a potential gradient will be influenced by double sheaths, pre-sheaths, and magnetic fields. Since sputtering is dominated by the ion energy and incidence angle, the origin of ions will set the net acceleration potential and the directionality of ions will determine if local oblique sputtering yields on ligaments are necessary. Based on the ion incidence conditions, the resulting sputterant distribution can be determined and potentially controlled to limit the escape of sputterants into the bulk plasma.

Appendix A

Sputtering Yield Formulations

In this Appendix, the improved sputtering equations by Yamamura, Matsunami, Bohdansky, and others is presented. The original Sigmund solution for normal incidence is shown to be:

$$Y(E) = \frac{0.042}{U_s} \alpha \left(\frac{M_2}{M_1} \right) S_n(E), \tag{A.1}$$

where U_s is the sublimation energy, α is a fit parameter based on the ion-target mass ratio, and $S_n(E)$ is the nuclear stopping cross section. The parameter, α, is approximated to be

$$\alpha = 0.15 + 0.13 \left(\frac{M_2}{M_1} \right) \tag{A.2}$$

based on a linear fit to measurements[113]. The nuclear stopping cross section was derived analytically by Lindhard[114] using the Thomas-Fermi treatment:

$$S_n(E) = 4\pi Z_1 Z_2 e^2 a \left(\frac{M_1}{M_1 + M_2} \right) s_n(\epsilon), \tag{A.3}$$

where M_1, Z_1 and M_2, Z_2 are the masses and atomic numbers of the incident ion and target atom respectively, $s_n(\epsilon)$ is the reduced elastic cross section, a is the screened radius, and ϵ is the reduced energy. The screened radius, a, and reduced energy, ϵ, are defined as

$$
\begin{aligned}
a &= 0.8853a_0(Z_1^{2/3} + Z_2^{2/3})^{-1/2}, && \text{(A.4)}\\
\epsilon &= \frac{a}{Z_1 Z_2 e^2}\left(\frac{M_2}{M_1 + M_2}\right)E, && \text{(A.5)}
\end{aligned}
$$

where a_0 is the Bohr radius. An analytical expression for the reduced elastic cross section, $s_n(\epsilon)$ is given by Matsunami et al.[45] to be

$$
s_n(\epsilon) = \frac{3.441\sqrt{\epsilon}\,\ln(\epsilon + 2.718)}{1 + 6.355\sqrt{\epsilon} + \epsilon(-1.708 + 6.882\sqrt{\epsilon})}. \tag{A.6}
$$

The Sigmund formula above is valid for collisions in the linear cascade regime, but may not apply for the single knock-on regime closer to the sputtering threshold. However, the general derivation performed by Sigmund is flexible and several semi-empirical adaptations have been implemented for better agreement with experimental data.

Matsunami et al.[45] adapted the Sigmund formula to include the effects of the threshold energy as

$$
Y(E) = \frac{0.042}{U_s}\alpha\left(\frac{M_2}{M_1}\right)S_n(E)\left(1 - \sqrt{\frac{E_{th}}{E}}\right), \tag{A.7}
$$

where E_{th} is the sputtering threshold energy. Yamamura et al.[115, 116, 20] further modified the equation to obtain the third Matsunami formula which takes into account electronic stopping and the effect of the target material on the mass-ratio dependence:

$$
Y(E) = 0.042\frac{Q(Z_2)\alpha^*(M_2/M_1)}{U_s}\frac{S_n(E)}{1 + \Gamma k_e \epsilon^{0.3}}\left(1 - \sqrt{\frac{E_{th}}{E}}\right)^s, \tag{A.8}
$$

where W, Q, and s are dimensionless parameters dependent on the atomic number of the surface atom, k_e is the Lindhard electronic stopping coefficient, and Γ and α^* are dimensionless factors that depend on the ion-target combination. The Γ factor is given by

$$\Gamma = \frac{W(Z_2)}{1 + (M_1/7)^3} \tag{A.9}$$

and k_e is defined by

$$k_e = 0.079 \frac{(M_1 + M_2)^{3/2}}{M_1^{3/2} M_2^{1/2}} \frac{Z_1^{2/3} Z_2^{1/2}}{(Z_1^{2/3} + Z_2^{2/3})^{3/4}}. \tag{A.10}$$

The best-fit values for α^* are described as a function of the mass ratio to be

$$\alpha^* = \begin{cases} 0.249(M_2/M_1)^{0.56} + 0.0035(M_2/M_1)^{1.5}, & M_1 \leq M_2 \\ 0.0875(M_2/M_1)^{-0.15} + 0.165(M_2/M_1), & M_1 \geq M_2 \end{cases} \tag{A.11}$$

and the sputtering threshold is equal to

$$\frac{E_{th}}{U_s} = \begin{cases} \frac{6.7}{\gamma}, & M_1 \geq M_2, \\ \frac{1+5.7(M_1/M_2)}{\gamma}, & M_1 \leq M_2, \end{cases} \tag{A.12}$$

where γ is the energy transfer factor from elastic collision theory as given by

$$\gamma = \frac{4M_1M_2}{(M_1 + M_2)^2}. \tag{A.13}$$

By obtaining the tabulated W, Q, and s from Ref. [20], the sputtering yield can be calculated as a function of ion energy. This equation has been shown to be accurate for data from many ion-target combinations over various ion energy ranges.

Another empirical equation has been derived by Bohdansky[117] that is valid for low energy sputtering of both heavy and light ions. By making physical arguments about the deposited energy and energy distribution of recoiling atoms, the author modifies Sigmund's fundamental relationship to give

$$Y(E) = \frac{0.042}{U_s}\alpha\left(\frac{M_2}{M_1}\right)S_n(E)\left(\frac{R_p}{R}\right)\left[1-\left(\frac{E_{th}}{E}\right)^{2/3}\right]\left[1-\left(\frac{E_{th}}{E}\right)\right]^2, \tag{A.14}$$

where

$$\frac{R_p}{R} = \frac{1}{0.4(M_2/M_1)+1} \tag{A.15}$$

and

$$\alpha = 0.3\left(\frac{M_2}{M_1}\right)^{2/3}. \tag{A.16}$$

The threshold energy is calculated as

$$\frac{E_{th}}{U_s} = \begin{cases} \frac{1}{\gamma(1-\gamma)} & M_1/M_2 \leq 0.3 \\ 8(M_1/M_2)^{2/5} & M_1/M_2 \geq 0.3. \end{cases} \tag{A.17}$$

This relation has been shown to agree with sputtering yield data for over one hundred ion-target combinations[117], but does not include inelastic effects like the approach by Yamamura et al.[20]. Both semi-empirical formulas are often used in sputtering yield measurement comparisons.

Appendix B

Plasma Redeposition Analysis

Sputtered atoms emitted from the target can be ionized within the background plasma and redirected back to the target by presheath electric fields in a process known as plasma redeposition. Since the sputtering yield measurements record net mass losses, plasma redeposition results in an underestimate of the sputtering yield since less mass is effectively removed. Doerner et al.[77] presented a geometric analysis of plasma redeposition that incorporated measurements of the sputtered molybdenum energy and ionization mean free path. Matlock et al.[84] extended the analysis to include the effects of the angular and energy distributions of sputtered atoms. Here, we follow the methodology of Matlock et al. to obtain estimates of the plasma redeposition rate in the Pi facility plasma.

Figure B.1 shows a schematic of the potential distribution in the plasma. On the downstream side, the sputtered atoms are ejected from the target in a potential trough due to the electrical bias. Due to the presheath, the electric field is directed towards the target

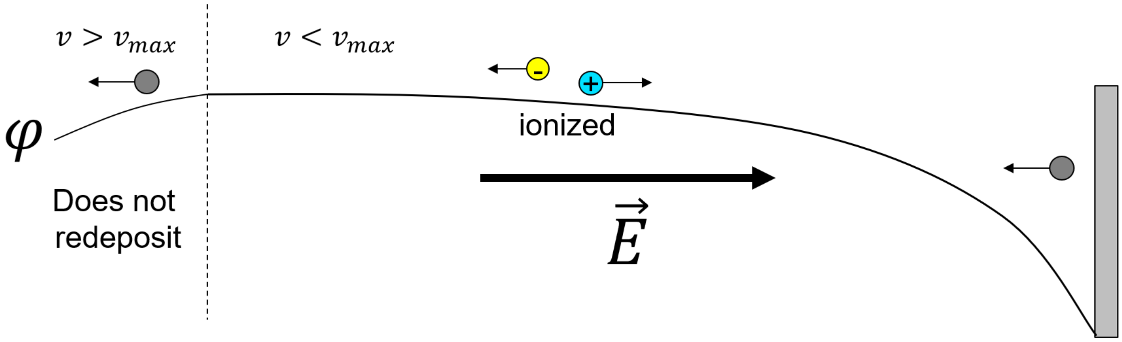

Figure B.1: Illustration of the potential structure between the upstream cathode and downstream biased target.

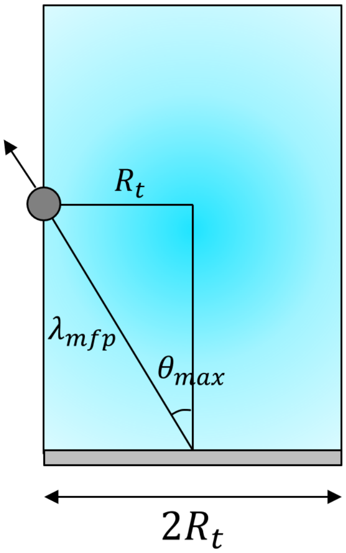

Figure B.2: Geometry definition for maximum sputtering angle in one mean free path.

up until a boundary point where the potential decreases towards the hollow cathode surface upstream. The variables v and v_{max} represent the velocity of the sputtered atom and the maximum velocity required to overcome the near-target potential hill respectively.

Since the trajectory of the sputtered atom is highly dependent on the ejection angle, a spherical coordinate system is used as shown in Figure B.2. Following Matlock et al., I assume all sputtered atoms are ionized in plasma within one ionization mean free path, λ_{mfp}. If a sputtered atom escapes the plasma column, it will not be redeposited. The maximum velocity angle for escaping the plasma column is:

$$\sin\,\theta_{max}(r, v, \psi) = \frac{-r\ \cos(\psi) + \sqrt{r^2\cos^2(\psi) - (r^2 - R_t^2)}}{\lambda_{mfp}(r, v)}, \tag{B.1}$$

where λ_{mfp} is the ionization mean free path, ψ is the azimuthal angle, r is a radial location with the origin at the center of the target, and R_t is the target radius. The ionization mean free path can be calculated as:

$$\lambda_{mfp} = \frac{v}{n_e R_+(v)}, \tag{B.2}$$

where n_e is the local plasma density and $R_+(v)$ is the ionization rate. The ionization rate, $R_+(v)$, can be calculated by integrating the total ionization cross sections of ground state and metastable molybdenum from Kwon et al.[118] over all possible speeds:

$$R_+(v) = \left(\frac{m_e}{2\pi T_e}\right)^{3/2} \int \exp\left(-\frac{m_e c^2}{2T_e}\right) |c - v| \sigma_+(|c - v|) d^3c, \tag{B.3}$$

where $|c-v|$ is equivalent to the random Maxwellian speed in the frame of the sputterant, σ_+ is the ionization cross section, and T_e is the electron temperature in units of eV. Matlock et al. find that the ionization is well fit by $R_+ = (1.978 \times 10^{-25})v^2 - (2.062 \times 10^{-19})v + (3.044 \times 10^{-14})$ when $T_e = 5$ eV. The fit must be changed for different electron temperatures.

With the ionization mean free path, the maximum sputtering angle, θ_{max} can now be obtained and the redeposition flux fraction can be calculated as:

$$\bar{\Gamma}(r) = \frac{\int_0^{v_{max}} f_0(v) v^3 dv \int_0^{2\pi} \int_0^{\theta_{max}} h(\theta) \cos(\theta) \sin(\theta) d\theta d\psi}{\int_0^{\infty} f_0(v) v^3 dv \int_0^{2\pi} \int_0^{\pi/2} h(\theta) \cos(\theta) \sin(\theta) d\theta d\psi}, \tag{B.4}$$

where the distribution of sputtered atoms, $f(v)$, can been separated into angular and energy-dependent components, $f_0(v)$ and $h(\theta)$ respectively. The maximum velocity for escaping the potential tough, v_{max}, is assumed to be 20 eV which is half the discharge voltage, but the redeposition flux is shown later to be nearly independent of this value.

The energy distribution function at low incident energies is given by Stepanova and

Dew[119] to be:

$$g_s(E,\theta) \propto \frac{E}{(E+E_b)^3}\exp\left[-13\left(\frac{m_i(E\ \cos^a\theta + E_b)}{m_t E_i}\right)^{0.55}\right] \times \left(1 - \frac{E+E_b}{E_{max}+E_b}\right), \tag{B.5}$$

where E_b is the binding energy, m_i is the ion mass, E is the sputtered atom energy, θ is the polar ejection angle, m_t is the target mass, E_i is the ion energy, and E_{max} is the maximum energy for a sputtered atom. For argon ions incident on a molybdenum sample, $E_b = 6.82$ eV, $E_{th} = 36$ eV, and $E_i = 300$ eV, $E_{max} = (E_i/E_{th})E_b$. To separate this equation into energy and angular components, the angular term, $\cos^a\theta$, is taken to be unity and the angular component, $h(\theta)$, is set equal to Equation 2.21 as derived by Zhang and Zhang[49]. These distributions for $g(E)$ and $h(\theta)$ can be plugged into Equation B.4 to obtain the plasma redeposition flux fraction, $\bar{\Gamma}$.

Figure B.3 shows the redeposition fraction as a function of plasma density for varying v_{max} values. At lower plasma densities, the redeposition fraction is relatively insensitive to the maximum velocity required to overcome the potential hill since the ionization mean free path is large. At higher plasma densities, there is a plateau in the redeposition fraction because all ions are ionized in the plasma column and any ion with energy insufficient to overcome the potential hill and reach the cathode will be redeposited. The maximum redeposition value is determined purely by the v_{max} value. Since the peak plasma density measured by the Langmuir probe in the Pi facility plasma is roughly 7×10^{17} m^{-3}, it can be seen that the redeposition fraction is insensitive to the value of v_{max} and is less than 10% for all cases.

Figure B.4 shows the redeposition fraction with varying plasma density and temperature. There is clearly a larger spread in redeposition fractions with varying electron temperatures. The measured electron temperature in the Pi facility is around 5 to 7 eV so the redeposition fraction at a plasma density of 7×10^{17} m^{-3} is around 10-15%. The Langmuir probe measurements are reasonably accurate for electron temperature but the plasma density may be

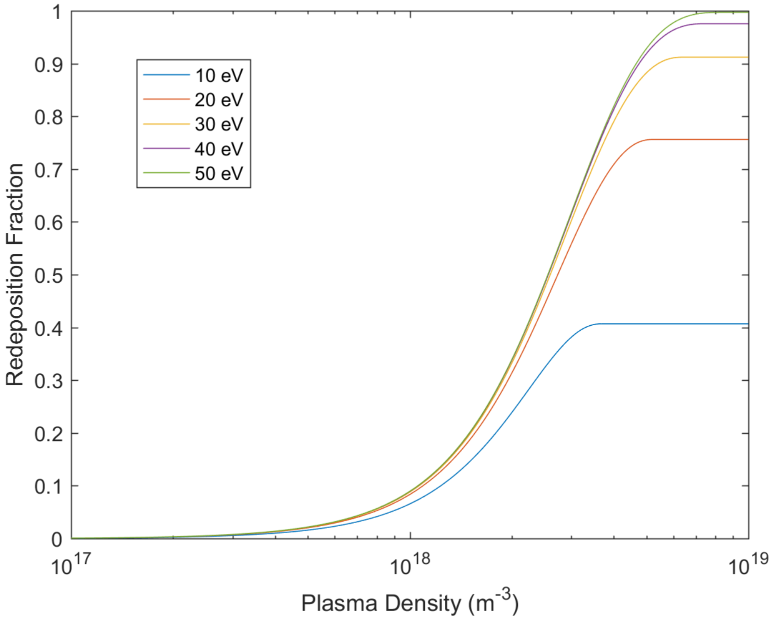

Figure B.3: The redeposition fraction as a function of plasma density at varying v_{max}. The electron temperature is set to 5 eV.

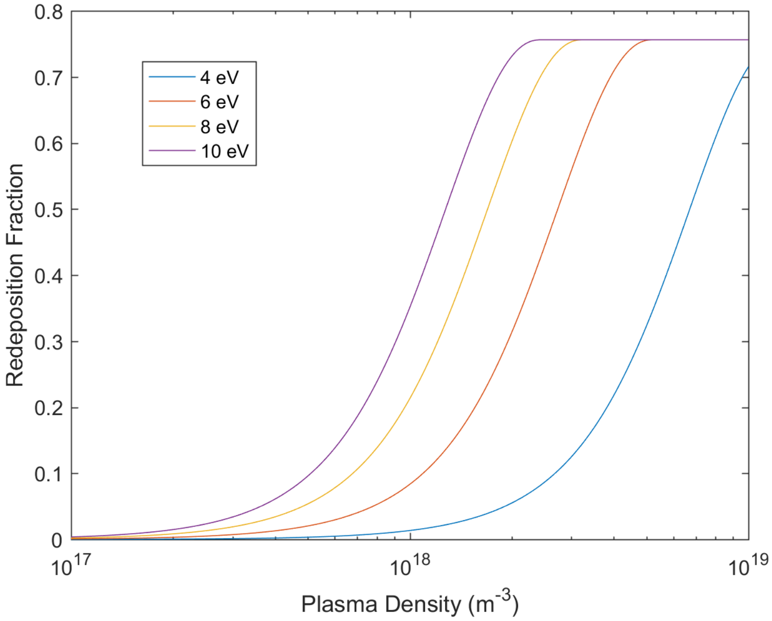

Figure B.4: The redeposition fraction as a function of plasma density at varying electron temperatures. v_{max} is taken to be 20 eV.

off by more than 50% depending on the probe theory used. However, the density is almost certainly below 10^{18} m^{-3} for the current Pi plasma so the range of redeposition fractions should be below 20%. In the instance that the Pi plasma properties change drastically for a given experiment, these calculations can be redone to obtain the estimated plasma redeposition fraction and assess the validity of assuming negligible plasma redeposition effects on the sputtering yield measurements.

Bibliography

[1] Polk, J. E., Kakuda, R. Y., Anderson, J. R., Brophy, J. R., Rawlin, V. K., Patterson, M. J., Sovey, J., and Hamley, J., "An Overview of the Results from an 8200 Hour Wear Test of the NSTAR Ion Thruster," *35th Joint Propulsion Conference*, No. AIAA99-2446, 1999, pp. 1–33.

[2] Tighe, W. G., Chien, K.-R., and Spears, R., "XIPS© Ion Thrusters for Small Satellite Applications," *21st Annual AIAA/USU Conference on Small Satellites*, 2007.

[3] Brophy, J. R., Polk, J. E., Goebel, D. M., Fellow, E., Section, M. E., Engineer, P., Section, M. E., Fellow, E., and Section, M. E., "Development of a 50 ,000s Lithium-fueled Gridded Ion Thruster," *35th International Electric Propulsion Conference*, 2017, pp. 1–7.

[4] Samples, S. A., Li, G. Z., and Wirz, R. E., "Performance testing and development of the MiXI thruster with the ARCH discharge," *2018 Joint Propulsion Conference*, 2018, pp. 1–11.

[5] Li, G. Z., Huerta, C. E., and Wirz, R. E., "Computational modeling of an axial ring cusp hybrid discharge for the MiXI thruster," *2018 Joint Propulsion Conference*, 2018, pp. 1–20.

[6] Wirz, R. and Goebel, D., "Effects of magnetic field topography on ion thruster discharge performance," *Plasma Sources Science and Technology*, Vol. 17, No. 3, 2008, pp. 035010.

[7] Wirz, R. E., Anderson, J. R., Goebel, D. M., and Katz, I., "Decel Grid Effects on Ion Thruster Grid Erosion," *IEEE Transactions on Plasma Science*, Vol. 36, No. 5, oct 2008, pp. 2122–2129.

[8] Wirz, R. E., Katz, I., Goebel, D. M., and Anderson, J. R., "Electron Backstreaming Determination for Ion Thrusters," *Journal of Propulsion and Power*, Vol. 27 of *Joint Propulsion Conferences*, American Institute of Aeronautics and Astronautics, jan 2011, pp. 206–210.

[9] Wirz, R. E., Anderson, J. R., Katz, I., and Goebel, D. M., "Time-Dependent Erosion of Ion Optics," *Journal of Propulsion and Power*, Vol. 27 of *Joint Propulsion Conferences*, American Institute of Aeronautics and Astronautics, jan 2011.

[10] Brown, N. P. and Walker, M. L., "Review of plasma-induced hall thruster erosion," *Applied Sciences (Switzerland)*, Vol. 10, No. 11, 2020.

[11] Goebel, D. M., Jorns, B. A., Hofer, R. R., Mikellides, I. G., and Katz, I., "Pole-piece Interactions with the Plasma in a Magnetically Shielded Hall Thruster," *Propulsion and Energy Forum*, 2014, pp. 1–7.

[12] Mikellides, P. G., "Modeling and Analysis of a Megawatt-Class Magnetoplasmadynamic Thruster," *Journal of Propulsion and Power*, Vol. 20, No. 2, 2004, pp. 204–210.

[13] Schrade, H. O., Auweter-Kurtz, M., and Kurtz, H. L., "Cathode erosion studies on MPD thrusters," *AIAA Journal*, Vol. 25, No. 8, 1987, pp. 1105–1112.

[14] Polk, J. E., Kelly, A. J., Jahn, R. G., Kurtz, H. L., Auweter-Kurtz, M., and Schrade, H. O., "Mechanisms of hot cathode erosion in plasma thrusters," *AlAA/DGLR/JSASS 21st International Electric Propulsion Conference, 1990*, 1990.

[15] Naujoks, D., *Plasma-material interaction in controlled fusion*, Springer Series on atomic, optical, and plasma physics, 2006.

[16] Behrisch, R., Roth, J., Staudenmaier, G., and Verbeek, H., "Sputtering in Fusion Devices," *Nuclear Instruments and Methods in Physics Research Section B: Beam Interactions with Materials and Atoms*, Vol. 18, 1987, pp. 629–638.

[17] Behrisch, R., Federici, G., Kukushkin, A., and Reiter, D., "Material erosion at the vessel walls of future fusion devices," *Journal of Nuclear Materials*, Vol. 313-316, No. SUPPL., 2003, pp. 388–392.

[18] Zhang, Y., Shumlak, U., Nelson, B. A., Golingo, R. P., Weber, T. R., Stepanov, A. D., Claveau, E. L., Forbes, E. G., Draper, Z. T., Mitrani, J. M., McLean, H. S., Tummel, K. K., Higginson, D. P., and Cooper, C. M., "Sustained Neutron Production from a Sheared-Flow Stabilized Z Pinch," *Physical Review Letters*, Vol. 122, No. 13, 2019, pp. 135001.

[19] Li, G., "Time-Resolved Emission Spectroscopy of Field Reversed Configuration Thruster," Tech. rep., Air Force Research Lab, Edwards, CA, 2016.

[20] Yamamura, Y. and Tawara, H., "Energy dependence of ion-induced sputtering yields from monatomic solids at normal incidence," *Atomic Data and Nuclear Data Tables*, Vol. 62, No. 5, 1996, pp. 149–253.

[21] Ziegler, J. F., Ziegler, M. D., and Biersack, J. P., "SRIM - The stopping and range of ions in matter (2010)," *Nuclear Instruments and Methods in Physics Research, Section B: Beam Interactions with Materials and Atoms*, Vol. 268, No. 11-12, 2010, pp. 1818–1823.

[22] Biersack, J. P. and Eckstein, W., "Sputtering studies with the Monte Carlo Program TRIM.SP," *Applied Physics A Solids and Surfaces*, Vol. 34, No. 2, 1984, pp. 73–94.

[23] Wittmaack, K., "Reliability of a popular simulation code for predicting sputtering yields of solids and ranges of low-energy ions," *Journal of Applied Physics*, Vol. 96, No. 5, 2004, pp. 2632–2637.

[24] Rosenberg, D. and Wehner, G. K., "Sputtering Yields for Low Energy He+-, Kr+-, and Xe+-Ion Bombardment," *Journal of Applied Physics*, Vol. 33, No. 5, 1962, pp. 1842–1845.

[25] Huerta, C. E., Matlock, T. S., and Wirz, R. E., "View factor modeling of sputter-deposition on micron-scale-architectured surfaces exposed to plasma," *J. Appl. Phys.*, Vol. 113303, 2016, pp. 1–9.

[26] Littmark, U. and Hofer, W. O., "The influence of surface structures on sputtering: Angular distribution and yield from faceted surfaces," *Journal of Materials Science*, Vol. 13, No. 12, 1978, pp. 2577–2586.

[27] Whitton, J. L., Hofer, W. O., Littmark, U., Braun, M., and Emmoth, B., "Influence of surface morphology on the angular distribution and total yield of copper sputtered by energetic argon ions," *Applied Physics Letters*, Vol. 36, No. 7, 1980, pp. 531–533.

[28] Wehner, G. K. and Hajicek, D. J., "Cone formation on metal targets during sputtering," *Journal of Applied Physics*, Vol. 42, No. 3, 1971, pp. 1145–1149.

[29] Cramer, S. N. and Oblow, E. M., "Feasibility Study of a Honeycomb Vacuum Wall for Fusion Reactors," *Nuclear Fusion*, Vol. 15, No. 2, 1975, pp. 339–343.

[30] Abe, T., Obara, K., Nakamura, H., Sone, K., Ohtsuka, H., Yamada, R., Saidoh, M., and Shimizu, M., "Reduction of effective sputtering yield by honeycomb structures," *Journal of Nuclear Science and Technology*, Vol. 15, No. 7, 1978, pp. 471–475.

[31] Ziegler, J. F., Cuomo, J. J., and Roth, J., "Reduction of ion sputtering yield by special surface microtopography," *Applied Physics Letters*, Vol. 30, No. 6, 1977, pp. 268–271.

[32] Ghoniem, N. M., Sehirlioglu, A., Neff, A. L., Allain, J.-p., and Williams, B., "Applied Surface Science Sputtering of molybdenum and tungsten nano rods and nodules irradiated with 150 eV argon ions," *Applied Surface Science*, Vol. 331, 2015, pp. 299–308.

[33] Matthes, C. S., *Non-uniform Erosion and Surface Evolution of Plasma-Facing Materials for Electric Propulsion*, Ph.D. thesis, Univeristy of California, Los Angeles, 2016.

[34] Goebel, D. M., Hirooka, Y., and Bohdansky, J., "Erosion and redeposition experiments in the PISCES facility," *Journal of Nuclear Materials*, Vol. 147, 1987, pp. 61–70.

[35] Baragiola, R. A., "Principles and mechanisms of ion induced electron emission," *Nuclear Inst. and Methods in Physics Research, B*, Vol. 78, No. 1-4, 1993, pp. 223–238.

[36] Ordonez, C. A. and Peterkin, R. E., "Secondary electron emission at anode, cathode, and floating plasma-facing surfaces," *Journal of Applied Physics*, Vol. 79, No. 5, 1996, pp. 2270–2274.

[37] Hobbs, G. and Wesson, J., "Heat flow through a Langmuir sheath in the presence of electron emission," *Plasma Physics*, Vol. 9, 1967, pp. 85–87.

[38] Hershkowitz, N., "Sheaths: More complicated than you think," *Physics of Plasmas*, Vol. 12, No. 5, 2005, pp. 1–11.

[39] Goebel, D. M. and Katz, I., *Fundamentals of Electric Propulsion: Ion and Hall Thrusters*, John Wiley & Sons, 2008.

[40] Child, C. D., "Discharge from hot CaO wires," *Science*, Vol. 32, No. 5, 1911, pp. 492–511.

[41] Langmuir, I., "The interaction of electron and positive ion space charges in cathode sheaths," *Phys. Rev.*, Vol. 33, No. 6, 1929, pp. 954–989.

[42] Sigmund, P., "Theory of Sputtering. I. Sputtering Yield of Amorphous and Polycrystalline Targets*," *Physical Review*, Vol. 42, No. 3, 1969, pp. 494–511.

[43] Sigmund, P., "Elements of Sputtering Theory," *Nanofabrication by Ion-Beam Sputtering*, 2011, pp. 1–40.

[44] Duchemin, O., Brophy, J., and Garner, C., "A Review of Low Energy Sputtering Theory and Experiments," *NASA Technical Reports Server (NTRS)*, 1997, pp. 1–9.

[45] Matsunami, N., Yamamura, Y., Itikawa, Y., Itoh, N., Kazumata, Y., Miyagawa, S., Morita, K., and Shimizu, R., "Energy Dependence of Sputtering Yields of Monatomic Solids," *IPPJ-AM–14*, 1980.

[46] Wehner, G., "Influence of the angle of incidence on sputtering yields," *Journal of Applied Physics*, Vol. 30, No. 11, 1959, pp. 1762–1765.

[47] Yamamura, Y., "Empirical Formula for Angular Dependence of Sputtering Yields." *Radiation effects*, Vol. 80, No. 1-2, 1984, pp. 57–72.

[48] Yamamura, Y., "Contribution of Anisotropic Velocity Distribution of Recoil Atoms To Sputtering Yields and Angular Distributions of Sputtered Atoms." *Radiation effects*, Vol. 55, No. 1-2, 1981, pp. 49–55.

[49] Zhang, Z. L. and Zhang, L., "Anisotropic angular distribution of sputtered atoms," *Radiation Effects and Defects in Solids*, Vol. 159, No. 5, 2004, pp. 301–307.

[50] Bachmann, L. and Shin, J. J., "Measurement of the sticking coefficients of silver and gold in an ultrahigh vacuum," *Journal of Applied Physics*, Vol. 37, No. 1, 1966, pp. 242–246.

[51] Sigmund, P., "A mechanism of surface micro-roughening by ion bombardment," *Journal of Materials Science*, Vol. 8, No. 11, 1973, pp. 1545–1553.

[52] Bradley, R. M. and Harper, J. M. E., "Theory of ripple topography induced by ion bombardment," *Journal of Vacuum Science & Technology A: Vacuum, Surfaces, and Films*, Vol. 6, No. 4, 1988, pp. 2390–2395.

[53] Bradley, R. M., "Redeposition of sputtered material is a nonlinear effect," *Physical Review B*, Vol. 83, No. 075404, 2011, pp. 1–5.

[54] Matlock, T. S., Goebel, D. M., Conversano, R., and Wirz, R. E., "A dc plasma source

for plasmamaterial interaction experiments," *Plasma Sources Science and Technology*, Vol. 23, No. 2, 2014, pp. 025014.

[55] Sheridan, T. E., "Ion focusing by an expanding , two-dimensional plasma sheath," *Applied physics letters*, Vol. 68, No. 14, 1996, pp. 1918–1920.

[56] Kaufman, H. R., "Technology of ion beam sources used in sputtering," *Journal of Vacuum Science and Technology*, Vol. 15, No. 2, 1978, pp. 272–276.

[57] Ishikawa, J., Sano, F., and Takagi, T., "Ion beam extraction with ion space-charge compensation in beam-plasma type ion source," *Journal of Applied Physics*, Vol. 53, No. 9, 1982, pp. 6018–6028.

[58] Yalin, A. P., Williams, J. D., Surla, V., and Zoerb, K. A., "Differential sputter yield profiles of molybdenum due to bombardment by low energy xenon ions at normal and oblique incidence," *Journal of Physics D: Applied Physics*, Vol. 40, No. 10, 2007, pp. 3194–3202.

[59] Nakles, M. R., *Experimental and Modeling Studies of Low-Energy Ion Sputtering for Ion Thrusters*, Ph.D. thesis, Virginia Polytechnic Institute, 2004.

[60] Laegreid, N. and Wehner, G. K., "Sputtering yields of metals for ar+ and ne+ ions with energies from 50 to 600 ev," *Journal of Applied Physics*, Vol. 32, No. 3, 1961, pp. 365–369.

[61] Mckeown, D., "New Method for Measuring Sputtering in the Region Near Threshold," *Review of Scientific Instruments*, Vol. 133, 1961.

[62] Duchemin, O. B., Polk, J. E., and Drive, B., "Low Energy Sputtering Experiments -For Ion Engine Lifetime Assessment : Preliminary Results," *35th AIAA/ASME/SAE/ASEE Joint Propulsion Conference & Exhibit*, 1999, pp. AIAA–99–2858.

[63] Kolasinski, R. D., Polk, J. E., Goebel, D., and Johnson, L. K., "Sputtering yield measurements at glancing incidence using a quartz crystal microbalance," *Journal of Vacuum Science & Technology A: Vacuum, Surfaces, and Films*, Vol. 25, No. 2, 2007, pp. 236.

[64] Sauerbrey, G., "Verwendung von Schwingquarzen zur Wagungdiinner Schichten und zur Mikrowagung," *Zeitschrift fur Physik*, Vol. 155, 1959, pp. 206–222.

[65] Rahtu, A. and Ritala, M., "Compensation of temperature effects in quartz crystal microbalance measurements," *Applied Physics Letters*, Vol. 80, No. 3, 2002, pp. 521–523.

[66] Blandino, J. J., Goodwin, D. G., and Garner, C. E., "Low energy sputter yields for diamond, carbon-carbon composite, and molybdenum subject to xenon ion bombardment," *Diamond and Related Materials*, Vol. 9, No. 12, 2000, pp. 1992–2001.

[67] Kundu, S., Ghose, D., Basu, D., and Karmohapatro, S. B., "The angular distribution of sputtered silver atoms," *Nuclear Inst. and Methods in Physics Research, B*, Vol. 12, No. 3, 1985, pp. 352–357.

[68] Chiplonkar, V. T. and Rane, S. R., "The Angular Distribution of Sputtered Particles From Polycrystalline Plane Gold Target by Impact with Positive Ions of Argon," *Proceedings of the Indian Academy of Sciences - Section A*, Vol. 61, No. 2, 1965.

[69] Wucher, A. and Reuter, W., "Angular distribution of particles sputtered from metals and alloys," *Journal of Vacuum Science & Technology A: Vacuum, Surfaces, and Films*, Vol. 6, No. 4, 1988, pp. 2316.

[70] Yalin, A., Surla, V., Butweiller, M., and Williams, J., "Detection of sputtered metals with cavity ring-down spectroscopy," *Applied Optics*, Vol. 44, No. 30, 2005, pp. 6496.

[71] Rubin, B., Topper, J. L., and Yalin, a. P., "Total and differential sputter yields of boron nitride measured by quartz crystal microbalance," *Journal of Physics D: Applied Physics*, Vol. 42, No. 20, 2009, pp. 205205.

[72] Bhattacharjee, S., Zhang, J., Shutthanandan, V., Ray, P. K., Shivaparan, N. R., and Smith, R. J., "Application of secondary neutral mass spectrometry in low-energy sputtering yield measurements," *Nuclear Instruments and Methods in Physics Research, Section B: Beam Interactions with Materials and Atoms*, Vol. 129, No. 1, 1997, pp. 123–129.

[73] Smith, J. N., Meyer, C. H., and Layton, J. K., "Auger electron spectroscopy in sputtering measurements: Application to lowenergy Ar + sputtering of Ag and Nb," *Journal of Applied Physics*, Vol. 46, No. 10, 1975, pp. 4291–4293.

[74] Bay, H., "Laser Induced Fluorescence as a technique for investigations of sputtering phenomena," *Nuclear Instruments and Methods in Physics Research Section B: Beam Interactions with Materials and Atoms*, 1987, pp. 430–445.

[75] Stevens, R. E., "Methodology and Feasibility of In Situ Erosion Measurements in Carbon-Based Ion Thruster Grids by Laser-Induced Fluorescence," *27th International Electric Propulsion Conference*, 2001, pp. 1–7.

[76] Gaeta, C. J., Matossian, J. N., Turley, R. S., Williams, J. R. B. J. D., and Williamsonh, W. S., "Erosion Rate Diagnostics in Ion Thrusters Using Laser-Induced Fluorescence," *Journal of Propulsion and Power*, Vol. 9, No. 3, 1993.

[77] Doerner, R. P., Whyte, D. G., and Goebel, D. M., "Sputtering yield measurements during low energy xenon plasma bombardment," *Journal of Applied Physics*, Vol. 93, No. 9, 2003, pp. 5816–5823.

[78] B, R., M, P., and M, M., "Rapid evaluation of ion thruster lifetime using optical

emission spectroscopy," *18th International Electric Propulsion Conference*, 1985, pp. 1–48.

[79] Vasina, P., Fekete, M., Hnilica, J., Klein, P., Dosoudilova, L., Dvorak, P., and Navratil, Z., "Determination of titanium atom and ion densities in sputter deposition plasmas by optical emission spectroscopy," *Plasma Sour. Sci. Technol.*, Vol. 24, 2015.

[80] Orsitto, F., Borra, M., Coppotelli, F., Gatti, G., Neri, E., Orsitto, F., Borra, M., Coppotelli, F., Gatti, G., and Neri, E., "MoI density measurements by laser induced fluorescence spectroscopy," *Review of Scientific Instruments*, Vol. 921, 1999, pp. 1–5.

[81] Stuart, R. V. and Wehner, G. K., "Sputtering thresholds and displacement energies," *Physical Review Letters*, Vol. 4, No. 8, 1960, pp. 409–410.

[82] Chu, E., Goebel, D. M., and Wirz, R. E., "Reduction of Energetic Ion Production in Hollow Cathodes by External Gas Injection," *Journal of Propulsion and Power*, Vol. 29, No. 5, 2013, pp. 1155–1163.

[83] Goebel, D. M., Jameson, K. K., Katz, I., and Mikellides, I. G., "Potential fluctuations and energetic ion production in hollow cathode discharges," *Physics of Plasmas*, Vol. 14, No. 10, 2007, pp. 103508.

[84] Matlock, T. S., Goebel, D. M., Conversano, R., and Wirz, R. E., "A dc plasma source for plasmamaterial interaction experiments," *Plasma Sources Science and Technology*, Vol. 23, No. 2, 2014, pp. 025014.

[85] Matlock, T. S., Conversano, R. W., Goebel, D. M., and Wirz, R. E., "The Plasma-Material Interactions Facility at UCLA," *49th AIAA/ASME/SAE/ASEE Joint PropulsionConference*, jul 2013, pp. 1–10.

[86] Steinbruchel, C., "A new method for analyzing Langmuir probe data and the determination of ion densities and etch yields in an etching plasma," *Journal of Vacuum Science & Technology A: Vacuum, Surfaces, and Films*, Vol. 8, No. 3, 1990, pp. 1663.

[87] Matlock, T. S., Dodson, C. A., Goebel, D. M., and Wirz, R. E., "Measurements of Transport due to Low Frequency," *34th International Electric Propulsion Conference*, 2015, pp. 1–10.

[88] Ferron, J., Alonso, E. V., Baragiola, R. A., and Oliva-Florio, A., "Electron emission from molybdenum under ion bombardment," *Journal of Physics D: Applied Physics*, Vol. 14, No. 9, 1981, pp. 1707–1720.

[89] Mahadevan, P., Layton, J., and Medved, D., "Secondary Electron Emission from Clean Surface of Molybdenum Due to Low-Energy Noble Gas Ions," *Physical Review*, Vol. 129, No. 1, 1963.

[90] Martínez-Sánchez, M. and Ahedo, E., "Magnetic mirror effects on a collisionless plasma in a convergent geometry," *Physics of Plasmas*, Vol. 18, No. 3, 2011, pp. 1–10.

[91] Matthes, C. S., Ghoniem, N. M., Li, G. Z., Matlock, T. S., Goebel, D. M., Dodson, C. A., and Wirz, R. E., "Fluence-dependent sputtering yield of micro-architectured materials," *Applied Surface Science*, Vol. 407, 2017, pp. 223–235.

[92] Li, G., Dodson, C. A., Wirz, R. E., Matlock, T. S., and Goebel, D. M., "Implementation of in situ diagnostics for sputter yield measurements in a focused plasma," *52nd AIAA/SAE/ASEE Joint Propulsion Conference*, 2016, pp. 1–13.

[93] Weijsenfeld, C. H., Hoogendoorn, A., and Koedam, M., "Sputtering of polycrystalline metals by inert gas ions of low energy (100-1000eV)," *Physica*, Vol. 27, 1961, pp. 763–764.

[94] Zoerb, K. A., Williams, J. D., Williams, D. D., and Yalin, A. P., "Differential Sputtering Yields of Refractory Metals by Xenon, Krypton, and Argon Ion Bombardment at Normal and Oblique Incidences," *IEPC*, 2005, pp. 1–25.

[95] Küstner, M., Eckstein, W., Dose, V., and Roth, J., "The influence of surface roughness on the angular dependence of the sputter yield," *Nuclear Instruments and Methods in*

Physics Research Section B: Beam Interactions with Materials and Atoms, Vol. 145, No. 3, 1998, pp. 320–331.

[96] Hapke, B. and Cassidy, W., "Is the moon really as smooth as a billiard ball? Remarks concerning recent models of sputter-fractionation on the lunar surface," *Geophysical Research Letters*, Vol. 5, No. 4, 1978, pp. 5–8.

[97] Anders, C., Bringa, E. M., and Urbassek, H. M., "Sputtering of a metal nanofoam by Au ions," *Nuclear Instruments and Methods in Physics Research, Section B: Beam Interactions with Materials and Atoms*, Vol. 342, 2015, pp. 234–239.

[98] Rodriguez-Nieva, J. F., Bringa, E. M., Cassidy, T. A., Johnson, R. E., Caro, A., Fama, M., Loeffler, M. J., Baragiola, R. A., and Farkas, D., "Sputtering from a porous material by penetrating ions," *Astrophysical Journal Letters*, Vol. 743, No. 1, 2011.

[99] Rodriguez-Nieva, J. F. and Bringa, E. M., "Molecular dynamics simulations of the sputtering of a nanoporous solid," *Nuclear Inst. and Methods in Physics Research, B*, Vol. 304, 2013, pp. 25–28.

[100] Cassidy, T. A. and Johnson, R. E., "Monte Carlo model of sputtering and other ejection processes within a regolith," *Icarus*, Vol. 176, No. 2, 2005, pp. 499–507.

[101] Johnson, R. E., "Application of Laboratory Data to the Sputtering," *Icarus*, Vol. 78, No. 1, 1989, pp. 206–210.

[102] Gao, E., Nadvornick, W., Doerner, R., and Ghoniem, N. M., "The influence of low-energy helium plasma on bubble formation in micro-engineered tungsten," *Journal of Nuclear Materials*, Vol. 501, 2018, pp. 319–328.

[103] Gao, E., Doerner, R., Williams, B., and Ghoniem, N. M., "Low-energy helium plasma effects on textured micro-porous tungsten," *Journal of Nuclear Materials*, Vol. 517, 2019, pp. 86–96.

[104] Kim, C. K. and Economou, D. J., "Plasma molding over surface topography: Energy and angular distribution of ions extracted out of large holes," *Journal of Applied Physics*, Vol. 91, No. 5, 2002, pp. 2594–2603.

[105] Kim, D. and Economou, D. J., "Simulation of plasma molding over a ring on a flat surface," *Journal of Applied Physics*, Vol. 94, No. 6, 2003, pp. 3740–3747.

[106] Watterson, P. A., "Child-langmuir sheath structure around wedge-shaped cathodes," *Journal of Physics D: Applied Physics*, Vol. 22, No. 9, 1989, pp. 1300–1307.

[107] Banhart, J., "Manufacture, characterisation and application of cellular metals and metal foams," *Progress in Materials Science*, Vol. 46, No. 6, 2001, pp. 559–632.

[108] Yamamoto, H. and Saiga, N., "Temperature-Corrected Quartz Crystal Microbalance for Real-Time Film Thicness Monitoring in Vaccum Evaporation.pdf," *Jpn. J. Appl. Phys.*, Vol. 35, No. 9, 1996, pp. 4833–4838.

[109] Huerta, C. E., Patino, M. I., and Wirz, R. E., "Secondary electron emission from textured surfaces," *Journal of Physics D: Applied Physics*, Vol. 51, No. 14, 2018.

[110] Matsunami, N., Yamamura, Y., Itikawa, Y., Itoh, N., Kazumata, Y., Miyagawa, S., Morita, K., Shimizu, R., and Tawara, H., "Energy dependence of the ion-induced sputtering yields of monatomic solids," *Atomic Data and Nuclear Data Tables*, Vol. 31, No. 1, 1984, pp. 1–80.

[111] Meyer, M. E., Byrne, M. P., Jorns, B. A., and Boyd, I. D., "Erosion of a meshed reflector in the plume of a hall effect thruster, Part 1: Modeling," *AIAA Propulsion and Energy Forum and Exposition, 2019*, No. August, 2019, pp. 1–22.

[112] Byrne, M. P., Meyer, M. E., Boyd, I. D., and Jorns, B. A., "Erosion of meshed reflector in the plume of a hall effect thruster, Part 2: Experiments," *AIAA Propulsion and Energy Forum and Exposition, 2019*, No. August, 2019, pp. 1–15.

[113] Ray, P. K. and Shutthanandan, V., "Low-Energy Sputtering," *NASA/CR-1999-209161*, 1999, pp. 1–46.

[114] Lindhard, J., Scharff, M., and Schiott, H., "Range concepts and heavy ion ranges," *Matematisk-fysiske Meddelelse r*, Vol. 33, No. 14, 1963, pp. 42.

[115] Yamamura, Y., Matsunami, N., and Itoh, N., "A new empirical formula for the sputtering yield," *Radiation Effects*, Vol. 68, No. 3, 1982, pp. 83–87.

[116] Yamamura, Y., Matsunami, N., and Itoh, N., "Theoretical Studies on an Empirical Formula for Sputtering Yield At Normal Incidence." *Radiation effects*, Vol. 71, No. 1-2, 1983, pp. 65–86.

[117] Bohdansky, J., "A universal relation for the sputtering yield of monatomic solids at normal ion incidence," *Nuclear Inst. and Methods in Physics Research, B*, Vol. 2, No. 1-3, 1984, pp. 587–591.

[118] Kwon, D. H., Rhee, Y. J., and Kim, Y. K., "Cross sections for ionization of Mo and Mo+ by electron impact," *International Journal of Mass Spectrometry*, Vol. 245, No. 1-3, 2005, pp. 26–35.

[119] Stepanova, M. and Dew, S. K., "Estimates of differential sputtering yields for deposition applications," *Journal of Vacuum Science & Technology A: Vacuum, Surfaces, and Films*, Vol. 19, No. 6, 2001, pp. 2805.